
Spatially-resolved star formation histories and molecular gas depletion time of nearby galaxies

Mei-Ling Huang



München 2015

Spatially-resolved star formation histories and molecular gas depletion time of nearby galaxies

Mei-Ling Huang

Dissertation
an der Fakultät der Physik
der Ludwig-Maximilians-Universität
München

vorgelegt von
Mei-Ling Huang
aus Taiwan

München, den 20. Februar 2015

Erstgutachter: Simon White

Zweitgutachter: Andreas Burkert

Tag der mündlichen Prüfung: April 29. 2015

Contents

| | |
|--|-------------|
| Summary | xi |
| Zusammenfassung | xiii |
| 1 Introduction | 1 |
| 1.1 Galaxies in the local universe | 2 |
| 1.2 What spectra tell us | 4 |
| 1.2.1 Metallicities of galaxies | 4 |
| 1.2.2 The stellar populations of galaxies | 8 |
| 1.3 Gas and star formation in galaxies | 12 |
| 1.3.1 ISM in general | 13 |
| 1.3.2 H ₂ observations | 16 |
| 1.3.3 H ₂ gas and star formation | 19 |
| 1.4 This thesis | 26 |
| 2 Spatially-resolved star formation histories of nearby galaxies | 29 |
| 2.1 Introduction | 29 |
| 2.2 Data | 31 |
| 2.3 Analyses | 35 |
| 2.3.1 A PCA-based Balmer absorption line index | 35 |
| 2.3.2 Comparison with a library of SEDs of model galaxies | 35 |
| 2.3.3 Fitting procedure | 36 |
| 2.3.4 Separating inner and outer regions of galaxies | 37 |
| 2.3.5 categorization of galaxies based on their star formation histories . . | 37 |
| 2.4 Results | 39 |
| 2.4.1 Dependence of star formation history | 39 |
| 2.4.2 Relations between star formation history, gas and metallicity . . . | 48 |
| 2.5 Summary and discussion | 50 |

| | |
|---|------------|
| 3 Variation in molecular gas depletion time: main parameter dependency | 53 |
| 3.1 Introduction | 53 |
| 3.2 Data | 55 |
| 3.2.1 COLD GASS | 55 |
| 3.2.2 HERACLES | 57 |
| 3.3 Analyses | 58 |
| 3.3.1 Molecular gas depletion time in the COLD GASS sample | 58 |
| 3.3.2 Properties in the HERACLES sample | 61 |
| 3.4 Results | 62 |
| 3.4.1 Depletion time based on our new SFR estimates | 63 |
| 3.4.2 Systematic effects caused by dust attenuation | 65 |
| 3.4.3 Primary or induced correlation? | 69 |
| 3.4.4 Comparison with results for 1 kpc grids | 72 |
| 3.5 Summary and discussion | 76 |
| 4 Impact of galaxy structures on molecular gas depletion time | 79 |
| 4.1 Introduction | 79 |
| 4.2 Data | 81 |
| 4.2.1 HERACLES | 81 |
| 4.2.2 ATLAS ^{3D} | 82 |
| 4.2.3 COLD GASS | 82 |
| 4.3 Methods | 87 |
| 4.3.1 Overview of the spatial scales probed by the observations | 87 |
| 4.3.2 Identification of bulges/arms/bars/rings | 88 |
| 4.3.3 Derivation of M_{H_2} or Σ_{H_2} | 88 |
| 4.3.4 Derivation of SFRs or Σ_{SFR} | 89 |
| 4.3.5 Derivation of stellar mass | 93 |
| 4.4 Results | 93 |
| 4.4.1 The effect of internal structures on molecular gas depletion time . . | 93 |
| 4.4.2 Linking the results together | 95 |
| 4.5 Summary and discussion | 102 |
| 5 Conclusion and outlook | 105 |
| Bibliography | 109 |
| Acknowledgements | 116 |

List of Figures

| | | |
|------|--|----|
| 1.1 | Spectral evolution of a simple stellar population | 10 |
| 1.2 | Summary of the stellar population synthesis technique | 11 |
| 1.3 | The star formation law for nearby galaxies on global scale | 21 |
| 1.4 | The star formation law for nearby galaxies on sub-kpc scale | 23 |
| 2.1 | Examples of type A and type B galaxies | 33 |
| 2.2 | Examples of type C and type D galaxies | 34 |
| 2.3 | The average errors as a function of radius | 38 |
| 2.4 | Galaxy types and recently-formed stellar mass in $\mu_* - M_*$ plane | 40 |
| 2.5 | Galaxy types and recently-formed stellar mass in $R_{90}/R_{50} - M_*$ plane | 41 |
| 2.6 | Galaxy types and recently-formed stellar mass in color- M_* plane | 42 |
| 2.7 | Distribution of the fraction of starbursts | 46 |
| 2.8 | Distribution of the look-back time | 47 |
| 2.9 | Correlation between recently-formed stellar mass, metallicity, gas | 49 |
| 3.1 | Ratio of IRAM beamsize to R_{25} for COLD GASS sample | 57 |
| 3.2 | Comparison of WISE 22 μm and Spitzer 24 μm fluxes | 59 |
| 3.3 | Comparison of SFR estimates | 61 |
| 3.4 | Molecular gas depletion time as a function of galaxy properties | 64 |
| 3.5 | Results of fitted linear relations | 66 |
| 3.6 | Stellar surface density and concentration as functions of $A\nu$ and IR/UV | 67 |
| 3.7 | Comparison of the depletion time | 68 |
| 3.8 | Molecular gas depletion time as a function of M_* and SFR/M_* | 70 |
| 3.9 | Molecular gas depletion time as a function of μ_* and SFR/M_* | 71 |
| 3.10 | Molecular gas depletion times within 1kpc ² grid cells | 73 |
| 3.11 | Comparison of the $t_{\text{dep}} - \text{sSFR}$ relation for COLD GASS and HERACLES | 75 |
| 3.12 | Depletion time and molecular gas surface density | 77 |
| 4.1 | Comparison of HERACLES and ATLAS ^{3D} galaxies | 83 |

| | | |
|------|---|-----|
| 4.2 | Multi-wavelength images for NGC3607 in the ATLAS ^{3D} sample | 84 |
| 4.3 | One-dimensional decomposition profile for HERACLES sample | 85 |
| 4.4 | SDSS g-band residual maps for HERACLES galaxies | 86 |
| 4.5 | Relation between K-band and WISE 22 μ m luminosity | 89 |
| 4.6 | Depletion time and the IR/UV ratio | 90 |
| 4.7 | $t_{\text{dep}} - \text{sSFR}$ relation for the HERACLES and ATLAS ^{3D} sample | 92 |
| 4.8 | Distribution in the $t_{\text{dep}} - \text{ssSFR}$ plane for galaxies with structures | 94 |
| 4.9 | Distribution of the ratio of $\text{SFR}_{22\mu\text{m}}$ to SFR_{FUV} | 96 |
| 4.10 | Distribution of the molecular gas surface densities | 97 |
| 4.11 | Distribution of the stellar surface densities | 99 |
| 4.12 | Residuals from the $t_{\text{dep}} - \text{ssSFR}$ relation | 101 |
| 4.13 | Constraint on t_{dep} with sSFR and Σ_* | 103 |

List of Tables

| | | |
|-----|---|----|
| 3.1 | Summary of the best-fit linear relations between t_{dep} and galaxy parameters | 63 |
| 3.2 | Summary of the best-fit linear relations for HERACLES sample | 73 |

Summary

This thesis has focused on observational studies of galaxy evolution. We combine multi-wavelength data to derive various physical properties of nearby galaxies. In particular, we study the recent star formation histories (SFHs) of galaxies from their optical spectra, and the relations between molecular gas and star formation of galaxies from their radio, ultraviolet, and infrared observations.

First, we constrain the radial dependence of the recent SFHs of ~ 200 local galaxies with the long-slit spectroscopy data by fitting stellar population models to the combination of specific star formation rate (sSFR), 4000 Å break strength and Balmer absorption lines. The late-type and early-type galaxies show distinct behaviors in their recent star formation histories. In late-type systems, bursts occur both in the inner and in the outer regions of the galaxy. The fraction of stars formed in a single burst episode is typically around 15% of the total stellar mass in the inner regions of the galaxy and around 5% of the mass in the outer regions. On the other hand, bursts occur predominantly in the outer disk in massive and bulge-dominated galaxies, and the fraction of stars formed in a single episode is only 2 - 3% of the underlying stellar mass.

One of the most fundamental questions in modern astrophysics is how galaxies convert their gas into stars, and how this process may change with the galaxy internal properties and/or across cosmic time. We study the variations in molecular gas depletion time (t_{dep}), defined as the molecular gas mass divided by the star formation rate (SFR), and which tells us how fast the gas will be consumed under the current SFR. We establish that the main parameter dependence of t_{dep} is upon sSFR on both local and global scales. The strong correlation between t_{dep} and sSFR extends continuously over a factor of 10 in t_{dep} and from $\log \text{sSFR} = -11.5$ to -9 , i.e. , from nearly quiescent patches of the disc to disc regions with very strong star formation. This leads to the conclusion that the local molecular gas depletion time in galactic disks is dependent on the local fraction of young-to-old stars and that galaxies with high current-to-past-averaged star formation activity, will drain their molecular gas reservoir sooner.

We further study the impact of galaxy internal structures such as the bulge, arm, bar

and ring on the variation of t_{dep} on kiloparsec and global scales. The displacements in the main t_{dep} -sSFR plane for different structures is linked to the variations in stellar, rather than gas surface densities: regions with high stellar surface densities such as the central bulges of galaxies have a reduced t_{dep} at a given sSFR, while regions with low stellar surface densities such as the disk of galaxies have a longer t_{dep} at a given sSFR. Our best current predictor for t_{dep} , both globally and for 1kpc grids, is given by $\log t_{\text{dep}} = -0.36 \log \Sigma_{\text{SFR}} + 0.22 \log \Sigma_* + 5.87$, where Σ_{SFR} and Σ_* are SFR and stellar surface densities.

Zusammenfassung

Diese Arbeit beschäftigt sich mit Beobachtungsstudien der Entwicklung von Galaxien. Wir kombinieren Beobachtungsdaten aus unterschiedlichen Wellenlängen, um verschiedene physikalische Eigenschaften von nahen Galaxien abzuleiten. Insbesondere studieren wir die jüngste Sternentstehungsgeschichte (SFHs) von Galaxien an Hand ihrer optischen Spektren, sowie die Beziehungen zwischen dem molekularen Gas und der Sternentstehung von Galaxien an Hand ihrer Radio-, Ultravioletts- und Infrarot-Beobachtung.

Zuerst schränken wir die radiale Abhängigkeit der jüngsten SFHs von ~ 200 lokalen Galaxien mit Lang-Spalt-Spektroskopie Daten ein, indem wir Sternpopulationsmodellen an eine Kombination von spezifischer Sternformierungsrate (sSFR), 4000 \AA Bruchfestigkeit und Balmer Absorptionlinien anpassen. Die “späten” und “frühen” Galaxien zeigen ein deutliches Verhalten bezüglich ihrer jüngsten Sternentstehungsgeschichte. In späten Systemen treten Ausbrüche sowohl in den inneren wie auch den äußeren Regionen einer Galaxie auf. Der Anteil von Sternen, die in einer einzigen Ausbruchsepisode gebildet werden, beträgt typischerweise etwa 15% der gesamten Sternenmasse der inneren Regionen von Galaxien und etwa 5% der Masse der äußeren Regionen. Andererseits treten Ausbrüche vorwiegend in der äußeren Scheibe in massiven von Ausbuchtungen dominierten Galaxien auf und der Anteil von Sternen, die in einer einzelnen Episode gebildet werden, beträgt nur 2–3% der zugrundeliegenden Sternenmasse.

Eine der grundlegendsten Fragen der modernen Astrophysik ist die Frage wie Galaxien ihr Gas in Sterne umwandeln und auf welche Weise dieser Prozess sich in Bezug auf die intrinsischen Eigenschaften der Galaxie sowie über die kosmische Zeitentwicklung verhält. Wir untersuchen die Veränderungen der molekularen “Gasentleerungszeit” (t_{dep}), die als das Verhältnis von molekularer Gasmasse und Sternentstehungsrate (SFR) definiert ist und die beschreibt, wie schnell das Gas bei der jetzigen SFR verbraucht wird. Wir begründen, dass t_{dep} hauptsächlich parametrisch von der sSFR auf lokalen als auch globalen Skalen abhängt. Die starke Korrelation von t_{dep} und sSFR besteht kontinuierlich über einen Faktor von 10 von t_{dep} und über $\log \text{sSFR} = -11.5$ to -9 , d.h. bei nahezu bewegungslosen Stellen von Scheiben zu Scheiben Regionen mit sehr starker Sternentstehung. Dies führt zu der

Feststellung, dass die lokale “Gasentleerungszeit” in galaktischen Scheiben abhängig ist vom lokalen Anteil von jungen-zu-alten Sternen und dass Galaxien mit hohen jetzigen-zu-vergangenen-gemittelten Sternbildungsaktivitäten ihr molekulares Gasreservoir schneller aufbrauchen werden.

Wir untersuchen weiterhin den Einfluss von intrinsischen Eigenschaften von Galaxien wie etwa Ausbuchtungen, Arme, Stäbe, sowie Ringe auf die Veränderung von t_{dep} auf Kiloparsec und globalen Größenordnungen. Die Verschiebung in der hauptsächlichen $t_{\text{dep}} - \text{sSFR}$ Ebene für verschiedene Strukturen hängt von den Veränderungen der stellaren Strukturen eher ab als von den Gasoberflächendichten: Regionen mit hoher stellaren Oberflächendichten, wie etwa die zentralen Ausbuchtungen von Galaxien, haben eine reduzierte t_{dep} bei einer gegebenen sSFR, während Regionen mit einer niedrigeren stellaren Oberflächendichte, wie die Scheibe von Galaxien, eine längere t_{dep} bei gegebener sSFR haben. Unser bester momentaner Vorhersagewert für t_{dep} , sowohl global als auch für 1kpc Gittern, ergibt sich aus $\log t_{\text{dep}} = -0.36 \log \Sigma_{\text{SFR}} + 0.22 \log \Sigma_* + 5.87$, wobei Σ_{SFR} und Σ_* die SFR sowie die stellare Oberflächendichte ist.

Chapter 1

Introduction

This thesis has focused on observational studies of galaxy formation and evolution. Galaxies emit radiation across the full extent of electromagnetic spectrum. Using multi-wavelength data allows astronomers to measure various fundamental properties of galaxies, such as their stellar masses, star formation rates, gas and dust contents, and even stellar ages. For example, we obtain the amount of atomic hydrogen gas in galaxies directly by 21-cm emission observations. The molecular hydrogen gas mass can be estimated by observing the emission from carbon monoxide (CO) at millimeter wavelengths. The combination of far-ultraviolet (UV) and infrared (IR) light yields robust measurements of star formation rates. With optical spectra, we obtain insights into the chemical compositions and star formation histories of galaxies. In this work, we have combined multi-wavelength data from the ultraviolet, optical, infrared to the radio, and we have derived various physical properties of nearby galaxies.

In the framework of the dark matter halo merging history (White & Frenk 1991), galaxy evolution can be simplistically characterized by a three-phase process: (1) accretion of gas from the intergalactic medium, (2) conversion from gas into stars, and (3) return of enriched gas and energy to the intergalactic medium. All of them have gas involved. We are particularly interested in the galaxy evolution during the first and second phase in this work. More specifically, we study the star formation histories of nearby galaxies to quantify how the recent star formation fueled by the newly-accreted gas differs among different types of galaxies. We also study the relation between molecular gas and star formation of galaxies, and constrain how this relation correlates with other galaxy physical parameters.

In this first chapter, we give a brief overview of local galaxies, and the possible mechanisms that explain how galaxies quench and sustain their star formation activity in Section 1.1. To gain insight into how the gas accretion refuel galaxies, we analyze the stellar pop-

ulations using long-slit spectroscopic data, and estimate the newly-formed stars related to gas accretion. We therefore introduce the important information provided by galaxy spectra and how to interpret them via stellar population synthesis techniques in Section 1.2. In Section 1.3, We introduce the properties of the interstellar medium and focus on molecular gas and star formation. We finally give an outline of our main works in Section 1.4.

1.1 Galaxies in the local universe

In the local universe ($z \sim 0.1$), galaxies have a large variety of features, including morphologies, sizes, colors, or luminosities, which are connected to the differences in their physical properties. The two main types of galaxies are spiral and elliptical galaxies. Spiral galaxies consist of a disk with spiral arm structure and a central bulge ,while elliptical galaxies are galaxies that have nearly elliptical isophotes without any clear sub-structure. The S0 galaxies, an intermediate type between ellipticals and spirals, have lenticular shapes and contain a bulge with a large enveloping region that often appears like a disk without spiral arms. According to the Hubble’s classification scheme, ellipticals and S0 galaxies are called early-type galaxies, whereas spirals are termed late-type galaxies. However, this simple classification does not reflect the true evolutionary history of galaxies.

Our understanding of galaxy evolution has made significant progresses in the last decade thanks to the large surveys, such as the Sloan Digital Sky Survey (SDSS; York et al. 2000) in the optical regime, the Galaxy Evolution Explorer (GALEX; Martin et al. 2005) in the UV regime. Galaxies are found to be separated into two populations around a transitional stellar mass of $3 \times 10^{10} M_{\odot}$, below which galaxies tend to be blue, disk-dominated, with high gas fractions and on-going star formation, and above which galaxies are mostly red, bulge-dominated with old stellar populations and low gas content. This transition is clearly seen in the bimodality of various galaxy properties, such as colors, surface mass densities, concentrations, as observed by the SDSS (e.g. Kauffmann et al. 2003; Baldry et al. 2004). Besides, observations of galaxies at higher redshifts show that these distinctions have existed already at redshift as high as 2.5 (Williams et al. 2010; Wuyts et al. 2011). The number of blue galaxies appears to have remained almost constant since redshift $z \sim 1$ whereas that of red galaxies has at least doubled (e.g. Faber et al. 2007; Brown et al. 2007; Ilbert et al. 2010). A natural explanation is that galaxies evolve with time from the blue cloud to the red sequence, i.e., from star-forming to quenched galaxies.

Since the evolution of galaxies hinges on their star formation activity and the star formation depends on the supply of the gas fuel, an important question in modern astro-

physics is how galaxies are starved of their gas, lose their star formation and evolve into red galaxies. Another important question is how galaxies accrete gas to sustain their star formation. There are observational evidences that our own Milky Way has formed stars at a relatively constant rate throughout the Hubble time, implying that the full reservoir of cold gas was not in place since the beginning but has been accreted slowly. The gas depletion time is found to be of the order of ~ 1 Gyr for star-forming galaxies at redshifts $0 < z < 2$ (e.g. Genzel et al. 2010), but they have been forming stars continuously for a Hubble time. This suggests the need for an external gas supply to sustain star formation. We briefly introduce the mechanisms that are related to quenching processes, as well as gas accretion in galaxies below.

How galaxies quench star formation

Many mechanisms have been proposed, and they can be generally classified into two main categories. First, quenching is related to internal processes in which the gas inside the galaxy is expelled or becomes inert to star formation. An example is the negative feedback from accretion of matter onto supermassive black holes. This acts to heat the surrounding gas (radiative feedback) and/or to drive the gas out by winds (mechanical feedback). Another example is related to “morphological quenching” – the bulge in the center of galaxy acts to stabilize the disk against gravitational instabilities and to prevent gas from forming stars (Martig et al. 2009).

The second class consists of external processes, in which the fresh gas supply from the environment is cut off or removed by the interactions. The main mechanism is “halo quenching” (Silk 1977; Rees & Ostriker 1977; Kereš et al. 2005; Dekel & Birnboim 2006) by which the dark matter halos above a critical mass produce virial shocks that halt the cold gas inflow. In particular, this mechanism produces a population of red-sequence galaxies in the dense region, which seems to agree with the observations (e.g. Baldry et al. 2006; Weinmann et al. 2009). Other examples include ram-pressure stripping or tidal interactions between galaxies.

How galaxies sustain star formation

Numerical simulations have predicted that pristine, metal-poor gas from the cosmic web can be accreted and fuel star formation in disk galaxies (e.g. Dekel and Birnboim 2006; Dekel et al. 2009). The gas originally resides outside the virial radius of the dark-matter halo, and is accreted over cosmic time and becomes the reservoir of fuel for new star formation. There are two modes of gas accretion, mainly depending on the halo mass. When the gas encounters a massive halo ($> 10^{12} M_\odot$), it becomes shock heated and forms

a rarefied hot corona around the galaxy, which requires a long time to cool and settle into the galaxy disk.

For less massive halos, a large fraction of the gas from cosmological accretion remains cold, without being shock heated to the virial temperature. This cool gas streams can quickly falls into the center of the potential well, reaching the inner halo or disk directly. This so-called cold-flow accretion may have a large impact on the disk, or it may provide a gentle gas supply that is transported radially in the disk. As the halos of galaxies at high redshifts have low mass, cold-flow accretion is predicted to be the main mode of galaxy growth during the early epoch of the Universe.

We note that it is difficult to probe gas infall directly. However, the galaxy spectrum provides important clues as to how the newly-accreted gas influences the stellar population in the galaxy. For instance, we would expect the accretion of pristine, metal-poor gas outside might dilute the metallicity of the galaxy. Also, the accreted gas can refuel the galaxy, causing the episodic rather than continuous star formation. In the next section, we introduce the contribution from spectroscopy to the study of galaxy evolution, and introduce stellar population synthesis by which we derive the star formation history of the galaxy.

1.2 What spectra tell us

The spectra of galaxies carry important information about their star formation histories and the chemical evolution of their stellar populations. To set constraints on the formation mechanisms of the stellar populations in galaxies, astronomers build models of chemical evolution and compare them with measurable quantities from spectra. Population synthesis models are the major tool to interpret the integrated spectra of galaxies in terms of their physical parameters, such as stellar mass, mass-to-light ratio, and average stellar age. In this section we give an overview of chemical evolution and population synthesis models.

1.2.1 Metallicities of galaxies

Metals, in astrophysics, are referred to those elements heavier than helium. According to Big Bang theory, hydrogen and helium, and a trace amount of lithium, are synthesized during the first few minutes of the universe . As both the density and temperature of the Universe drops fast after the big bang, further fusion is no longer possible and thus heavier elements are not produced. Instead, other heavy elements are created in nuclear reactions within stars and in supernova explosion. Elements up to carbon and nitrogen are synthesized in the cores of intermediate-mass stars with masses less than $8M_{\odot}$; heavier

elements like silicon upto iron are produced in stars with masses more than $8M_{\odot}$. Elements above iron cannot be formed via stellar nucleosynthesis because the reaction requires the supply of energy. During explosions of core-collapse supernovae, neutron capture reactions take place, leading to the formation of elements heavier than iron. Supernovae also play an important role in the cycle of chemical evolution. The heavy elements produced inside stars are dispersed into the interstellar medium (ISM) through supernova explosion. Another major source for the chemical enrichment of ISM is stellar winds by which massive stars can lose more than half of their mass in their lifetime.

The metallicity (or Z) of an astronomical object, is the ratio of the metal mass to its total baryon mass, which is an approximate measure of its chemical abundance. Metallicity can be determined through (1) interstellar absorption lines (e.g., FeII, MgII), and (2) nebular emission lines (e.g., [OII], [OIII], and [NII]). Below we introduce a common method to measure the metallicity of the galaxy.

Measure gas-phase metallicity

The most popular way to measure the gas-phase metallicity is to estimate its oxygen abundance as oxygen is the most abundant metal in the universe and it displays strong lines in optical. Oxygen abundance, $\log(\epsilon_O)$, is defined as the ratio of the number density of oxygen to the number density of hydrogen (O/H), and is usually scaled to a hydrogen abundance of $\log(\epsilon_H) = 12.0$:

$$\log(\epsilon_O) = 12 + \log(O/H). \quad (1.1)$$

Solar metallicity in this unit is 8.69 (Allende Prieto et al. 2001), and 8.4 and 8.0 for the Large Magellanic Cloud and the Small Magellanic Cloud respectively (Garnett 1999).

From the viewpoint of observations, the estimate of abundance of an element is obtained by measuring the emission-line flux produced by ionized atoms. Accurate abundance measurement for the ionized gas in galaxies requires the determination of the electron temperature (T_e) in this gas. The most reliable determination is made possible by measuring the flux ratio of the [OIII] $\lambda 4363$ line against a lower excitation line, such as [OIII] $\lambda 5007$. The technique is often called the T_e or direct method. However, this method is difficult to carry out for metal-rich galaxies because the electron temperature decreases (as the cooling is via metal lines) and thus [OIII] $\lambda 4363$ line are usually too faint to detect.

Instead, the oxygen abundance can be estimated indirectly from the emission line ratios of different species. These metallicity-sensitive “strong-line” ratios include $[NII]\lambda 6583/H\alpha$, $([OII]\lambda 3727+[OIII]\lambda\lambda 4959,5007)/H\beta$, $[NII]\lambda 6583/[OII]\lambda\lambda 3726,3729$ (e.g., Pettini & Pagel

2004; Kewley & Dopita 2002). These strong-line abundance indicators are typically calibrated by (1) using the samples of nearby galaxies with direct (T_e -based) abundance measurements (e.g. Pagel et al. 1979; Pettini & Pagel 2004) or (2) using photoionization models (e.g., McGaugh 1991; Tremonti et al. 2004).

Galactic chemical evolution

As gas is converted into stars, heavy elements are produced in the nuclei of stars. These elements are partially returned into the interstellar gas at the end of the star's life through stellar winds or supernovae explosions. Some fractions of the metals are locked into the remnant of the star. This cycle indicates that the chemical abundance of the gas in a galaxy should evolve with time. The evolution of chemical abundances in a galaxy thus provides a clock for galactic aging. This evolution is controlled by a variety of parameters, such as the initial gas composition, initial mass function, star formation history, gas infall from cosmic accretion, gas outflows from supernovae, radial transport and mixing of gas within disks, and stellar yields.

Here I briefly introduce the formalism of a simple model of galactic chemical evolution with the assumptions:

- the gas in the galaxy is well-mixed;
- the massive stars return their nucleosynthesis products rapidly, much faster than the time to form a significant fraction of the stars;
- the total mass of the system is conserved, i.e., no exchange of gas with the surrounding environment.

The second approximation is known as the one-zone, instantaneous recycling model; the third approximation is called “closed-box model”, which gives:

$$\frac{dM_{\text{tot}}}{dt} = 0 \quad (1.2)$$

Note that this model assumes that the initial mass of the system is only in gaseous form, and at time $t = 0$, no metals are present. Consider the star formation rate ψ , the returned mass fraction R , which is the mass of gas returned to the ISM from evolved stars, so that the fraction $\alpha = (1 - R)$ of a newly-formed stellar population stays enclosed in stars, i.e., it no longer takes part in the chemical evolution of the ISM afterwards. We further define q as the ratio of the metal mass, which is produced by stars and returned into ISM, to

the initial total mass of the stars. The stellar yield $y = q/\alpha$, is defined as the ratio of the produced metal returned to ISM, to the mass that remains enclosed in stars.

As we have assumed a closed system, the total mass is the sum of stellar mass M_* and gas mass M_g and is constant:

$$\frac{dM_*}{dt} + \frac{dM_g}{dt} = 0 \quad (1.3)$$

The mass of the metals in the ISM is ZM_g and changes when stars are formed. Through the star formation, the mass of the ISM and that of its metals decrease. On the other hand, metals are also returned into ISM by stellar evolution. Under the assumption that timescales of stellar evolution are small, this return process occurs instantaneously.

The differential equation describing the evolution of the metal mass fraction in the ISM is

$$\frac{d(ZM_g)}{dt} = \psi(RZ + q) - Z\psi, \quad (1.4)$$

where the last term is the rate of the metals depleted from the ISM during the star formation process, and the first term describes the return of metals to the ISM by stellar evolution process, which is composed of metals that were already present at the formation of stellar population – a fraction of R of these will be returned – and newly formed metals. As $dM_{*,tot}/dt = \psi$, equation (1.4) can be written as:

$$\frac{d(ZM_g)}{dM_{*,tot}} = (R - 1)Z + q = q - \alpha Z. \quad (1.5)$$

Dividing this equation by α , and using $M_* = \alpha M_{*,tot}$, the yield $y = q/\alpha$, we obtain

$$\frac{dZM_g}{dM_*} = \frac{dM_g}{dM_*}Z + M_g \frac{dZ}{dM_*} = y - Z. \quad (1.6)$$

Equation (1.3) gives $dM_g/dM_* = -1$ and $dZ/dM_* = -dZ/dM_g$, and we thus obtain a simple equation of the metallicity,

$$M_g \frac{dZ}{dM_g} = \frac{dZ}{d\ln M_g} = -y. \quad (1.7)$$

We integrate to obtain the metallicity at time t :

$$Z(t) = y \ln \frac{M_{tot}}{M_g(t)}. \quad (1.8)$$

We can see that the metallicity of the gas only depends on the yield and the gas mass fraction, M_g/M_{tot} . As the gas metallicity and the gas mass fraction are observable

quantities, it is possible to derive an “effective yield” from equation (1.8). If this simple model applies, the derived yield should be equal to the true yield, independent of galaxy mass. This test has been performed by Garnett (2002) on a small sample of 44 nearby spiral and irregular galaxies and by Tremonti et al. (2004) on a large sample of $\sim 53,000$ star-forming galaxies at $z \sim 0.1$ from SDSS. The observation results show that the effective yield and the galaxy mass are highly correlated and the former decreases with the latter sharply below a total mass $\sim 10^{9.5} M_{\odot}$. It is thus clear that galaxies do not evolve as closed boxes. The extent to which the effective yield of a galaxy deviates from its expected true yield reflects the effects of gas infall and outflow on its chemical evolution (Garnett 2002). The fact that low-mass star-forming galaxies have significantly low effective yields suggests that galactic winds play important roles in removing metals from these systems.

1.2.2 The stellar populations of galaxies

The various physical processes occurring in a galaxy leave their imprint on its spectral energy distribution (SED) by changing the global and detailed shape of the spectrum and dominating at different wavelengths. Detailed analysis of the galaxy SED allows us to understand the physical properties of the galaxy. As the light of a galaxy originates from stars within it, a galaxy spectrum is actually made out of the combination of different stellar populations of different ages and metallicities. The straightforward way one might first try to analyse the galaxy spectrum is to decompose them with a linear combination of individual stellar spectra of various types. This method is somehow impractical as the number of free parameters is too large to be constrained by typical galaxy spectra.

If the distribution of the number density of stars is known as a function of their mass, chemical composition, and evolutionary age, we can reduce the free parameters and thus interpret the galaxy spectrum as a superposition of stellar spectra successfully. This is the stellar population synthesis technique (Tinsley 1976; Bruzual & Charlot 1993; Maraston 1998; Vazdekis 1999; Bruzual & Charlot 2003), which is based on the idea that stellar populations with any star formation history can be decomposed into a series of simple stellar populations (SSP, i.e. a single, coeval stellar population formed instantaneously). The main free parameters involved here are the initial mass function, the star formation rate, the chemical enrichment rate. The initial mass function (IMF) is defined as the initial mass distribution at the time of birth of the stars. The star formation rate is the gas mass converted into stars per unit time. The chemical enrichment rate, as discussed previously in Section 1.2.1, characterizes the process in which metals are produced inside the stars and returned to ISM by stellar winds or supernovae. The chemical enrichment must be taken into account in population synthesis studies in a self-consistent form.

Simple stellar population

The starting point of any stellar population synthesis model is the simple stellar population at a single metallicity and abundance pattern. Let $\psi(t)$ be the star formation rate, $S_{\lambda,Z}(t')$ be the spectral energy distribution of an SSP of initial metallicity Z and age t' . The function $S_{\lambda,Z(t-t')}(t')$, which describes this emission at any time point t , accounts for the different evolutionary tracks of the stars in the Hertzsprung-Russell diagram (isochrones)¹. Then the total spectral energy distribution of a simple stellar population at a time t can be written as:

$$F_{\lambda}(t) = \int_0^t \psi(t-t') S_{\lambda,Z(t-t')}(t') dt. \quad (1.9)$$

To calculate S_{λ} , one needs the stellar evolution prescription, which calculates the stellar evolutionary tracks of stars from the hydrogen burning limit ($\approx 0.1M_{\odot}$), to the maximum stellar mass ($\approx 100M_{\odot}$), and the stellar spectral libraries, which convert the outputs of stellar evolution calculations – surface gravities and effective temperatures – as a function of metallicity into observable SEDs. Both theoretical stellar atmosphere libraries and empirical stellar spectra based on observations can be used. However, observational stellar libraries are limited to the stars in the solar neighborhood, and thus they give incomplete coverage of parameter space. For example, hot main-sequence stars at low metallicity are very rare, so are stars in rapid phases of stellar evolution such as thermal pulse asymptotic giant branch (TP-AGB) stars.

Figure 1.1 illustrates the SEDs of an SSP for solar metallicity at various ages, from 10^6 yr to 13 Gyr. The spectrum of a young stellar population is dominated by short-lived, massive stars that emit strong ultraviolet (UV) radiation, below 2000Å. As the most massive stars leave the main-sequence and evolve into red giant stars around 10^7 years, the UV emission decreases and the near-infrared (IR) emission increases. The UV emission starts to rise again from 0.1 to 13 Gyr because of the accumulation of low-mass, post-AGB stars. It is remarkable to see that the shapes of SEDs at ages from 4 to 13 Gyr remain unchanged. The reason is that low-mass stars evolve within a narrow temperature range from the main-sequence to the end of AGB phase. The spectral evolution can be studied also by the strength of stellar absorption lines. For instance, between 0.1 and 1 Gyr, there is a marked features of all the Balmer lines from H α 6563Å to the continuum limit at 3646Å). The strength of the Balmer lines is a powerful diagnostic tool of recent burst of star formation. Another important spectral feature is the 4000Å-break which arises from the prominence in cool stars of many metallic lines blueward of 4000Å. This feature is

¹Hertzsprung-Russel diagram is a scatter graph of stars showing the relation between their absolute magnitudes or luminosities versus their spectral classifications or effective temperatures

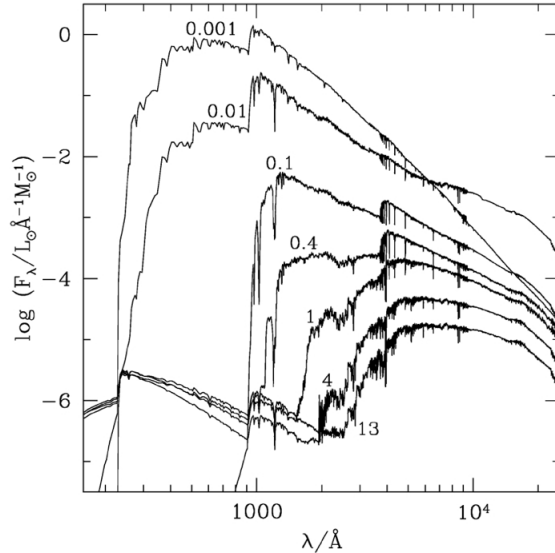


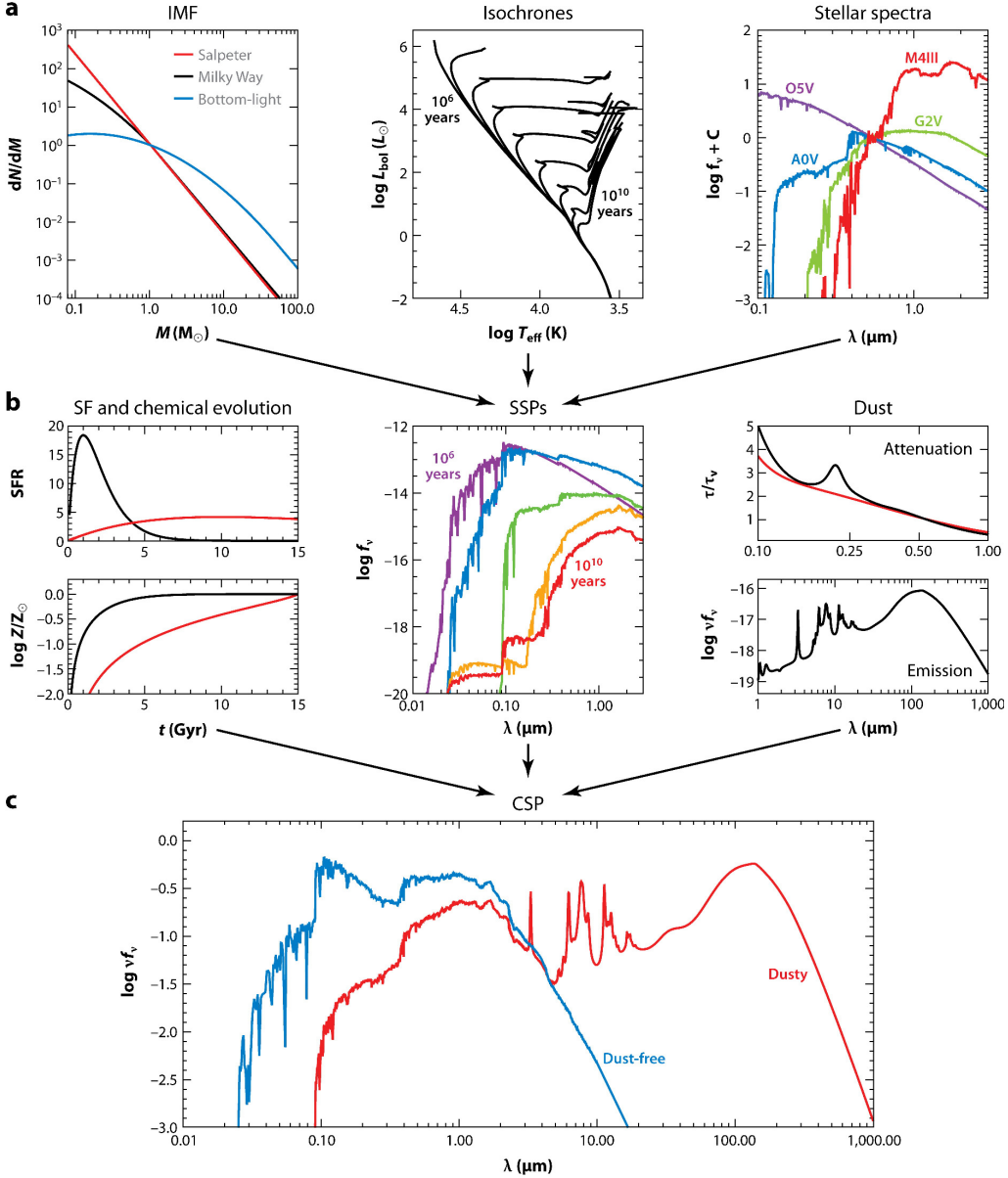
Figure 1.1: Spectral evolution of a simple stellar population of solar metallicity. Ages are indicated next to the spectra (in Gyr). [Figure taken from Bruzual & Charlot (2003)]

widely used as age indicator, but it shows also a dependence on metallicity at old ages. Although the spectral continuum shapes of SEDs look unevolving at ages from 4 to 13 Gyr, the strengths of many absorption lines evolve/change significantly during this time range. The strengths of absorption lines react to the differences in age and metallicity, which hence can potentially help to resolve the age-metallicity degeneracy.

Composite stellar populations

The processes to construct the SEDs of composite stellar populations (CSP) are summarized in Figure 1.2. Compared to SSP, CSPs include more sophisticated, realistic ingredients in their construction. First, they contain stars with a range of ages characterized by their star formation history (SFH). Second, they contain stars with a range in metallicities given by their time-dependent metallicity distribution function. Third, they contain dust.

The SFHs of galaxies can be arbitrarily complex; however, a simple form of SFH in which SFR decays exponentially with time, is usually adopted. This form is based on the idea that SFR correlates linearly with the gas density in a closed-box model. As we know that galaxies do not simply follow the closed-box model but rather interact with environments, superimposing additional bursts of star formations upon continuous models could be used to further understand the star formation histories among different types of galaxies (e.g., Kauffmann 2003a). In Chapter 2, I also add starburst modes of star formation upon continuous models and compare them with the observational spectra to



 Conroy C. 2013.
Annu. Rev. Astron. Astrophys. 51:393–455

Figure 1.2: Summary of the stellar population synthesis technique. The first row (a) includes the ingredients needed to construct simple stellar populations (SSP): an initial mass function, isochrones for different ages and metallicities, and stellar spectra for different spectral types. The second row (b) are the necessary components to construct composite stellar populations (CSP): star formation histories and chemical evolution, SSPs, and a model for dust attenuation and emission. The third raw (c) shows the final CSPs with and without the dust model. [Figure taken from Conroy (2013)]

derive the recently-formed stellar mass for ~ 200 nearby galaxies.

The distribution function of metallicity in CSPs is usually very simplistic. The common treatment is using a δ -function; that is, a single metallicity value is adopted for the entire composite populations.

Dust is prevalent in galaxies and plays a dual role in stellar population synthesis models – dust obscures the emission in UV through NIR and emits the light in the IR regime. Our understanding of interstellar dust mostly comes from the local observations within our own Galaxy and the Magellanic clouds, and from theoretical and experimental laboratory works. The size distribution of dust grains is a power law in nature with the index ~ -3.5 , sustained by the theory and observation. The average cross-section is dominated by small grains while the mass is dominated by large grains. The size distribution and types of dust are convolved with absorption/emission cross-sections, scattering cross-sections, and phase functions which are determined by laboratory works and Mie theory (see Draine & Li 2007). These data form the dust models used often in SED modelling. Besides, empirically-based laws and templates are also used in SED modeling, such as the Milky way extinction law or Calzetti law (Calzetti 1997).

The ultimate goal of stellar population synthesis is to fit to the observed SEDs of galaxies and to derive their physical properties, such as stellar masses, specific star formation rate, star formation histories, stellar ages, dust masses, and chemical abundance. Studying these parameters among different types of galaxies in different environments or/and across cosmic time, and comparing them with other properties from multi-wavelength data, such as the cold or hot gas content, have made significant contribution to the observational understanding of galaxy formation and evolution.

1.3 Gas and star formation in galaxies

The interstellar medium fills the space between the stars. The total mass of the interstellar medium, including abundant gas and little dust, is about 15% of the total mass of visible matter in our own Galaxy. Of the gas in the Milky way, 90% by mass is hydrogen, with the rest mostly helium. The interstellar gas appears mainly in two forms: cold clouds of neutral atomic and molecular hydrogen, and hot ionized gas around young stars. The cold gas is the fuel for star formation, and the process plays a key role in galaxy evolution. In this section, we first give an introduction of various components of the ISM, and then focus on the molecular gas and its connection with the star formation.

1.3.1 ISM in general

Astronomers were aware of the existence of the ISM by the absence of stars in some dark areas of the Milky way. Such dark patches result from the starlight being blocked from sight by the interstellar dust absorption in-between. Matter inside stars is mainly in ionized states because of high temperatures. The ISM, on the other hand, is in a wide range of physical conditions, and mainly consists of atomic, molecular, ionized gas, and dust at various temperatures. The ratio of gas to dust is about 99 to 1 %.

From a variety of observations, the distribution of different components of the ISM can be mapped. Generally speaking, the discrete interstellar clouds are concentrated in spiral arms, and they occupy a small interstellar volume. While most of the mass in the ISM is contained in the cold component, most of the space is occupied by a hot, ionized component. The ISM also likely includes the transition phase of a warm component, either in a neutral or an ionized state.

In this section I give an introduction of different components of ISM and their general properties. As my studies have focused on molecular gas in nearby galaxies, I will give a more detailed overview of molecular gas observations in next section.

Atomic neutral gas

The atomic neutral gas includes most of the mass of the ISM. The neutral medium is best defined by the absence of hydrogen Lyman continuum photons, so that hydrogen is neutral. There are three main observables to study this component: (1) 21-cm line of atomic hydrogen which traces the main constituent and allows us to measure its temperature; (2) the interstellar absorption lines that provide the information of chemical composition and some physical parameters; (3) the fine-structure lines in far-IR band which are the cooling source for the gas.

There are several important results we obtain by emission and absorption measurements of the 21-cm lines. The information given by 21-cm lines includes the mass, the distribution and the kinematics of atomic gas in our own Milky way and external galaxies. It is usually assumed that the 21-cm line is optical thin (i.e., the photons produced in a emitting source can all escape from it), which might not apply to all the cases. Thus, we should keep in mind that the HI mass obtained in this way is a lower limit. Besides, we know that the atomic gas is very inhomogeneous; the 21-cm emission is dominated by filaments, sheets, and shells. There are two phases of the atomic interstellar medium. One is warm and diffuse ($n_{\text{H}} \approx 0.1 - 0.3 \text{ cm}^{-3}$, $T \approx 8000 \text{ K}$), called the warm neutral medium (WNM). The other is cold and dense ($n_{\text{H}} \approx 10 - 50 \text{ cm}^{-3}$, $T \approx 100 \text{ K}$), called the cold neutral medium (CNM). The WNM is extended in interstellar space while the CNM forms discrete, inhomogeneous and

structured filaments, which is thought to be due to turbulence. Finally, there exists high-velocity neutral gas that falls onto the galactic plane with velocities from a few km s^{-1} to several hundreds of km s^{-1} at high galactic latitudes. Its origin might be of extragalactic source, or more likely the hot ionized gas ejected by supernovae and bubbles from the galactic disk falling back onto the disk while cooling and recombining.

Molecular gas

The molecular species range in size from 2 to 13 atoms. They are usually found in dense interstellar clouds with sizes of 1-100 light years, average gas densities of $10^2 - 10^3 \text{ cm}^{-3}$, and temperature of 10 – 60K. Today, more than 120 different molecules are discovered in the ISM. Molecular hydrogen, H_2 , stands out to be the most abundant interstellar molecule, which is partly due to the high elemental abundance of hydrogen compared with other heavy elements found in molecules, and partly to an efficient chemical pathway for its formation from hydrogen atoms. The H_2 molecule forms on the surfaces of dust grains in the ISM, and also the dust grains provide shielding from UV radiation field, allowing the atoms to be cool and to form molecules. The second most abundant molecule, CO, has a fractional abundance with respect to H_2 of 10^{-4} . Most of the remaining molecules are organic or carbon containing in nature; all organic molecules have much smaller fractional abundances than CO ($< 10^{-8}$) and can be regarded as trace constituents.

In contrast to atoms with electronic transition only, molecules have three types of transitions: electronic, vibrational and rotational. The vibrational transitions of diatomic molecules result from stretching mode. More complex molecules also have bending and deformation modes. Vibrational energies are typically a fraction of an eV, and they are generally in the near-infrared. The vibrational transitions of H_2 have been much observed from ground and space, in addition to those of CO and of H_2O . Rotation can be a global rotation around the principal axes of inertia, or some internal rotation for complex molecules. The energies of the rotational transitions are of the order of meV, and the wavelengths are in the submillimeter to centimeter range, except for H_2 .

The energy of molecular electronic transitions is of the order of several eV, with corresponding wavelengths in UV. For instance, all the electronic transitions of H_2 are at $\lambda < 115\text{nm}$. Very few simple molecules have transitions in the optical which is visible from ground; as such the discovery of interstellar molecules has been relatively late. Most of the molecular gas is confined in large and dense clouds with abundant dust. As the gas and dust become so thick in molecular clouds that the UV extinction is too large to accurately measure all of the H_2 gas in the interior of the cloud. Because of this limitation, in combination with the fact that, the H_2 molecule is a symmetric rotator without a permanent

dipole moment and thus without permitted transitions in the radio regime, the most useful tracer of molecular gas has long been the molecule CO, which has a $J = 1 \rightarrow 0$ rotational transition at 2.6mm (115 GHz) and higher-level transitions at higher frequencies. We will discuss more about CO observations and results in galaxies in next section.

Ionized gas

The ISM can be ionized by the UV photons of hot stars or by other mechanisms such as collisional ionization in shocks, X-ray ionization or high-energy charged particles. There are three kinds of ionized ISM in general: HII region or gaseous nebulae, which are well-defined entities surrounding hot stars; the diffuse ionized medium; the hot ISM, most of which comes from supernova remnants and bubbles that permeate the general medium.

The lowest energy required to ionize hydrogen is 13.6 eV, corresponding to the UV regime. The young and hot stars, such as O- or B-type stars emit large amounts of UV photons and ionize hydrogen or helium around them. An ideal HII region is an ionized sphere surrounding a hot star or a cluster of hot stars, called “Strömgren sphere”. The Strömgren sphere is defined as a region inside which the number of atom photoionization by the UV radiation is equal to the number of recombination of the ions with free electrons. The radius of a Strömgren sphere around a uniform medium of hydrogen is:

$$R_S = \left(\frac{3N_*}{4\pi\alpha n_H^2} \right)^{\frac{1}{3}}, \quad (1.10)$$

where N_* is the number of ionizing photons from star per second, n_H is the number density of neutral hydrogen, and α is the recombination coefficient, with a value of $\alpha = 2.6 \times 10^{-13} \text{cm}^3 \text{s}^{-1}$ at a temperature $\sim 10^4 \text{K}$. An O5 star with $N_* = 5 \times 10^{49} \text{s}^{-1}$, if embedded in a cool neutral cloud with $n_H \approx 30 \text{cm}^{-3}$, will generate an HII region with $\sim 10 \text{pc}$ in radius.

Outside well-defined HII region, the ISM has diffuse ionized gas which might originate either from leaks of ionized gas out of HII region, or from ionization by the UV photons of isolated hot stars. In our Galaxy, the diffuse ionized gas contains much more mass than the HII region. Its total mass is of the order of 1/3 of HI mass.

As early as 1956, the existence of hot gas with temperature $> 10^6 \text{K}$ in our Galaxy was predicted. In 1968 a diffuse emission in soft X-rays was discovered and attributed to this gas (Bowyer et al. 1968). Later, absorption lines of OVI at 1032, 1038 Å, X-ray emission lines of OVI and OVII were also observed. All these observations show the existence of a hot diffuse gas at temperatures of a few 10^5 K to 10^7K . This hot gas comes from supernova remnants and bubbles, and could reach very high Galactic altitudes, occupying some 80-90% of the volume in the Galactic disk. As aforementioned, the hot gas is associated with

the high-velocity neutral clouds that fall into the potential well of our Galaxy. This hot gas could come from photoionization by a diffuse UV background, or it could be a thermally unstable front between the cold gas in the neutral clouds and an even hotter gaseous halo.

Dust

Dust grains are formed in the atmospheres of evolved stars, novae, and supernovae, and are destroyed and re-formed in the ISM. With sizes from nanometres to micrometres, they are very well mixed with the ISM. Dust plays an extremely important role in the physics and chemistry of the ISM, although it only makes up about one hundredth of the mass of the ISM. For instance, dust acts as a catalyst. Atoms or molecules can stick on the dust grains and form a surface “mantle” of “ices” where chemical reactions can occur. In particular, the H₂ molecule can only form on dust grains. Heating of the dust grains can evaporate the mantle and release new molecules into the ISM. The destruction of dust also returns heavy elements back to the ISM. Moreover, dust grains irradiated by UV photons can release electrons by the photoelectric effect. These electrons are crucial to the heating of the ISM. For particle densities $> 10^4 \text{ cm}^{-3}$, collisions can efficiently transfer energy from the gas to dust and vice versa.

The most straightforward way to observe dust in our Galaxy is using its extinction effect on background luminous sources. Many stars on the galactic plane are redder than expected based on their spectral types. The increasing degree of absorption or scattering at shorter wavelengths is known as selective extinction. We can build a so-called extinction curve by calculating the degree to which the observed and expected magnitudes differ as a function of wavelength. By studying extinction curves we can derive the composition and sizes of the interstellar dust. For example, a bump shown in the extinction curve in UV, around 217 nm, indicates the presence of graphite particles; the extinction in infrared suggest the presence of silicates. Dust grains can also be directly detected via their self-emission. They absorb UV photons and re-emit them in infrared. From the peak radiation wavelength given by the Wien’s law, we can infer the temperature of the dust, with typical temperatures ranging from 10 to 100 K.

1.3.2 H₂ observations

As mentioned in the above section, CO molecules are commonly used to trace H₂ gas. CO has a weak permanent dipole moment, and its low excitation energy ($h\nu \approx 5.53\text{K}$) leads to its excitation at the densities and temperatures present in molecular clouds. In particular, the CO(1-0) integrated line intensity is roughly linearly related to the H₂ column density

based on theoretical and observational studies.

CO as H₂ tracer

The main justification of using CO to tracer H₂ mass is the virial hypothesis. The CO line profile provides the velocity width ΔV of molecular clouds; for a uniform, spherical cloud of size R, the virial mass can be derived, proportional to $\Delta V^2 R$. Based on observations, there indeed exists a strong correlation between CO luminosities and the H₂ masses (i.e. H₂ column densities) for Galactic molecular clouds (e.g., Scoville et al. 1987; Solomon et al. 1987). Let us write the relation by

$$\frac{N(H_2)}{\text{cm}^{-2}} = X_{\text{CO}} \frac{I_{\text{CO}}}{\text{K km s}^{-1}}, \quad (1.11)$$

where N(H₂) is the column density of molecular hydrogen, I_{CO} is the intensity of the CO(1-0) rotational transition line, and X_{CO} is the ratio between these two quantities, called CO-to-H₂ conversion factor. Several methods have been used to estimate the H₂ column density and thus determine the X_{CO} factor, including analysis using virial masses, CO isotopologues (e.g., ¹²C¹⁸O, ¹³C¹⁶O, ¹³C¹⁸O), dust extinction and diffuse γ -ray radiation. The most widely-used values for X_{CO} come from the studies in the Milky Way, and lie in the range $\approx 2 - 3 \times 10^{20} \text{ cm}^{-2} (\text{K km s}^{-1})^{-1}$.

However, the X_{CO} factor is sensitive to local physical parameters, such as density or metallicity. CO is inherently more fragile to the destructive UV radiation field. Because H₂ is plentiful, it can self-shield: H₂ molecules at the surfaces of the clouds can absorb the dissociating photons, leaving molecules in the interior intact. CO is far less abundant, so it cannot self-shield. Instead, CO is protected from dissociation by dust grains which absorb the CO-dissociating photons before they can reach a CO molecule. The amount of dust in a galaxy usually scales linearly with metallicity, which indicates that CO is more easily dissociated in low metallicity environments. We note that, studies of other normal galaxies have return X_{CO} values similar to the Galactic one. Significant departures from the Galactic conversion factor are seen only below metallicity $\sim 1/3 - 1/2$ solar (see review in Bolatto, Wolfire, & Leroy 2013). On the other hand, CO will saturate at modest column densities due to its high optical depth, so it is not useful for tracing molecular gas at high densities ($n_H > 10^3 \text{ cm}^{-3}$).

H₂ content in galaxies

CO Line emission from the external galaxies was first detected in 70s (Rickard et al. 1975; Solomon & de Zafra 1975; Combes et al. 1977). Since 80s, there have been many CO

surveys of nearby galaxies using single-dish telescopes. For example, the large surveys included FCRAO Extragalactic CO Survey (Young et al. 1995), which measured the CO $J = 1 \rightarrow 0$ line in 300 nearby galaxies, and more recently, the COLD GASS survey (Saintonge et al. 2011), which targeted ~ 360 galaxies with stellar masses $10.0 < \log M_*/M_\odot < 11.5$, at redshifts $0.025 < z < 0.05$. Up to now, CO data for more than 1500 local galaxies are available. There are also a few CO interferometric surveys for local galaxies, such as BIMA-SONG (Helfer et al. 2003), HERACLES (Leroy et al. 2008). The interferometric surveys yield high-resolution (from ~ 1 to 13 arcsec) CO gas maps and allows us to study the distribution of molecular gas in external galaxies.

It has been shown early that the ratio of H₂ and HI masses, $M_{\text{H}_2}/M_{\text{HI}}$, depended on Hubble type (e.g., Young& Knezev 1989; Sage et al. 1993). The early-type galaxies, such as Sa type, have higher ratios ~ 1 while the late-type galaxies have lower ratios ~ 0.1 . However, Casoli et al. (1998) found that the molecular to atomic gas ratio showed a constant value from Sa to Sc, and a factor of 10 decrease for late-types, beginning at Sc. In fact, the trend between the $M_{\text{H}_2}/M_{\text{HI}}$ and the Hubble type disappeared when only the massive galaxies were considered. This suggested that the trend with Hubble type might be due to the dependence of metallicity as the low-mass galaxies usually have low metallicity. We note that the sample of the above studies was either small, inhomogeneous or biased towards a particular galaxy type (e.g., the spiral type or infrared-bright objects).

On the other hand, the COLD GASS sample, covering a wide range of galaxy parameters, is much more uniform and unbiased, which allows us to study the scaling relations between the molecular gas and other galaxy properties quantitatively. First, the molecular-to-atomic mass ratio has a mean value of 0.3 over the entire sample and weakly increases with the stellar mass and stellar surface density with large scatters. The molecular gas mass fractions, M_{H_2}/M_* , are in the range of 0.009 – 0.2, with a mean value 0.066 ± 0.039 . Most interestingly, there exists a sharp thresholds in galaxy structural parameters such as stellar surface mass density and concentration index, below which all galaxies have a measurable cold gas component (HI and CO) but above which the detection rate of the CO line drops suddenly. This seems to suggest that the quenching processes in galaxies are associated with a change in their structures.

In addition to global properties of molecular gas, the resolved CO maps give us insights into the distributions of molecular gas in galaxies. Unlike HI, which is usually much more extended than the galaxy disk, molecular gas is most concentrated in the center of the disk, where average ISM densities are higher due to the deeper gravitational potential. Globally, the $M(\text{H}_2)/M(\text{HI})$ ratio ranges from 0.1 to 1 while $M(\text{H}_2)/M(\text{HI})$ could be larger than 10 in the center of galaxies. The molecular gas distributions decline monotonically with galaxy-

centric radius; the H₂ radial profile can be described by the exponential function well. In contrast with HI, the molecular gas distribution follows the star formation closely. In the next section we will discuss the relation between cold gas and star formation.

1.3.3 H₂ gas and star formation

One of the most fundamental questions in modern astrophysics is how galaxies convert their gas into stars, and how this process may change with the galaxy internal properties or galactic environments. Understanding of this process is a necessary prerequisite for a complete theory of galaxy formation and evolution across cosmic time. Numerous observational studies have attempted to find out empirical laws to describe the relationship between the star formation rate and the gas mass. These empirical results are essential inputs to constrain the relative importance of various physical processes governing the star formation rate. In this section, we give an overview of the current picture of star formation and cold gas.

Historical review of star formation law

A pioneering work of quantifying how gas turns into stars can date back to a half-century ago. Schmidt (1959) suggested that the relation between the gas and SFR densities could be characterized by power laws:

$$\rho_{\text{SFR}} \propto \rho_{\text{gas}}^n, \quad (1.12)$$

or

$$\Sigma_{\text{SFR}} \propto \Sigma_{\text{gas}}^N, \quad (1.13)$$

where ρ_{SFR} and ρ_{gas} are the volume densities of the SFR and the gas, and Σ_{SFR} and Σ_{gas} are the surface densities of the SFR and the gas. The later relation is more commonly used nowadays as they are directly measurable quantities in external galaxies. Schmidt (1959) built a self-consistent model for the evolution of stellar and gas masses by assuming a constant initial luminosity function for stars, a star formation rate $f(t)$ that depends on a power n of the gas density, a star above 0.7 solar mass returning all mass into gas and becoming white dwarf after main sequence stage. He argued that a more direct evidence was to study the distributions of atomic gas and young stars perpendicular to the galactic plane, which gave a power-law index of $n \approx 2 - 3$. He also suggested that, for $n = 2$ or larger, the giant ellipticals with high mean density would have low gas mass, high helium abundance and a red color. On the other hand, a system with lower mean density such as Small Magellanic Cloud should have high gas mass, high helium abundance and a bluish color.

Since the publication of Schmidt's original work, many authors have attempted to study the Schmidt law outside our own Milky Way. Sanduleak (1969) studied the correlation between the densities of bright stars and atomic hydrogen gas in Small Magellanic Cloud and reported $N = 1.84 \pm 0.14$. Hartwick (1971) found $N = 3.50 \pm 0.12$ for M31 with the distribution maps of HII regions and HI gas. By using stars and HII regions together to trace star formation and HI observation for gas, Madore et al.(1974) found that the power-law index N was higher in the outer region than in the inner region for M33. Tosa & Hamajima (1975) compared HII regions to HI gas in M31 and the Large Magellanic Cloud (LMC), and also performed the same analyses in seven nearby galaxies later (Hamajima & Tosa 1975). They obtained power-law indices $N = 1.5 - 1.9$ and found radial variations in N value.

With the availability of CO observations for a larger sample, Buat, Deharveng & Donas (1989) used UV emission of 28 late-type galaxies as the SFR tracer and compared to their molecular and atomic gas assuming a galactic standard CO-to-H₂ conversion factor, $X_{\text{CO}} = 2.3 \times 10^{20} \text{ cm}^{-2} (\text{K km s}^{-1})^{-1}$ (Strong et al. 1988). They found that the correlation of the SFR is very good with the HI + H₂ gas surface density, better than HI or H₂ gas alone. The index N they derived in Schmidt's law varied from 1 to 1.6 depending on whether the extinction corrections on UV emission were constant or depended on the gas content. Kennicutt (1989) also looked at the relation between SFR and HI + H₂ but used H _{α} emission line as SFR tracer. He looked at the radial profiles of the Schmidt relation for 15 galaxies and found that in dense regions the SFR and total gas surface densities were well represented by a power-law relation with index $N = 1.3 \pm 0.3$.

Finally, a breakthrough occurred in 1998 when much more data of extinction-corrected SFR, CO and HI gas maps were obtained. Kennicutt (1998) extended his previous work with a comprehensive study on 61 normal galaxies and 36 starburst galaxies. As shown in Figure 1.3, he found $N \sim 1.4$ on global scale for the normal and starburst galaxies using H _{α} as star formation rate indicator and CO, HI emission as the total gas tracer. The slope found in Kennicutt (1998) could be simply explained by gravitational instability: if stars are formed constantly each free-fall time and gas scale height is assumably constant, N is equal to 1.5 (e.g., Madore 1977; Elmegreen 1994). Nowadays such relations are often called the Kennicutt-Schmidt (K-S) laws.

We note that the previous studies were based on different SFR and gas tracers; these systematic variations might contribute to the varieties and scatters of N values. First of all, the molecular gas, rather than the total or atomic gas, is thought to be linked directly to the star formation. Wong & Blitz (2002) found a roughly linear correlation between Σ_{SFR} and Σ_{H_2} for 7 gas-rich spiral galaxies using the H _{α} and CO observations. In Gao and

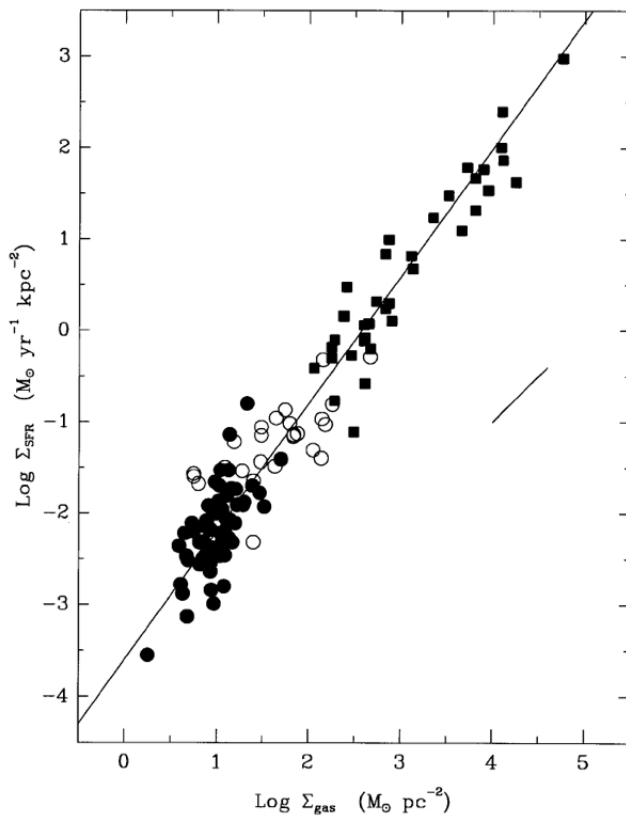


Figure 1.3: Relationships between the disk-averaged surface densities of star formation and gas (atomic and molecular) for normal disk (filled circles) and starburst (squares) galaxies. The line is a least-square fit with power-law index $N = 1.4$. [Figure taken from Kennicutt (1998)]

Solomon (2004), they showed that FIR luminosities of disk and starburst galaxies were linearly correlated with their luminosities of HCN emission that traced dense molecular gas clouds ($n(H_2) > 10^4 \text{ cm}^{-3}$). Later on, Wu et al. (2005) compared FIR and HCN luminosities of massive giant molecular clouds (GMCs) in the Milky Way and found a linear correlation between these two quantities as well. This tight correlation between the SFR and the dense molecular clouds on small scale extended smoothly to that found by Gao and Solomon (2004) for galaxies, spanning over 7–8 orders of magnitude in infrared luminosities.

The differences of the power-law index in Schmidt's law between H₂- and HI-dominated regions were shown clearly in the Figure 1.4 taken from Bigiel et al. (2008). For regions with $\Sigma_{\text{gas}} > 10 M_\odot \text{ pc}^{-2}$, the K-S law seems to be linear up to $\Sigma_{\text{gas}} \approx 100 M_\odot \text{ pc}^{-2}$. However, for regions with $\Sigma_{\text{gas}} < 10 M_\odot \text{ pc}^{-2}$, where the gas is dominated by HI, the K-S slope becomes steepened. Σ_{HI} seems to saturates at $\sim 10 M_\odot \text{ pc}^{-2}$. The combination of HI and H₂ gas in the measurement of Σ_{gas} tends to dilute the star formation in HI-dominated regions, such as outskirts of disk galaxies.

These studies suggested that the young stars were born in molecular gas exclusively; the atomic gas was inert to the star formation process. Thus, in this thesis I mainly focus on the relation between the molecular gas and SFR or the molecular gas depletion time, defined as molecular gas mass divided by SFR.

Secondly, the discrepancy among different studies might also come from the use of SFR indicators. Extensive efforts have been made to calibrate star formation at different wavelength (see reviews by Kennicutt 1998; Kennicutt & Evans 2012). UV continuum, H α recombination lines are conventionally used although the correction of dust attenuation is never trivial and needs to be calibrated with care. H α emission comes directly from the HII region ionized by young and massive stars with the lifetime of ~ 10 Myr. Its dust extinction can be calibrated well by Balmer decrement. H α emission is deemed as an ideal star formation indicator as it provides a nearly instantaneous measure of the star formation. Due to the fact that spectroscopy is much more time-consuming than photometry, no survey data with the former technique is available yet for a large, uniform and unbiased sample in extragalactic studies, except SDSS, which however observed only the central 3 arcsec region of galaxies.

Considering the availability, an alternative of star formation tracer is UV continuum: the launch of GALEX has mapped the sky in the NUV and FUV bands with both the scope (e.g, All-sky-Imaging Survey or AIS) and depth (e.g., Deep Imaging Survey or DIS). FUV traces the bulks of the emission from massive stars formed over the past ~ 100 Myr after the gas around the star birth place is dispersed. A good indicator of the amount of

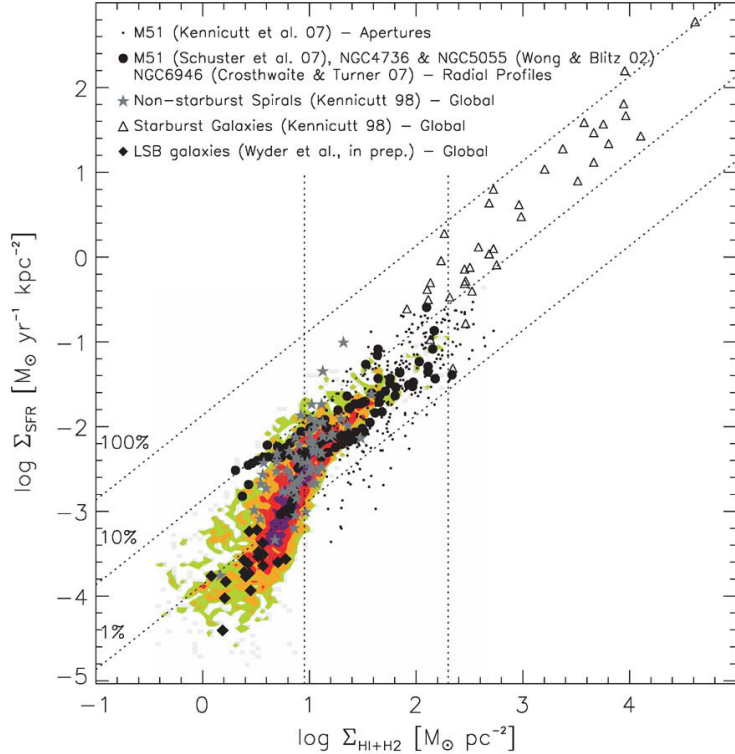


Figure 1.4: The star formation law for nearby galaxies on sub-kpc scale. Colored regions indicate data density of 750kpc regions in seven nearby spiral galaxies (Bigiel et al. 2008); black dots are individual apertures in M51 (Kennicutt et al. 2007); black circles show radial profiles from 4 nearby spirals. Filled gray stars are the global measurements of 61 normal spirals and triangles of 36 starburst galaxies (Kennicutt 1998). Black filled diamonds are the global measurements for 20 low surface brightness galaxies (Wyder et al. 2009). All data have been adjusted to a common IMF, CO line ratio, CO-to-H₂ conversion factor, and galaxy inclination. [Figure taken from Bigiel et al. (2008)]

FUV attenuation is the ratio of total IR (TIR) to UV emission (Infrared excess or IRX), which is shown to be more reliable to estimate the dust attenuation than others, such as FUV-NUV color (e.g., Cordon et al. 2000; Bell 2003; Hao et al. 2011). As shown in Hao et al. (2011), the IRX-corrected FUV luminosities are linearly correlated with dust-corrected H α luminosities. The idea of using IRX is based on the energy balance: The UV photons are absorbed by surrounding dust; the heating dust re-emits the energy obtained from stars in the IR regime.

Since the dust-reprocessed emission from young stars emerges mainly at IR, the IR is considered as a reliable tracer of star formation activity. Many studies have tried to calibrate the star formation rate based on the total IR luminosity or monochromatic emission, mainly 24 or 70 μm fluxes. In order to probe both the unobscured stellar emission in FUV/optical and the dust-reprocessed emission at IR, the combination of SFR tracers has been proposed to be more accurate than FUV, H α , or IR alone (e.g., Calzetti 2007; Hao et al. 2011). This method could also spare the long-term struggle for correcting the extinction effect in UV/optical regime. In our works, I improve the measurements of star formation rates by adopting a combination of FUV and mid-IR data.

The modern molecular star formation law

Only the last decade exploded multiwavelength data for nearby galaxies, including the GALEX Nearby Galaxy Survey (Gil de Paz et al. 2007), the Spitzer Infrared Nearby Galaxies Survey (SINGS; Kennicutt et al. 2003), The HI Nearby Galaxy Survey (THIGHS; Walter et al. 2008), and The HERA CO Line Extragalactic Survey (HERACLES; Leroy et al. 2008). These observations provided high-resolution, multiwavelength images of nearby galaxies for spatially-resolved, sensitive measurements of Σ_{gas} and Σ_{SFR} .

Two recent studies have exploited these data sets and aimed at exploring the “spatially resolved” star formation law throughout the disks of nearby galaxies. Kennicutt et al. (2007) used a combination of narrow-band H α plus 24 μm photometric images to measure Σ_{SFR} , and 21cm plus CO(J=1-0) maps to measure Σ_{gas} for 257 star-forming regions with 520 pc in diameter in the disk of NGC 5194. They derived slopes of $N = 1.37 \pm 0.03$ and $N = 1.56 \pm 0.04$ for the molecular and total gas Kennicutt-Schmidt law respectively.

Bigiel et al. (2008) first obtained a large sample of nearby galaxies to study the star formation law at sub-kpc resolutions. They explored the correlation between Σ_{SFR} estimated from FUV+24 μm and Σ_{H_2} derived from CO (J=2-1) on sub-kpc scales using a sample of 18 nearby spiral galaxies from the HERACLES project (Leroy et al. 2008). They reported a constant star formation efficiency with the timescale for conversion from H $_2$ to stars $\sim 2\text{Gyr}$ among these spirals. Leroy et al. (2008) compared these new data with various theoretical

models. They found that the depletion timescales in molecular gas is universally $\sim 2\text{Gyr}$, independent of local or global conditions, such as the free fall or orbital timescales, mid-plane gas pressure, state of disk stability, and regardless of the rate of shear of the ability of the gas phase to form. Their results seemingly suggested that star formation is likely to be a localised process linked to the quantity of molecular gas only, and it proceeds at a fixed rate per molecule.

Some subsequent works, however, reported non-linear relations between Σ_{SFR} and Σ_{H_2} either using different fitting methods on the same data (Shetty et al. 2013) or new observational data (e.g., Momose et al. 2013; Pan et al. 2014). In Shetty et al. (2013), these authors developed a Bayesian linear regression method that rigorously treats measurement uncertainties and accounts for hierarchical data structure. They then applied this method to estimate the Kennicutt-Schmidt parameters of a sample of spiral galaxies compiled by Bigiel et al. (2008) and found significant variation in the KS parameters. This showed that the relations between molecular gas and star formation vary from galaxy to galaxy, indicating non-constant molecular gas depletion time.

On the other hand, Momose et al.(2013) found a super-linear Kennicutt-Schmidt law with $N = 1.3 - 1.8$, based on new CO ($J=1-0$) and $\text{H}\alpha+24\mu\text{m}$ data of 10 nearby spiral galaxies at sub-kpc resolution. They argued that star formation efficiency of the disks depends on the bulk molecular gas: the stars are forming more efficiently in the region where the gas surface density is higher. They speculated that the difference between their findings and the HERACLES results was due to the use of different CO tracers. CO($J = 2-1$) was used as a tracer of molecular gas mass in Bigiel et al. (2008) while CO ($J=1-0$) was used in Momose et al. (2013) . If CO($J = 2-1$) is enhanced in regions with higher star formation (and hence higher excitation), CO($J = 2-1$) may not trace the underlying molecular gas mass in a linear way. In Pan et al. (2014), they found that the power-law index N of the K-S relation rises towards the center of IC 342: $N \sim 1.4$ in the disc with low Σ_{H_2} and $N \sim 2-3$ in the galactic center with high Σ_{H_2} . As the evidence of shocks produced by cloud-cloud collisions was found in the center of IC 342 (Meier & Turner 2005), they suggested that the star-formation of the disc is dominated by gravitational instabilities while the combination of gravitational instabilities and cloud-cloud collisions is favored for the star formation in the center of IC 342.

It is still not clear whether there is a universal star formation timescale from the molecular gas or not. However, we note that most studies have mainly focused on the disk regions of star-forming spiral galaxies. The uniformity and the relatively small number of the sample might limit further insight into the star formation process across different environments or galaxy properties.

The COLD GASS project investigated the relation between molecular gas depletion time (t_{dep}) and global galaxy parameters for a representative sample of ~ 360 galaxies with stellar masses $10^{10} - 10^{11.5} M_\odot$, at redshift $0.02 - 0.05$ (Saintonge et al. 2011a). CO(1-0) line measurements were combined with ancillary optical and FUV data from the SDSS and GALEX to explore global relations between star formation and molecular gas of nearby galaxies (Saintonge et al. 2011b). This large and unbiased sample –no selection criteria except mass– allows a statistical research on star formation law for nearby galaxies. The global star formation efficiency (SFE) or molecular gas depletion time was found to be dependent on a variety of galaxy parameters, including stellar mass, stellar surface mass density, concentration of the light (i.e. bulge-to-disk ratio), NUV– r colour and specific star formation rate. The strongest dependence was on colour and specific star formation rate. Especially, the bulge-dominated galaxies tend to have longer t_{dep} , showing that the bulge presence somehow suppresses the star formation. The results from the COLD GASS were intriguing as they suggested that there are different star formation laws among different types of galaxies.

In our work we try to minimize the differences in analysis methods between the COLD GASS and resolved HERACLES data and to investigate their discrepancies. We present our plans to approach the problems and outline the following chapters in next section.

1.4 This thesis

As discussed previously, galaxy evolution can be appreciated by three processes: (1) accretion of gas from the intergalactic medium, (2) conversion from gas into stars, and (3) return of enriched gas and energy to the intergalactic medium. All are directly linked to gas. In this work, we are particularly interested in the first and second processes. Though it is not easy to directly witness the gas being accreted into galaxies, we study the stellar populations of galaxies in a resolved way to explore how the newly-accreted gas fuel the recent star formation in episodic or busty mode. To understand the second process, we focus on the depletion timescale for the molecular gas under current star formation as the stars are born within the molecular gas clouds.

In Chapter 2, we first develop principal component analysis (PCA) techniques, by which we achieve much better signal-to-noise ratio for galaxy spectra. The main concept of the PCA method is that a galaxy spectrum can be decomposed into a set of orthogonal principal components (PCs), which can be linked to the physical properties of galaxies, such as the fraction of stars formed over the last billion year. By decomposing each observed spectrum into the same set of PCs, and by comparing the amplitudes of the

components with those calculated for models, the likelihood distribution of each physical parameter can be calculated and thus constrained. Next we create a library of model spectra by using a population synthesis code, and superimposing additional bursts of star formation on to continuous star formation histories (SFHs). With these novel techniques, we constrained the radial dependence of the recent SFHs of ~ 200 local galaxies with the long-slit spectroscopy data by fitting stellar population models to several observational parameters that jointly place strong constraints on whether the galaxy has been forming stars smoothly or episodically over the past 1-2 Gyr.

Next, we turn to study the star formation process inside the galaxy in terms of molecular gas depletion time in Chapter 3. We explored whether the depletion time correlates with the galaxy properties using the data from COLD GASS survey, which has observed ~ 360 massive galaxies with a wide range of galaxy properties using the IRAM 30-meter telescope for CO(1-0) line measurements. We improved on previous work by estimating SFR more accurately using the combination of far-ultraviolet and mid-infrared data, and by deriving depletion time within a fixed aperture set by the CO gas observation. What we want to ascertain is how fast the gas fuel is consumed into stars. To answer this question as accurately as possible, it is clearly preferable that the apertures for the molecular gas and SFR measurements should be closely matched.

In Chapter 4, we further study the impact of galaxy internal structures such as the bulge, arm, bar and ring on the variation of molecular gas depletion time, by combining 3 data sets of nearby galaxies on different spatial scales, from 1kpc to disk-averaged scale. We have identified two important parameters that are correlated with the depletion time. With the combination of these two parameters, we are able to better constrain the molecular gas depletion time of nearby galaxies than previous works.

Finally, we conclude our work and provide our outlook on future studies in Chapter 5.

Chapter 2

Spatially-resolved star formation histories of nearby galaxies

Based on

Mei-Ling Huang et al.

MNRAS, 431, 2633, (2013)

2.1 Introduction

As aforementioned in Chapter 1, it is now well-established that galaxies in the nearby Universe separate rather cleanly into two classes: those with disk morphologies, plentiful gas and ongoing star formation and those that are bulge-dominated, with little gas and star formation, and where star formation has largely ceased. Most of the baryons in the Universe are not locked up in stars, but reside in the circum-galactic medium associated with virialized dark matter halos or in a more diffuse phase in the intergalactic medium. It is thus reasonable to postulate that the observed bimodality in galaxy properties is in some way linked with the ability of galaxies to accrete gas from the external environment.

It is very difficult to probe gas infall onto galaxies directly. Resolved studies of the stellar populations of galaxies may, however, provide some important clues as to how accretion may refuel galaxies. Bell & de Jong (2000) used a large sample of low inclination spiral galaxies with radially resolved B,R,K photometry to derive estimates of age and metallicity as a function of position within the galaxy. Bell & Bower (2000) then interpreted these results using very simple models of disk galaxy evolution. They showed that a “closed box” model in which the star formation history and the metallicity of a given area in

any galaxy depend only on the initial local gas surface density did not provide a good fit to the observational results. Real galaxies had stronger age gradients than predicted, and the predicted slope of the age/central surface brightness correlation was steeper than observed. Models which included infall of gas (with an infall rate that was larger for low mass galaxies) were required to fit the age/surface brightness relations. Outflows were required to explain the observed correlation between stellar metallicity and galaxy mass.

Muñoz-Mateos et al. (2007) examined the specific star formation rate profiles of a sample of nearby, face-on spiral galaxies with UV photometry from the GALEX Atlas of Nearby Galaxies and K-band photometry from the Two Micron All Sky Survey. They showed that on average, galaxies were forming stars at higher relative rates in their outer regions compared to their inner regions. More recently, Wang et al. (2011) showed that UV/optical colour gradients of galaxies are strongly correlated with their atomic gas content. Gas-rich galaxies with high H I gas masses had stronger colour gradients than galaxies of the same stellar mass, size, and NUV-r colour with average H I content. Both groups interpreted their results in the context of an “inside-out” picture of disk galaxy formation, which has commonly served as a basis for semi-analytic models of the formation of discs in the context of cold dark matter cosmologies.

The UV/optical colours of galaxies depend strongly on the amount of dust extinction in the galaxy and also are sensitive to star formation occurring over timescales of \sim 1 Gyr. They thus cannot be used to assess whether the recent star formation history of a galaxy has been smooth or episodic. Combinations of narrow-band stellar absorption line indices, in particular the 4000 Å break strength and the equivalent widths of Balmer absorption lines , such as H γ_A or H δ_A , are able to probe the recent star formation histories of galaxies in more detail. Galaxies that have undergone a burst of star formation in the last 1-2 Gyr will have stronger Balmer absorption line equivalent widths for a given value of 4000 Å break strength, compared to galaxies that have been forming their stars continuously (Dressler & Gunn 1983; Poggianti et al. 1999; Kauffmann et al. 2003a).

In our work, we aim to constrain the radial dependence of the recent star formation histories of disk galaxies. We compare spectral indices, the 4000Å break strength (D_n4000), a Balmer line index derived using an approach based on principal component analysis (PCA), and the present-day star formation rate over stellar mass (specific star formation rate ; SSFR) to a library of models generated from the Bruzual & Charlot (2003) population synthesis code. We use the best fit models to constrain the timescale over which stars have been formed at different radii in the disk. We show that the star formation histories of many spiral galaxies cannot be described by simple exponentially declining star formation histories. Additional recent (< 2 Gyr old) episodes of star formation are required in order

to fit D_n4000 , $H\gamma_A$ and SSFR simultaneously. The mean fraction of stars formed in these recent episodes is similar in the inner and outer regions of galaxies, except for massive galaxies, where the bursts occur predominantly in the outskirts of the galaxy.

We also study how the recent star formation histories and gas-phase metallicities in the inner and outer regions of the galaxies in our sample correlate with their atomic and molecular gas content. Our main result is that the recent star formation history and the metallicity in both the inner and outer regions of galaxies are strongly correlated with their total atomic gas mass fraction. In contrast, only the inner star formation history and metallicity are correlated with total molecular gas fraction.

This chapter is organized as follows. Section 2.2 introduces the 21cm and CO(1-0) line data we use from GALEX Areceibo SDSS (GASS; Catinella et al. 2010) and COLD GASS (Saintonge et al. 2011) surveys and the long-slit spectroscopic observations from the MMT follow-up observations (Moran et al. 2012). We explain how we create a library of model spectra and use it to extract estimates of parameters such as burst mass fraction in Section 2.3. Based on the results of the fits, we classify our sample galaxies into five groups according whether their star formation histories are best described by continuous or burst models in their inner and outer regions. In Section 2.4, we examine how the fraction of galaxies in these different classes depends on their location in the plane of stellar mass versus stellar surface density/concentration/colour. We also examine how the fraction of stars formed both continuously and in bursts in the inner and outer regions of the galaxy depends on the location of galaxies in these planes. We summarize and discuss our results in Section 2.5.

2.2 Data

The data set on which this analysis is based has been described in detail in (Moran et al. 2012). The original parent sample consists of galaxies with HI line flux data from the Arecibo telescope that were observed as part of the GASS survey (Catinella et al. 2010; 2012). GASS aimed to measure the neutral hydrogen content for a large, uniform sample of ~ 1000 massive galaxies with stellar masses in the range $10^{10} - 10^{11.5} M_\odot$ and redshifts in the range $0.025 < z < 0.05$. No other selection criteria such as cuts on morphology, colour or gas content were applied. This sample thus provided an unbiased view of how the cold gas fraction related to the physical parameters of galaxies. The reader is referred to these papers for details about the sample selection and the HI observations. A subset of 300 galaxies were selected from this sample for CO ($J = 1 - 0$) observations using the IRAM 30m telescope (Saintonge et al. 2011). Of these, around 200 galaxies now have

reduced long-slit spectroscopy obtained from both the Blue Channel Spectrograph on the 6.5m MMT telescope on Mt. Hopkins, AZ, and the Dual Imaging Spectrograph on the 3.5m telescope at Apache Point Observatory (APO; see Moran et al. 2010 for details about the observational setup and data reduction). These galaxies were all selected at random from the GASS sample.

The wavelength ranges for MMT and APO observations are \sim 3900-7000 Å at a spectral resolution of \sim 4 Å (90 km s^{-1}), and \sim 3800-9000 Å at a spectral resolution of \sim 6-8 Å (150 km s^{-1}). The spectra were spatially binned outward from the galaxy center to ensure an adequate S/N in each spatial bin. All bins have minimum extent equal to the slit width: 1.25 arcsec for the MMT observations) and 1.5 arcsec for the APO observations. The bin size is typically <3 arcsec, corresponding to a physical size of \sim 1.5-3 kpc at the redshift of the galaxies in our sample. The S/N per bin is required to be larger than 15 (per Å) in the inner regions of the galaxy. In the outer, lower surface brightness regions, these requirements are progressively loosened in order to compromise between S/N and spatial resolution: we adopt S/N >10 for bins out to a distance of 4.5'', S/N >8 for bins between 4.5 and 6'' and finally S/N >6 in the outermost bins. The spectra were flux-calibrated by matching to SDSS *g* and *r*-band photometry measured through an aperture matched to the slit. The O3N2 index (Pettini & Pagel 2004) was applied to estimate gas-phase metallicities. The empirical relation is $12 + \log(\text{O/H}) = 8.73 - 0.32 \text{ O3N2}$, where O3N2 = $\log(([{\text{OIII}}]/\text{H}\beta)/([{\text{NII}}]/\text{H}\alpha))$. It was demonstrated that the inferred metallicity gradient did not depend on the exact choice of indicator.

All galaxies have NUV and FUV fluxes from the GALEX medium imaging survey. SDSS *r*-band and GALEX NUV images were used to derive the NUV-*r* colours of the galaxies in our sample. The SDSS images were first degraded to the resolution of NUV images. The *r*-band and NUV magnitudes within Kron elliptical apertures were obtained using SExtractor (Bertin & Arnouts 1996) and corrected for Galactic extinction following Wyder et al. (2007). The reader is referred to Catinella et al. (2010) for a more detailed explanation. Global galaxy parameters such as stellar mass, stellar surface mass density, and concentration index were taken from the MPA/JHU value-added catalogs (<http://www.mpa-garching.mpg.de/SDSS>). Stellar masses were derived by fitting SDSS photometry to stellar population synthesis models. Stellar surface mass density was defined as $M_*/(2\pi R_{50,z}^2)$, where $R_{50,z}$ was the radius containing 50% of the Petrosian flux in *z*-band. Concentration index was defined as R_{90}/R_{50} where R_{90} and R_{50} are the radii enclosing 90% and 50% of the total *r*-band light.

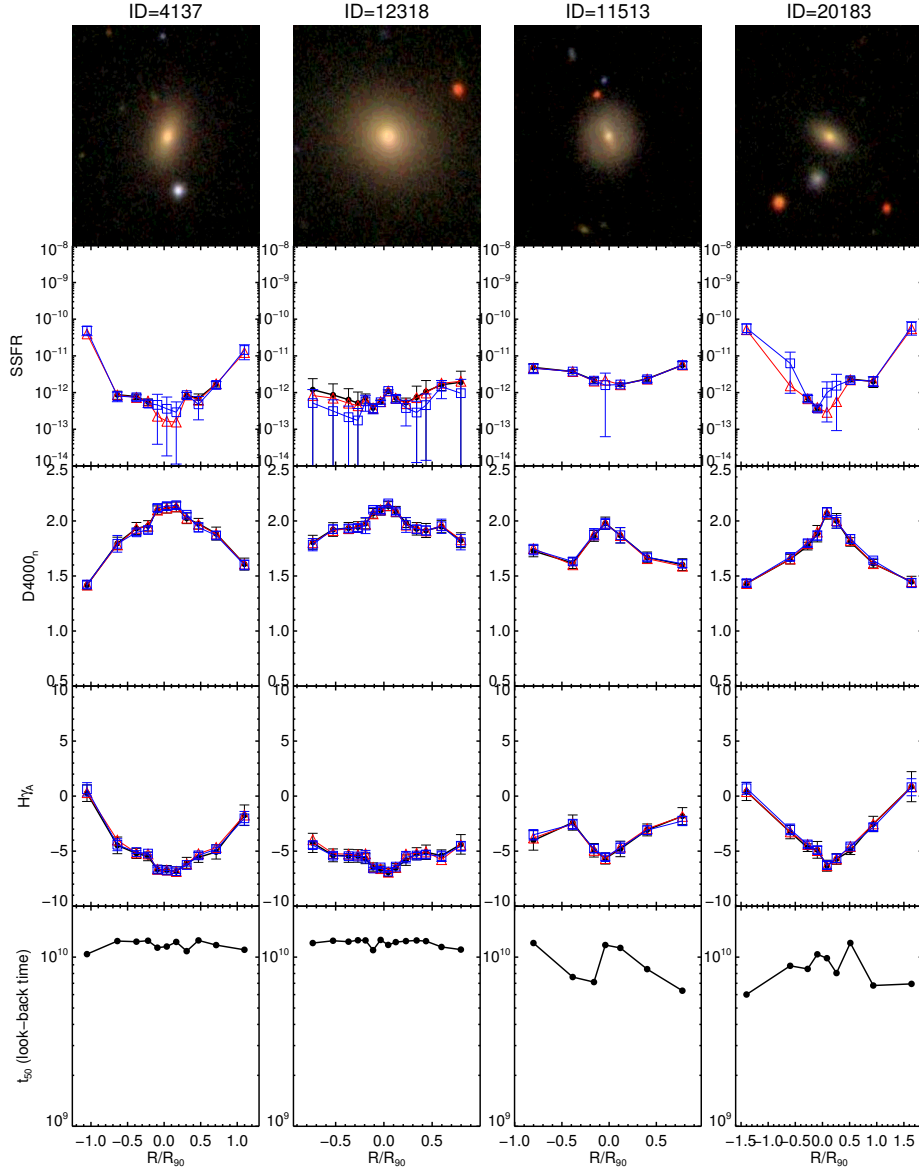


Figure 2.1: Model fits for galaxies with star formation histories of type A (columns 1 and 2) and type B (columns 3 and 4). The first row shows SDSS cut-out images of the galaxy. Rows 2,3, and 4 show the radial run of the specific star formation rate, the 4000 Å break index and the $H\gamma_A$ index. Black points show the data along with error bars. Red/blue lines are the model fits using minimum chi-square model and the median of the PDF, respectively. In the bottom row we plot the look-back time when half of stellar mass was formed. Note that radii are scaled by dividing by R_{90} , the radius enclosing 90% of the r -band light.

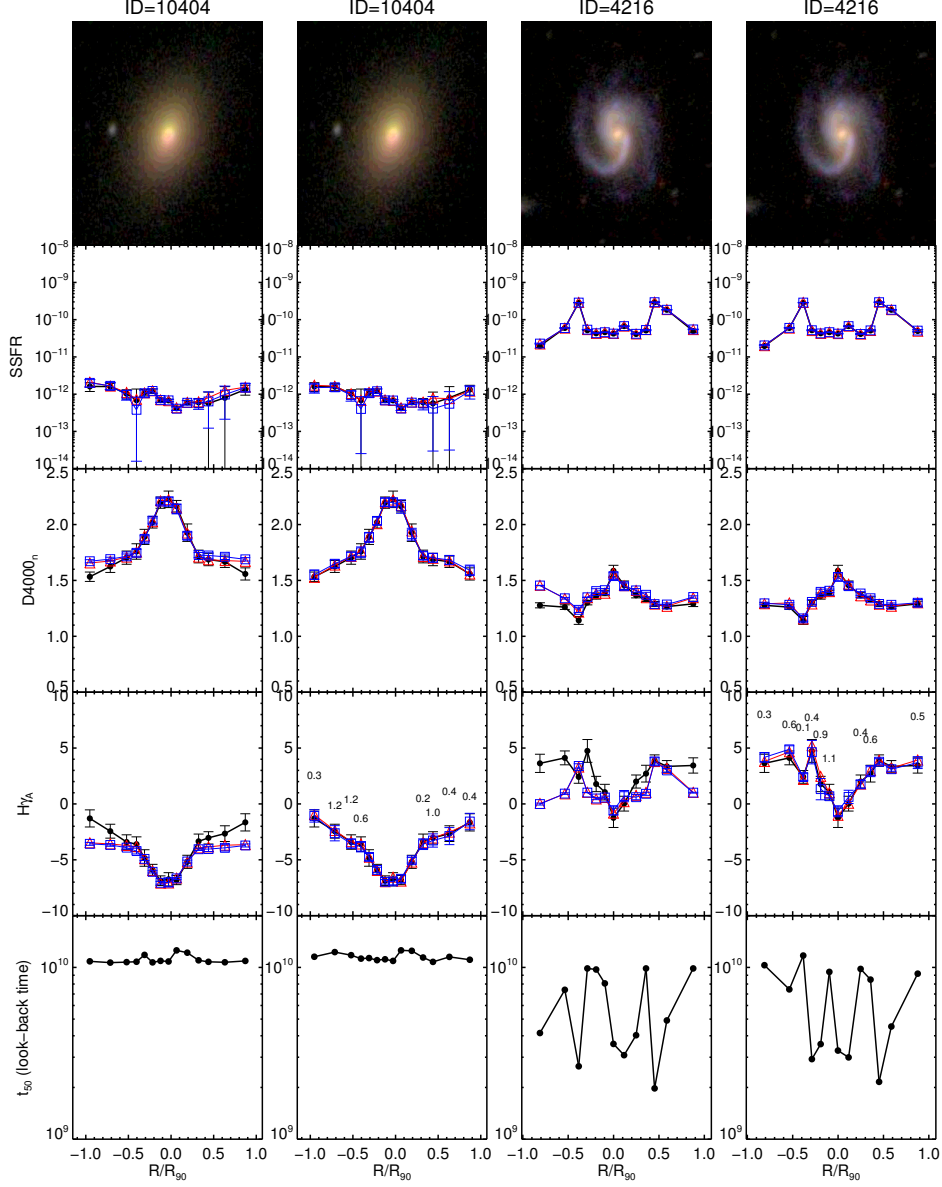


Figure 2.2: Examples of a galaxy of Type C (Columns 1-2) and Type D (Columns 3-4). The rows and line styles have the same meaning as in Figure 2.1. Columns 1 and 3 show the best-fit continuous models. Columns 2 and 4 show the best-fit models that include bursts. The number above the bins in the fourth row is the look-back time of the start of bursts in units of Gyr.

2.3 Analyses

2.3.1 A PCA-based Balmer absorption line index

The use of “classic” Balmer absorption line Lick indices such as $H\delta_A$ or $H\gamma_A$ measured directly from the galaxy spectra can be problematic for two reasons: 1) Because these indices are defined over a narrow range in wavelength, the signal-to-noise of the measurements is quite low, especially towards the outer regions of the galaxy, where the spectra may only have $S/N \sim 2$ per pixel. 2) In star-forming galaxies, the Balmer absorption lines are filled in by emission. A robust measurement of the absorption line equivalent width hinges on subtracting this emission accurately.

If stellar population models fit the observed spectra accurately, they provide one way of solving the problem. Because the models are fit to the spectra over a wide range in wavelength, the errors on Balmer line indices derived from these fits decrease with respect to those for directly measured indices (Wild et al. 2007). In addition, the wavelength regions where emission may be present are masked when the fitting is carried out.

In our work, we apply the principal component analysis (PCA) method described in Chen et al. (2012), which is an extension of the method described in Wild et al. (2007). The principle of PCA method is that a galaxy spectrum can be decomposed into a set of orthogonal principal components (PCs), which can be linked to physical properties such as fraction of stars formed over the last Gyr, or to estimates of indices such as D4000, $H\delta_A$, $H\gamma_A$ using a library of star formation histories generated using population synthesis models. By comparing the amplitudes of the principal components of the observed spectra to those of the modelled spectra, the likelihood distribution of such parameters can be calculated and thus constrained. The advantage of this approach is that it improves our estimates of Balmer absorption line equivalent widths, particularly for the spectral bins with poor S/N in the outskirts of the galaxies. The reader is referred to Chen et al. (2012) for further details. In this work, we find the linear combination of PC amplitudes that best represents the indices D4000 and $H\gamma_A$ for each spectrum. A probability distribution function (PDF) for either D4000 or $H\gamma_A$ can be built using χ^2 as weights. We use the median value of the PDF as our nominal estimate of the parameters, and the 16th to 84th percentile range of the PDF as the $\pm 1\sigma$ confidence interval.

2.3.2 Comparison with a library of SEDs of model galaxies

We compare two PCA-derived spectral indices, which we will denote $\text{PCA}_{D_n(4000)}$ and $\text{PCA}_{H\gamma_A}$, as well as the present-day star formation rate over stellar mass (sSFR) derived

from the extinction-corrected H α flux as described in Moran et al. (2012), to a library of models generated from the Bruzual & Charlot (2003) population synthesis code. As we will demonstrate, these three quantities jointly place strong constraints on whether the galaxy has been forming stars smoothly or episodically over the past 1-2 Gyr.

We create a library of models by using the population synthesis code of Bruzual & Charlot (2003). The underlying model has a continuous SFR, declining exponentially with time $SFR(t) \propto \exp(-\gamma t)$, with γ uniformly distributed between 0 (i.e. constant star formation rate) and 1 Gyr⁻¹. Stars begin to form at a look-back times between 13 Gyr and 1.5 Gyr.

We then superimpose additional bursts of star formations onto these continuous models.

¹ The strength of the burst is defined as the fraction of the stellar mass produced by bursts relative to the total mass formed by continuous models, and is distributed logarithmically between 0.001 and 4. Bursts are described by top-hat functions and have durations between 3×10^7 to 3×10^8 years. The combination of Balmer absorption lines and 4000 Å break strength is not sensitive to star formation episodes that have occurred longer than about 2 Gyr ago, so the bursts occur randomly between look-back times of 2 Gyr and the present. The metallicity range of our models is distributed uniformly from 0.005 to $2.5 Z_\odot$. Each model includes dust extinction based on the two-component model of Charlot & Fall (2000), where the V-band optical depth τ_v follows a Gaussian distribution with a peak at 1.78 and a width of $\sigma = 0.55$. The τ_v distribution is truncated so that it only spans the range 0-4. μ is the fraction of that optical depth affecting stellar populations older than 10 Myr and is uniformly distributed between 0 and 1.

2.3.3 Fitting procedure

We first discard those spectral bins with contamination from background or foreground sources (3 spectral bins in total, originating from 2 galaxies). We also exclude the spectral bins with large errors in the PCA indices — $PCA_{H\gamma_A} > 1$ and $PCA_{D_n(4000)} > 0.2$. This leaves a total of 2725 spectral bins out of the original 2812 bins. We first check whether the 2 PCA indices and the SSFR can be fit using the library of continuous SF models. The bins where such fits fail are then fit with the full library of continuous and burst models. We have used both the best-fit model with minimum chi-square to estimate quantities

¹It is true that exponentially decaying star formation histories are not very physical. However, as we will show, the look-back times when half the stellar mass was formed is never less than ~ 4 Gyr. As a result, an exponential model and other parametrizations such as a delayed exponential model will yield the same answers regarding burst requirements, because the timescale over which the $H\gamma_A$ index becomes strong following a burst is ~ 1.5 Gyr.

such as the stellar mass formed in the past 2 Gyr, as well as the median of the probability distribution function. In practice, the two estimates yield virtually identical results (see Figures 2.1 and 2.2). We record the stellar mass produced in the last 2 Gyrs. When the continuous models do not provide acceptable fits within 1σ error of data, we also record the stellar mass produced in the burst mode during this time period.

2.3.4 Separating inner and outer regions of galaxies

In the following sections, we will often refer to the mass of recently formed stars in both the “inner” and the “outer” regions of the galaxy. We choose $0.7R_{90}$ as the nominal radius to partition our galaxies into inner versus outer spectral bins, where R_{90} is the radius enclosing 90 percent of the r -band Petrosian flux. In Moran et al. (2012), they found that there was a clear anti-correlation between the outer-disk metallicity ($R > 0.7R_{90}$) and the total galaxy HI fraction. We therefore follow their definitions of the inner and outer regions of galaxies. We weight each spectral bin by the stellar mass enclosed by the circular annulus formed by the inner and outer boundaries of the bin. We then calculate weighted averages of quantities such as the fraction of recently-formed stellar mass and gas-phase metallicity.

2.3.5 Categorization of Galaxies According to Their Star Formation Histories

We divide our galaxy sample into five classes according to their star formation histories in their inner and outer regions:

(1) Type A: Those that are well described by continuous models at all radii, i.e. the star formation histories are well described by a varying exponential decline time as a function of radius. Type A galaxies have t_{start} ranging between 13 and 12 Gyr in look-back time.

(2) Type B: Those that are well described by continuous models at all radii, but with t_{start} varying between 12 and 2 Gyr.

(3) Type C: Those that are well described by continuous models with t_{start} varying between 13 and 2 Gyr in their inner regions, but which require a burst in their outer regions.

(4) Type D: Those that require bursts in both their inner and their outer regions.

(5) Type E: Those that require bursts only in their inner regions.

The number of galaxies of type A, B, C, D, and E is 45, 24, 34, 104, 2 respectively. Some examples of each type are presented in Figures 2.1 and 2.2. Figure 2.1 shows examples of galaxies of types A and B, which are well fit by pure exponential models. In the first

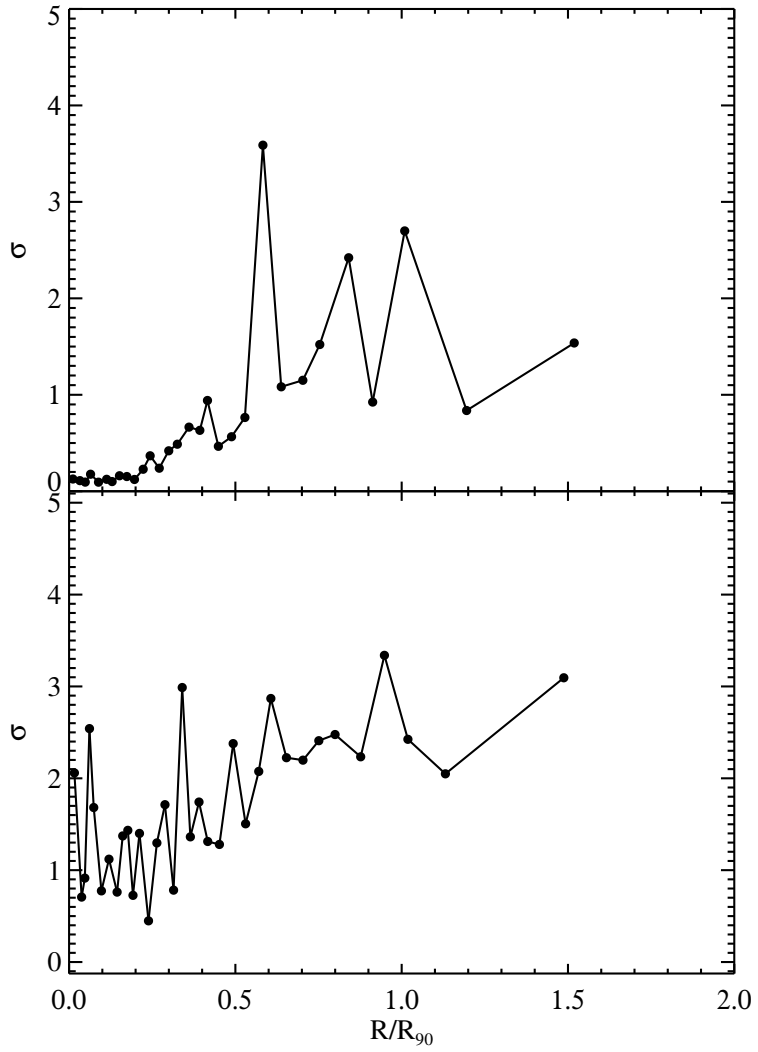


Figure 2.3: The average deviation of the observed values of $D_n(4000)$, $H\gamma_A$ and sSFR from the values predicted by the best-fit continuous models for all Type C (upper panel) and Type D (lower panel) galaxies as a function of radius. Note that the deviations are scaled by the measurement errors σ and are plotted in units of σ . This takes into account the fact that the S/N of the binned data is higher in the inner regions than the outer regions.

row, we show SDSS cut-out images. The 2nd, 3rd, 4th rows show SSFR, D4000 and $H\gamma_A$ as a function of radius in the galaxy. Note that the radii have been scaled by dividing by R_{90} . In these panels, black points show the data along with the errors. Red/blue lines are model fits using the minimum chi-square models and the median of the PDF, respectively. In the 5th row, we plot the parameters of the minimum chi-square models as a function of radius. The 5th row shows the look-back time when half of stellar mass was formed at each radius.

Figure 2.2 shows examples of galaxies of types C and D, which require bursts. The rows are the same as in the previous figure. In the left column, we show the best-fit continuous models. As can be seen, in both cases such models generally work better near the centers of galaxies. In the outer regions, the deviations in the fit to $PCA_{H\gamma_A}$ and $PCA_{D_n(4000)}$ become large. The right panels show how addition of a burst bring the models into much better agreement with the data. We note that the physical size of each bin for our sample is at least $\sim 1.5\text{-}3\text{kpc}$, and the discrepancies between the data and the continuous models often span more than 2 bins. This means that the bursts are not generated by individual HII regions, but span a significant portion of the outer disk.

In Figure 2.3 we plot the *average* deviation of the continuous models from the observations as a function of radius for type C (upper panel) and type D (lower panel) galaxies. In order to account for the fact that the observational errors increase as function of radius, we scale the deviation by σ before taking the average . As expected, the centers of Type C galaxies are well fit, with the average deviation increasing towards the outer regions. The lower panel of Figure 2.3 shows that the same general trend is also true for type D galaxies. In the central regions, the average deviation from a continuous model is only $\sim 1\sigma$, but in the outer regions the average deviation increases by a factor of 2–3. As we will show in the next section, the main difference between galaxies with type C and type D star formation histories is stellar mass. Galaxies with recent star formation only in their outer regions are predominantly systems with stellar masses greater than $\sim 10^{11} M_\odot$.

2.4 Results

2.4.1 Dependence of star formation history on stellar mass, surface density, concentration and colour

In this section, we investigate how the fraction of galaxies with different types of star formation histories defined in Section 2.3.5 depends on stellar mass, galaxy colour and structural parameters such as surface density and concentration.

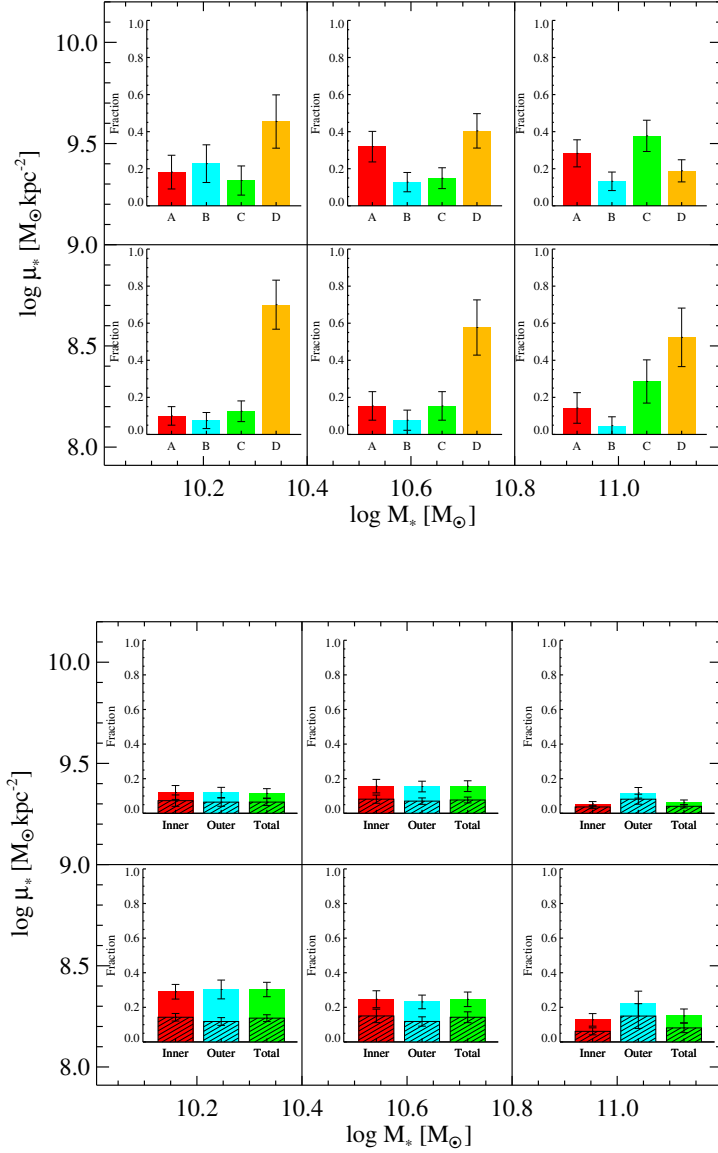


Figure 2.4: Top: Fraction of galaxies with different types of star formation history in the two-dimensional plane of stellar surface density versus stellar mass. Poisson error bars are shown. Bottom: Fraction of the stellar mass formed in the last 2 Gyr in the inner region ($R < 0.7R_{90}$, red), outer region ($R > 0.7R_{90}$, cyan), and in the whole galaxy (green). The hatched area shows the fraction of stellar mass formed in the last 2 Gyr in the *burst mode*. Error bars have been computed using boot-strap resampling.

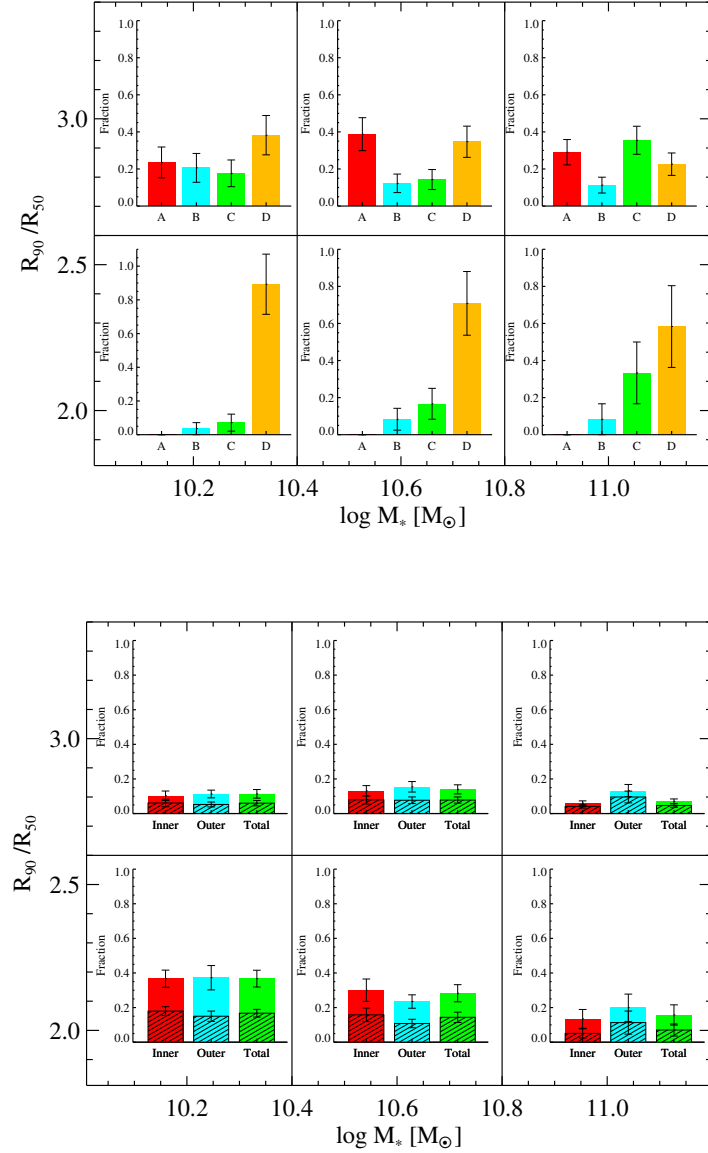


Figure 2.5: As in Figure 2.4, except for galaxies in the two dimensional plane of concentration versus stellar mass.

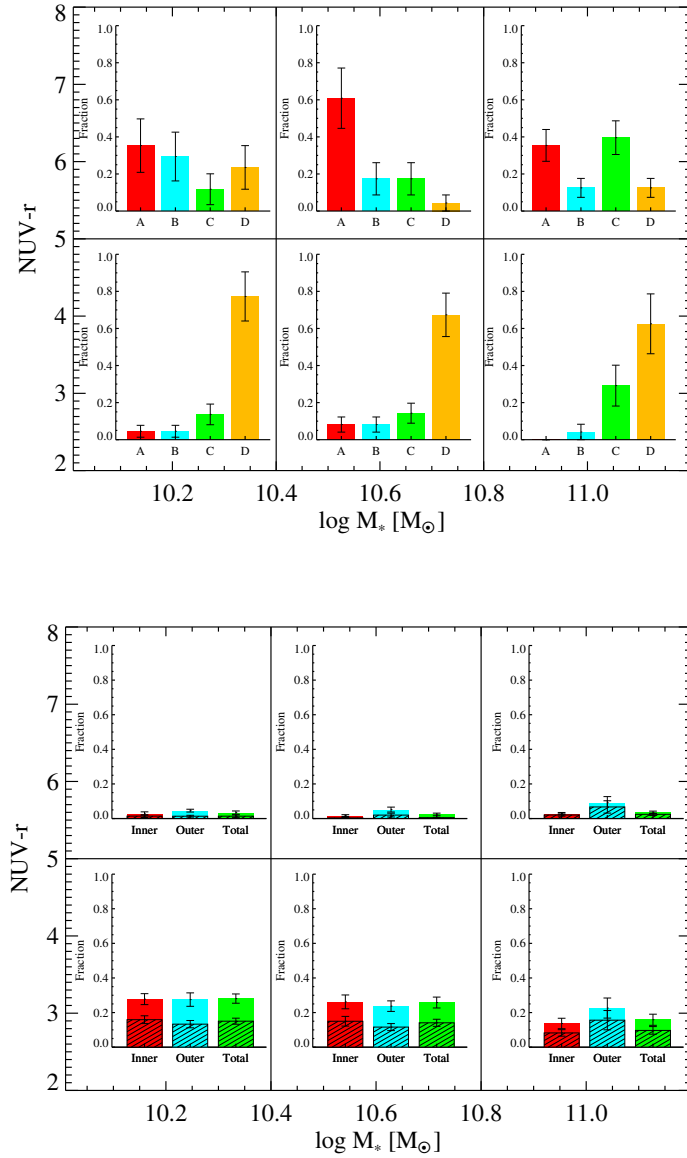


Figure 2.6: As in Figure 2.4, except for galaxies in the two dimensional plane of NUV- r colour versus stellar mass.

For central galaxies, stellar mass is a good tracer of the mass of dark matter halo in which the galaxy resides. The surface density of the galaxy is a rough measure of the degree to which the gas has lost angular momentum prior to being converted into stars. The concentration index is a good proxy for the bulge-to-disk or bulge-to-total luminosity ratio of the galaxy (see Fig. 1 of Weinmann et al. 2009). Finally, in the absence of dust, the global NUV-r colour is a measure of the average luminosity-weighted age of the stellar population. In order to understand whether the star formation history of a galaxy is determined primarily by its mass or by its structural properties, we will analyze SFH trends in *two dimensional planes* of stellar mass versus surface density and concentration. We will also examine how the fraction of stars formed both continuously and in bursts in the inner and outer regions of the galaxy depends on the location of the galaxies in these 2D planes.

The plane of stellar mass versus stellar surface density

All galaxies are divided into 6 bins by dividing their stellar mass into 3 bins, 10.0–10.4 M_{\odot} , 10.4–10.8 M_{\odot} , and 10.8–11.2 M_{\odot} in $\log M_*$, and surface mass density into 2 bins: $\log \mu_* < 9 M_{\odot} \text{ kpc}^{-2}$ and $\log \mu_* > 9 M_{\odot} \text{ kpc}^{-2}$. In each bin, we calculate (1) the fraction of galaxies with different types of star formation histories (top panel), (2) the fraction of the stellar mass formed within the last 2 Gyr in the inner region, the outer region and in the entire galaxies (bottom panel), (3) the fraction of the stellar mass formed in the *burst mode* in the last 2 Gyr in the inner region, the outer region, and in the entire galaxy (hashed histograms in the bottom panel).

As shown in the top panel of Fig. 2.4, the star formation histories of galaxies clearly depend on both stellar mass and surface density. The fraction of quiescent galaxies without bursts (types A and B) depends mainly on surface density rather than stellar mass. There is some tendency for quiescent galaxies to be somewhat more active (i.e. be of type B) if they have low masses.

The fraction of galaxies that have experienced recent bursts in both their inner and their outer regions (type D) decreases both as a function of stellar mass and stellar surface density. In the stellar mass bin with $\log M_*$ in the range 10–10.4, type Ds make up more than two thirds of the entire population, but type Ds make up only a small fraction of the galaxies our highest M_*/μ_* bin. Interestingly, however, the fraction of galaxies that have experienced recent bursts in their outer regions only (type Cs) exhibits the opposite dependence of on the mass of the galaxy. In the highest stellar mass bin with $\log M_*$ in the range 10.8–11.2, there are as many type C galaxies as there are quiescent (type A and B) galaxies.

The bottom panel of Fig. 2.4 displays the fraction of stars formed in the last 2 Gyr as a function of location in the plane of stellar mass and stellar surface density. We show the fraction of recently formed stars in the whole galaxy (in green) as well as the fraction in the inner ($R < 0.7R_{90}$, red) and outer ($R > 0.7R_{90}$, blue) regions. The fraction of stars formed in the last 2 Gyr in the *burst mode* is indicated as hashed shading. As expected, the fraction of recently formed stars is highest for galaxies with low masses and low surface densities and lowest for galaxies with high masses and high surface densities. Interestingly, the recent star formation is always rather evenly split between the inner and outer parts of galaxies, except for the most massive galaxies with low stellar surface densities, where more star formation occurs in the galaxy outskirts. These results are consistent with a recent analysis by Pérez et al. (2013) of star formation in the inner and outer regions of galaxies using a sample of ~ 100 galaxies with integral field unit (IFU) spectroscopy. What is new here, is that we can estimate the fraction of the recent star formation that occurred in bursts. We see that the burst fraction is highest in massive galaxies. The majority of galaxies with stellar masses in the range 10–10.4 in $\log M_*$ require bursts in both their inner and in their outer regions (i.e. they are classified as type D systems), but the total mass of stars formed in the bursts over the last 2 Gyr is comparable or smaller (in the case of low mass galaxies with low densities) than that formed in the quiescent mode. In high mass galaxies, the opposite is true – the majority of the recent star formation is contributed by bursts.

The plane of stellar mass versus concentration

Figure 2.5 is similar to Figure 2.4 except that we divide galaxies according to concentration index (R_{90}/R_{50}) at a value of 2.6. As can be seen, the results are quite similar to those obtained when galaxies are divided by stellar surface mass density. One notable difference is that in Figure 2.5 we see that *all* type A galaxies have the division between quiescent galaxies and galaxies with actively ongoing star formation is much more pronounced. We see that *all* type A galaxies have $R_{90}/R_{50} > 2.6$, whereas Figure 2.4 shows that there is a significant number of type A galaxies with stellar surface mass densities less than $10^9 M_\odot \text{ kpc}^{-2}$. We note that high concentration index (equivalently bulge-to-disk ratio) instead of high stellar surface density (equivalently contraction factor) appears to be the necessary condition for galaxies with quiescent type A star formation histories. Although high concentration is a necessary condition, it is not a sufficient condition – a sizeable fraction of bulge-dominated galaxies have experienced bursts of star-formation in the last 2 Gyr.

The plane of stellar mass versus colour

In Figure 2.6 we divide galaxies according to (NUV-r) colour at a value of 4.8 . As can be seen from the right-hand panel, red global colours select out the galaxy population that have experienced very little recent star formation both in their inner and in their outer regions. It is noteworthy that almost all galaxies with quiescent star formation histories (types A and B) belong to the red population with $\text{NUV-r} > 4.8$. Galaxies that have experienced bursts in their outer regions are roughly split evenly between the red and the blue populations, while type D galaxies that have experienced bursts in both their inner and outer regions are predominantly blue. We note, however, that a significant population of red type D galaxies is found in the lowest stellar mass bin.

Distribution of SFH parameters of galaxies

In the previous sub-sections we studied the fraction of galaxies with bursty versus continuous star formation histories as a function of stellar mass, colour and structural parameters. We also looked at the contribution of bursts to the recent star formation in the inner and the outer regions of galaxies, as a function of these same parameters. In this sub-section, we analyze the distribution of burst strengths in galaxies, as well as the look-back time when half the stars were formed. For simplicity, we confine our attention to the two dimensional plane of concentration versus stellar mass.

(i) *The Fraction of stars formed in bursts.* Figure 2.7 shows the distribution of the fraction of stars formed in bursts in the inner and outer regions of galaxies as a function of position within this plane . As seen in the top panel, the fractions of stars formed in bursts in the inner region is generally around a few percent for bulgy galaxies ($R_{90}/R_{50} > 2.6$) or for massive galaxies ($\log M_* > 10.8$). In the inner regions of less massive, disk-dominated galaxies the median burst strength is $\sim 10\%$ and the distribution is much wider. The bottom panel of Figure 2.7 shows that burst strengths in the outer regions of galaxies are insensitive to whether it is bulge or disk-dominated. The main controlling factor is the mass of the galaxy. In the highest stellar mass bin, the median burst strength in the outer region is $\sim 3\%$, about a factor of two lower than in the other two bins. We also note that in massive galaxies, the outer bursts are stronger than the inner bursts on average, whereas the opposite is true for low mass galaxies.

(ii) *The look-back time when half the stellar mass was formed.* In Figure 2.8, we make similar plots of the look-back time when half the stellar mass was formed (T_{50}), which provides information about the mean stellar ages of the galaxies. The trends in this plot are much weaker. Only a very small fraction of galaxies have T_{50} less than $\sim 4 \times 10^9$ Gyr in either their inner or their outer regions. This is in keeping with the results in the previous

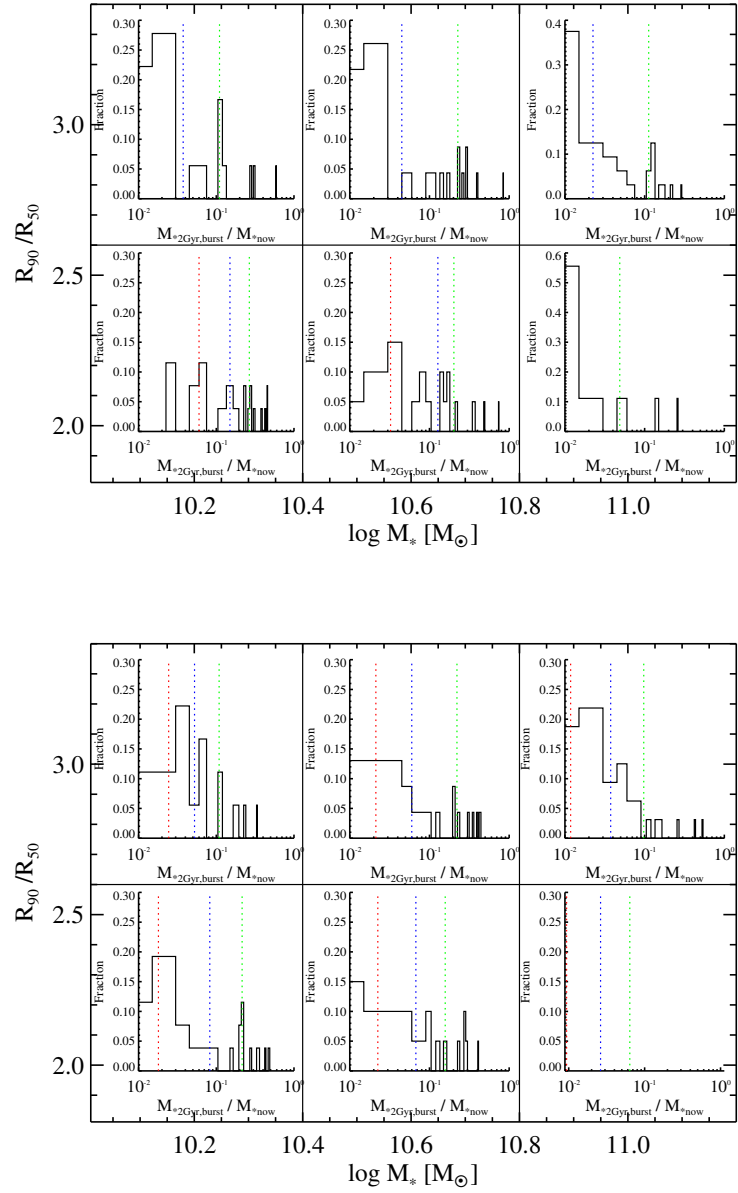


Figure 2.7: Top: Distribution of the fraction of stars formed in bursts in the inner regions of galaxies in the two-dimensional plane of concentration versus stellar mass. Bottom: As in the top panel, but in the outer region. The red, blue, green dotted lines indicate 25%, median, 75% values of the distribution in each panel.

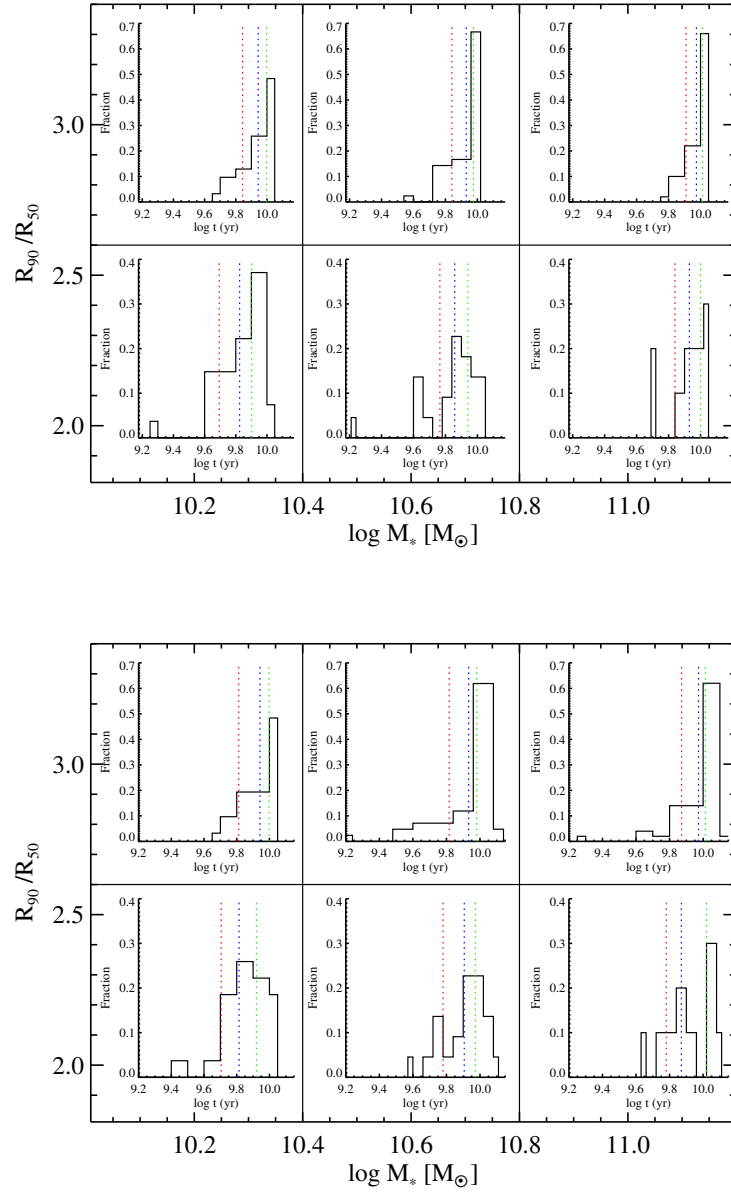


Figure 2.8: Top: Distribution of the look-back time when half the stellar mass was formed in the inner regions of galaxies in the two-dimensional plane of concentration versus stellar mass. Bottom: As in the top panel, but in the outer region. The red, blue, green dotted lines indicate 25%, median, 75% values of the distribution in each panel.

section, which shows that although recent bursts are required to fit the spectral parameters, the fraction of mass formed in these bursts generally does not exceed $\sim 10 - 20\%$ of the total stellar mass. Disk-dominated galaxies generally have younger mean stellar ages than bulge-dominated galaxies of the same stellar mass, and the most massive galaxies have the oldest mean stellar ages. The trend for the most massive, bulge-dominated galaxies to have the oldest mean stellar ages holds in both the inner and outer regions of the galaxies, but is somewhat stronger in the outer region.

We also note that outer star formation in massive galaxies discussed in the previous section, is manifested in this plot as shift in the lower 25th percentile of the mean age distribution, rather than a shift in the median value. This means that outer disk growth is a phenomenon that pertains to a *minority of the massive galaxies*, rather than to the population in general.

2.4.2 Relations between star formation history, HI/H₂ mass fraction and gas-phase metallicity

In the previous section, we explored how the star formation histories in the inner and outer regions of galaxies depend on their stellar mass, structural properties and colour. In this section, we examine how star formation history depends on the gas content and gas-phase metallicity of a galaxy. In previous work, Moran et al. (2012) showed that around 10% of all galaxies with stellar masses greater than $\log M_* > 10$ exhibit strong drops in gas-phase metallicity in their outer regions. These galaxies tended to have high HI content and to have actively star-forming outer disks.

In this analysis, we explore the correlations between the fraction of recently-formed stars and gas-phase metallicity in the inner and outer regions of the galaxy with both the HI and H₂ gas mass fraction. We also explore how the correlations change as we vary the radius R_{cut} used to divide the inner galaxy from the outer galaxy.

The spectral bins with only upper or lower limits on metallicity are discarded before we carry out our analysis. For each value of R_{cut} (in units of R_{90}), we compute correlation coefficients of Spearman rank tests for

- The relations between the fraction of stars formed in the inner/outer regions of the galaxy and total HI gas mass fraction.
- The relations between the fraction of stars formed in the inner/outer regions of the galaxy and total H₂ gas mass fraction.

We only take into account the correlation coefficients with probability larger than 0.97. For the coefficients with probability smaller than 0.97, we set the coefficients to zero. (In

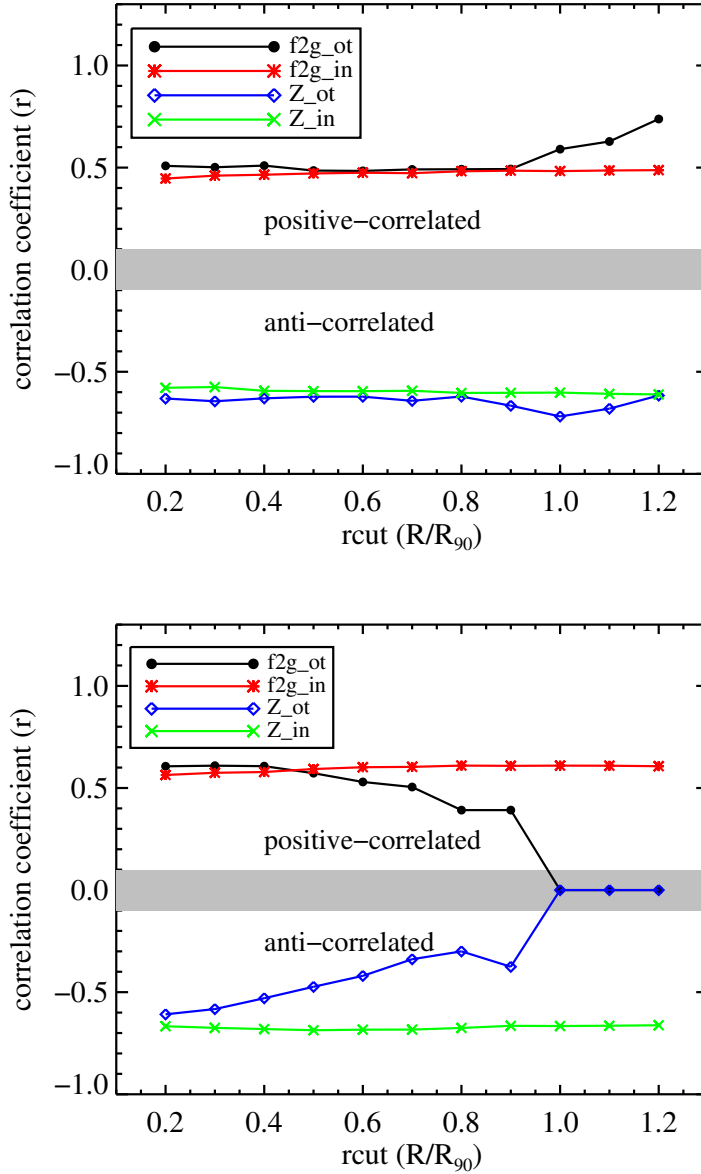


Figure 2.9: Top: The correlation coefficients of Spearman rank tests for the fraction of recently-formed stellar mass and gas-phase metallicity as a function of HI mass fraction. The four parameters, $f2g_{in}$, $f2g_{ot}$, Z_{in} , Z_{ot} , are M_{*2Gyr}/M_{now} for the inner region, M_{*2Gyr}/M_{now} for the outer region, inner metallicity, and outer metallicity. The correlation coefficients are plotted as a function of R_{cut} , the radius (in units of R_{90}) used to separate the inner region of the galaxy from the outer region. Bottom: As in the top panel, but for the four parameters as a function of H₂ mass fraction.

practice, this only happens for the relations between outer star formation and metallicity and H₂ gas mass fraction when R_{cut} is greater than R₉₀.)

Figure 2.9 summarizes the results of this exercise. r_{cut} is in units of R/R₉₀. The upper and lower panels show the results for the correlations with HI and H₂ gas mass fraction, respectively. Coefficients with values larger and smaller than zero indicate positive and anti-correlations between the parameters.

As can be seen in the upper panel of the figure, the fraction of recently-formed stars and the gas-phase metallicity in both the inner and the outer regions of the galaxy correlate strongly with the global atomic gas mass fraction. The strength of the correlations does not depend on the adopted value of R_{cut}, until R_{cut} reaches values greater than 0.9 R₉₀. At this point, stronger correlations between the gas-phase metallicity and the fraction of stars formed in the outer regions and the total HI content are seen. Interestingly, the correlation between the fraction of stars formed in the inner region of the galaxy and total HI gas fraction is independent of the value of R_{cut}. Even as R_{cut} decreases to values near zero, there is still a correlation between the fraction of stars formed in the very inner regions of the galaxy and its total atomic gas content. We will discuss possible reasons for this in the next section.

In the lower panel of Figure 2.9, we see that the gas-phase metallicity and the fraction of recently-formed stars in the inner regions of the galaxy are also both correlated with H₂ mass fraction. The correlation of these inner quantities with H₂ mass fraction is stronger than the correlation with HI mass fraction (*r* values of ~ 0.6 rather than ~ 0.4). Similar to what is seen for the atomic gas, the strength of the correlations of the inner quantities with H₂ gas mass fraction are independent of R_{cut}. The outer quantities, however, are much more weakly correlated with H₂ mass fraction and for R_{cut} > 0.7, the correlations with H₂ mass fraction disappear entirely.

2.5 Summary and discussion

We now summarize our main results as follows:

- (i) By fitting stellar population models to the combination of SSFR, D4000, H γ_A , we show that the star formation histories of many disk galaxies cannot be accurately represented if the star formation rate has declined exponentially as a function of time. Many galaxies have strong Balmer absorption lines that require recent short-lived episodes of star formation in both their inner and in their outer regions.
- (ii) The fraction of galaxies that have experienced such episodes in both their inner and outer regions is highest for systems with low stellar masses, low surface densities, and low

concentrations, i.e., late-type galaxies.

(iii) Around a third of all massive ($\log M_* > 10.8$), bulge-dominated galaxies have experienced recent star formation episodes only in their *outer* regions.

(iv) For low mass, disk-dominated galaxies, the fraction of stars formed in a single burst episode is typically around 15% of the total stellar mass in the inner regions of the galaxy and around 5% in the outer regions of the galaxy. When we average over the population, we find that such bursts contribute around a half of total mass in stars formed in the last 2 Gyr.

(v) For massive galaxies ($\log M_* > 10.8$), the fraction of stars formed in bursts is only $\sim 2 - 3 \%$. Averaging over the population, however, we find that such bursts contributed nearly all the mass in stars formed in the last 2 Gyr.

(vi) The amount of recent star formation in both the inner and outer regions of a galaxy is positively-correlated with its total atomic gas content. In contrast, only the inner star formation is correlated with total molecular gas content.

(vii) Very similar results are obtained for gas-phase metallicity. Metallicity in both the inner and outer regions of galaxies are negatively correlated with global atomic gas fractions. The metallicity in the inner region of the galaxy is negatively correlated with the molecular gas mass fraction.

We hypothesize that these results can be understood if galaxies accrete atomic gas and form stars episodically. The fact that episodic component of the star formation occurs primarily in the outer regions of massive galaxies (bottom panels of Figures 2.4 and 2.5) argues that gas may be accreted at large radii. We note that the non-episodic (continuous) component of the star formation is much more evenly split between the inner and the outer regions in these systems.

In low mass galaxies, both the episodic and the continuous components of the star formation are evenly divided between the inner and outer regions of the galaxy. It is tempting to postulate that this may indicate that gas accretion occurs in a different mode in low mass systems – some theoretical models predict that gas should be accreting in the form of “cold streams” in dark matter halos with low mass, and from quasi-static atmospheres of hot gas in dark matter halos of high mass (e.g. Kereš et al. 2005; Dekel & Birnboim 2006).

However, our data does not allow us to rule out the possibility that the inner and outer bursts in galaxies may have different triggers, for example gas accretion may be the trigger in the outer regions and disk-driven instabilities in the inner regions. Indeed, at fixed stellar mass, the fact that burst strengths are larger in the interiors of disk-dominated galaxies densities (Figure 2.7, top panel), argues that disk instabilities may indeed be key

to the origin of the episodic nature of the inner star formation. The Toomre Q parameter scales inversely with disk surface density.

The idea that gas accretion at large radii is followed by instability-triggered radial inflows of gas and a burst of star formation in the central regions of the galaxy is also consistent with our result that gas-phase metallicity and the fraction of recently formed stars in the inner region of the galaxy is best correlated with its molecular gas content. Molecular gas extends to much smaller radii than the atomic gas in all disk galaxies and also exists at considerably higher surface densities (Leroy et al. 2008). Why then do metallicity and recent star formation in the inner regions of galaxies also correlate (albeit more weakly) with the total atomic gas content of the galaxy? The most reasonable explanation, in our view, is that the atomic gas represents a longer-term *reservoir* for star formation in the inner galaxy. In other words, if the galaxy has no atomic gas, there is simply no raw material to be transported inwards to be converted into molecular gas and stars at galactic centers.

Finally, we would like to note that we began this chapter with the statement “It is now well established that galaxies in the nearby Universe separate rather cleanly into two classes: those with disky morphologies, plentiful gas and ongoing star formation and those that are bulge-dominated, with little gas and star formation, and where star formation has largely ceased.” Examination of the top panel of Figure 2.4 indicates that even at high stellar masses, bulge-dominated galaxies have actually experienced a wide variety of different star formation histories. Those that are “dead” in that they have not experienced any recent star formation episodes comprise less than half of the total population. In many of the massive, bulge-dominated galaxies star formation occurs in the outer regions of the galaxy, where the light has simply not been picked up by large scale redshift surveys that employ single fibre spectrographs. The fibres typically have diameters of 2-3 arcseconds and only sample light from the inner regions of the galaxies.

The realization that many early-type galaxies do have extended star-forming disks first came from studies of early-type galaxies at ultra-violet wavelengths (e.g., Yi et al. 2005; Kauffmann et al. 2007; Fang et al. 2012), and these results are now being confirmed by IFU studies of the nearby galaxy population Pérez et al. (2013). Our study reveals that the star formation in these disks did not occur continuously over a Hubble time, but was concentrated in a recent episode or burst. In future, large-scale Integral Field Unit (IFU) surveys of galaxies (see for example Sánchez et al. 2012) will shed more light on the nature of the star formation in the far outer reaches of nearby galaxies.

Chapter 3

The Variation in Molecular Gas Depletion Time: What are the Main Parameter Dependencies?

Based on

Mei-Ling Huang et al.

MNRAS, 443, 1329 (2014)

3.1 Introduction

Numerous studies have attempted to characterize the relation between star formation rate surface density (Σ_{SFR}) and total gas surface density (Σ_{gas}), which is usually known as Kennicutt-Schmidt laws (see Equation 1.13).

Kennicutt (1998) found the power index $N \sim 1.4$ on global scales for normal and starburst galaxies using $\text{H}\alpha$ as a star formation rate (SFR) indicator and CO and HI line emission as tracers of total cold gas content. It has been demonstrated that this value of N can be explained by gravitational instability: if stars are formed constantly each free-fall time and gas scale height is assumed to be constant, N is equal to 1.5. Other studies have found values for N that vary in the range between 1 and 3. The scatter between different studies is likely due to the fact that a variety of galaxy samples and SFR tracers were used, and that the relation was evaluated over a range of different spatial scales.

Stars form directly in molecular clouds, so the molecular gas, rather than the total or atomic gas, is believed to be linked more directly to the star formation. In recent

54 3. Variation in molecular gas depletion time: main parameter dependency

studies, Bigiel et al. (2008, 2011) explored the correlation between Σ_{SFR} on sub-kpc scales estimated from FUV plus 24 μm fluxes and Σ_{H_2} derived from CO ($J=2-1$) line luminosities using a sample of 18 nearby spiral galaxies from the HERACLES project. They reported a constant star formation efficiency with depletion time ~ 2 Gyr among these spirals, independent of local conditions such as orbital timescale, midplane gas pressure and disk stability (Leroy et al. 2008). Their results appeared to suggest that star formation is likely to be a localised process linked only to the local quantity of molecular gas. However, in subsequent work, Momose et al. (2013) found a super-linear Kennicutt-Schmidt law at sub-kpc resolution with slope $N = 1.3 - 1.8$, based on CO ($J=1-0$) plus H α and 24 μm data for 10 nearby spiral galaxies. These results would argue that the star formation efficiency in disks depends on local gas surface density. Differences with the published HERACLES results were attributed to the fact that CO($J = 2-1$) was used as a tracer of molecular gas mass. If CO($J = 2-1$) is enhanced in regions with higher star formation (and hence higher excitation), CO($J = 2-1$) may not be a linear tracer of the underlying molecular gas mass.

The COLD GASS project investigated the relation between molecular gas depletion time (t_{dep}) and global galaxy parameters for a representative sample of ~ 350 galaxies with stellar masses $10^{10} - 10^{11.5}\text{M}_{\odot}$, at redshift 0.02 – 0.05 (Saintonge et al. 2011a). CO(1-0) line measurements were combined with ancillary optical and FUV data from the SDSS and the GALEX satellite to carry out a statistical analysis of global relations between star formation and molecular gas for nearby galaxies (Saintonge et al. 2011b). The global star formation efficiency (SFE) or molecular gas depletion time was found to be dependent on a variety of galaxy parameters, including stellar mass, stellar surface mass density, concentration of the light (i.e. bulge-to-disk ratio), NUV– r colour and specific star formation rate. The strongest dependences were on colour and specific star formation rate.

In subsequent work, Leroy et al. (2013) studied the global Kennicutt-Schmidt law for 30 nearby spirals using CO(2-1) line luminosities as the molecular gas tracer and H α plus 24 μm luminosities as the SFR tracer. They found that all dependences of t_{dep} on global galaxy properties vanished after applying a CO-to-H $_2$ conversion factor (α_{CO}) that depended on dust-to-gas-ratio. Saintonge et al. (2011b) tested whether there was any relation between t_{dep} and gas-phase metallicity determined from nebular emission lines in their sample and found a null result. Since dust-to-gas ratio and metallicity are well-correlated, this would argue that the explanation given in Leroy et al. (2013) for apparent variations in molecular gas depletion time, cannot be the explanation for the results presented in Saintonge et al. (2011b).

We note that the sample of galaxies studied by Leroy et al. (2013) spans a much

narrower range in specific star formation rate than the COLD GASS sample. In particular, massive, bulge-dominated galaxies with low gas fractions and low SFR/M_{*} are absent. These are the galaxies that contribute most to the observed variations on depletion time (see Figure 7 in Saintonge et al. 2011b).

One hypothesis that has not yet been explored is that different SFR tracers may be the origin of the differing conclusions of Leroy et al. (2013) and Saintonge et al. (2011b). The latter used spectral energy distribution (SED) fitting technique to derive SFR by fitting UV and optical broad-band photometry to a grid of SED models. Correction for dust extinction was not done directly, but by adopting a set of priors that linked the range of possible values of A_V in the model grid with the NUV-r colours and 4000 Å break strengths of the galaxies. These priors were calibrated using results from the GMACS (Galaxy Multiwavelength Atlas From Combined Surveys) sample (Johnson et al. 2007), for which accurate star formation rates and extinction measurements could be obtained using UV and far-IR data.

In this chapter, we re-derive SFRs for galaxies in the COLD GASS sample by combining GALEX FUV and WISE 22μm data (Wide-field Infrared Survey Explorer; Wright et al. 2010). We thus eliminate the need for statistical dust correction methods. We also improve on the Saintonge et al. (2011b) analysis by measuring molecular gas masses and SFR surface densities within apertures that are exactly matched in radius. We show that not only does this reduce the scatter in our previously derived relations between molecular gas depletion time and galaxy parameters, but also changes some of the scalings. Correlations with galaxy structural parameters such as stellar surface mass density and the concentration index of the light are considerably weakened or entirely absent. We are able to show that the only galaxy parameter that is significantly correlated with the global depletion time of the molecular gas is the ratio of young-to-old stars in the galaxy. We also utilize molecular gas and star formation maps from the HERACLES survey to demonstrate that very similar results are found on sub-kpc scales.

3.2 Data

3.2.1 COLD GASS

Molecular gas and galaxy parameters

Our data set is drawn from the COLD GASS survey catalogue (Saintonge et al. 2011a,b, 2012), which is a subsample of the GASS survey. COLD GASS contains CO ($J = 1-0$) line measurements from the IRAM 30m telescope for ∼360 nearby galaxies with stellar masses

56 3. Variation in molecular gas depletion time: main parameter dependency

in the range $10^{10} - 10^{11.5} M_{\odot}$ and redshifts in the range $0.025 < z < 0.05$. The reader is referred to Saintonge et al. (2011a) for a detailed description of the sample selection and the observations.

The COLD GASS catalogue also includes global galaxy parameters such as stellar mass, stellar surface mass density, concentration index and NUV-r colour for each targeted galaxy. The first three parameters were taken from the MPA/JHU value-added catalogs (<http://www.mpa-garching.mpg.de/SDSS>). Stellar masses were calculated by fitting SDSS 5-band optical magnitudes to stellar population synthesis model grids. Stellar surface mass density is defined as $M_*/(2\pi R_{50,z}^2)$, where $R_{50,z}$ is the radius containing 50% of the Petrosian flux in the z -band. Concentration index is defined as R_{90}/R_{50} where R_{90} and R_{50} are the radii enclosing 90% and 50% of the total r -band light. The concentration index is well-correlated with the bulge-to-total luminosity ratio of the galaxy (Gadotti 2009; Weinmann et al. 2009). The NUV-r colours of the galaxies were measured using SDSS r -band and GALEX NUV images, which were corrected for Galactic extinction following Wyder et al. (2007).

GALEX FUV and WISE 22 μ m Data

Instead of adopting the catalog SFRs derived using SED-fitting methods, we derive new SFRs using the combination of FUV emission from GALEX data and mid-infrared 22 μ m emission from WISE data. FUV emission traces recent unobscured star formation in the galaxy. The missing part of the emission from young, massive stars obscured by surrounding dust can be recovered via the measured IR emission, which originates from the dust that is heated by absorbed FUV light.

GALEX provides FUV images with effective wavelength at 1528 Å and angular resolution \sim 4.3 arcsec FWHM. We draw the FUV maps from GALEX Data Release 7 products. When several maps from different surveys are available, we select the maps with the longest exposure time. Most of our FUV images are from the Medium Imaging survey (MIS) with typical exposure time \sim 1500 seconds; 81 out of 366 galaxies only have data from the All-sky Imaging survey (AIS) with typical exposure time \sim 100 – 200 seconds. The limiting flux for MIS is \sim 1.4 μ Jy and for AIS, it is \sim 0.2 μ Jy. WISE provides 22 μ m images of the whole sky, with angular resolution 12 arcsec and 5σ point-source sensitivity \sim 6mJy. With both GALEX and WISE all-sky maps available, we are able to derive more accurate SFRs for the COLD GASS sample galaxies.

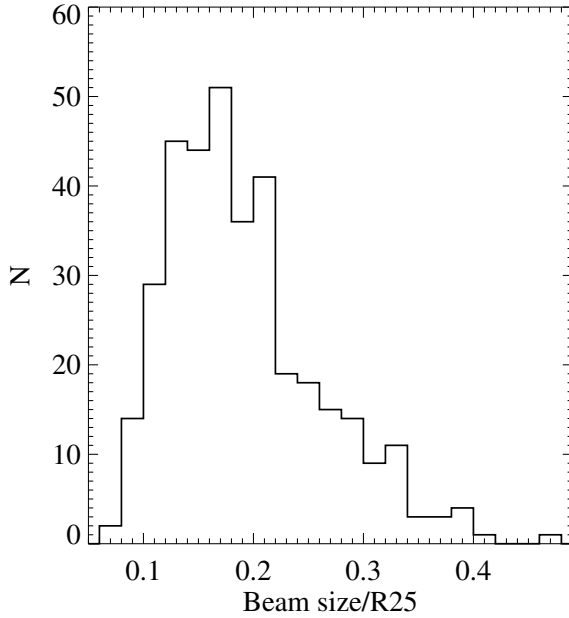


Figure 3.1: Ratio of IRAM beamsize to R_{25} for galaxies in the COLD GASS sample.

3.2.2 HERACLES

To compare molecular gas depletion time trends on sub-kpc scales with results obtained globally, we utilize publicly available data from the HERA CO-Line Extragalactic Survey (HERACLES; Leroy et al. 2008). HERACLES has released CO ($J = 2 - 1$) maps for 48 nearby galaxies, achieving a spatial resolution ~ 13 arcsec and an average H₂ surface density detection limit of $\sim 3 \text{ M}_\odot \text{ pc}^{-2}$. For our comparisons with the COLD GASS results, we select 20 massive galaxies with $\log(M_*/M_\odot) > 10$ from the catalog in Leroy et al. (2013); these selected galaxies are all located within a distance of ~ 20 Mpc.

A variety of ancillary data is available for the galaxies we select from HERACLES sample. This includes FUV images from GALEX AIS (four galaxies) and Nearby Galaxy Survey (NGS; Gil de Paz et al. 2007), 24 μm data from the Spitzer Infrared Nearby Galaxies Survey (SINGS; Kennicutt et al. 2003), HI maps from The HI Nearby Galaxies Survey (THINGS; Walter et al. 2008). SINGS provides MIPS 24 μm images with an angular resolution ~ 6 arcsec and 3σ sensitivity $\sim 0.21 \text{ MJy sr}^{-1}$. The maps (natural-weighting) from THINGS have an angular resolution of ~ 11 arcsec and are sensitive to $\Sigma_{\text{HI}} \geq 0.5 \text{ M}_\odot \text{ pc}^{-2}$.

The combination of these public datasets enables us to derive gas and SFR surface

densities as a function of position in the galaxy by dividing the galaxy into a set of square cells using a 1 kpc^2 grid. Galaxy parameters such as distance, R_{25} , inclination angle, position angle are taken from Leroy et al. (2013). Stellar mass contained within each grid cell is estimated by fitting SDSS 5-band photometry measured for the cell to stellar population models.

3.3 Analyses

3.3.1 Molecular gas depletion time in the COLD GASS sample

Since the IRAM 22'' beam size does not cover the entire optical disk of the galaxies in the COLD GASS sample, aperture corrections were applied to derive total molecular gas masses in Saintonge et al. (2011a). In Figure 3.1, we plot the ratio of the IRAM beam size to R_{25} , the 25 mag arcsec $^{-2}$ g -band isophotal radius. As can be seen, the beam radius is typically only a quarter of the optical radius. Because the molecular gas is generally quite concentrated towards the center of the galaxy, the corrections to total gas mass are not large *on average* (Saintonge et al. 2011a). Nevertheless, when calculating molecular gas depletion time, it is much more accurate to evaluate all quantities within the central 22'' region of the galaxy.

We thus use the observed CO fluxes rather than the corrected CO fluxes from the COLD GASS survey catalogues to derive our estimates of the molecular gas mass. We apply a CO-to-H₂ conversion factor, α_{CO} , in the catalogue to calculate the molecular mass from observed CO line luminosities. In the catalogue, α_{CO} is assumed to have the Galactic value ($4.35 \text{ M}_{\odot}(\text{K km s}^{-1} \text{ pc}^2)^{-1}$) for the main sample galaxies. For the subset of interacting starburst galaxies with high SFR/M_{*} values that were added as extra targets towards the end of the program, α_{CO} is assumed to have the “ULIRG” value ($1 \text{ M}_{\odot}(\text{K km s}^{-1} \text{ pc}^2)^{-1}$). Note that there are only 11 galaxies that require the ULIRG-type α_{CO} in the catalogue. More detailed discussion can be found in Sec 2.3 of Saintonge et al. (2012).

To derive the depletion time, SFR must be estimated within the same region where molecular gas is measured. We place a Gaussian IRAM beam on the FUV and WISE 22 μm maps to derive the central SFR. We note that this was not done in the analysis of Saintonge et al. (2011b), who used total SFR estimates and aperture-corrected CO fluxes. What we want to estimate, is how fast the molecular gas is consumed into stars. To answer this question as accurately as possible, it is clearly preferable that the apertures for the molecular gas and SFR measurements should be closely matched.

We first run SExtractor on the WISE images and mask the detected sources, with

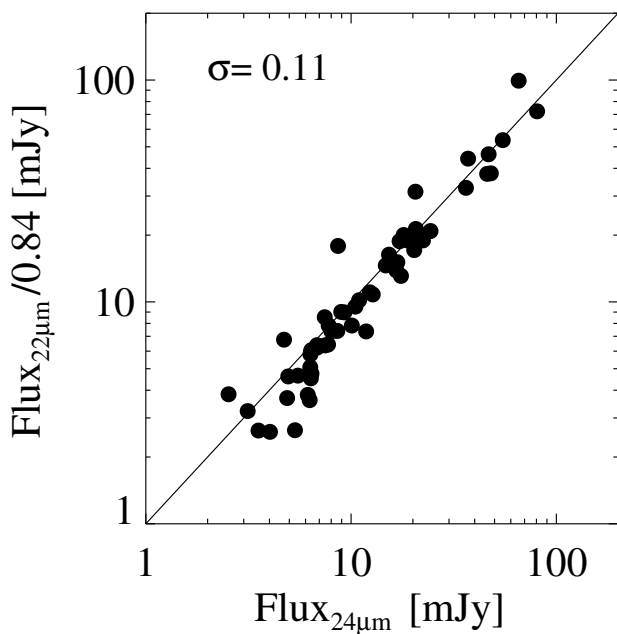


Figure 3.2: Scaled WISE 22 μm fluxes are plotted against Spitzer MIPS 24 μm fluxes for galaxies with WISE detections in the GMACS catalog.

60 3. Variation in molecular gas depletion time: main parameter dependency

the exception of the central target. To remove the background, we first generate the sky image by selecting pixels with values $< 3 \sigma$ above the median value of the image. We then subtract the median value of the sky image as background. Following Wright et al. (2010) and Jarrett et al. (2011), we apply a colour correction and a flux correction for extremely red sources. Finally, we scale the $22\mu\text{m}$ WISE fluxes so that they have the same normalization as the MIPS $24\mu\text{m}$ fluxes. Using the SED template of normal galaxies from Chary & Elbaz (2001), the flux ratio between WISE $22\mu\text{m}$ and Spitzer MIPS $24\mu\text{m}$ filters is ~ 0.841 at a redshift $z < 0.05$.

One question is whether there is much scatter around this ratio. We use the GMACS catalog from Johnson et al. (2007) to answer this question. The catalogue provides a sample located in two sky regions: the Lockman Hole (part of the Spitzer Wide-area InfraRed Extragalactic survey; SWIRE) and the Spitzer Extra-Galactic First Look Survey (FLS). The median stellar mass of galaxies in this sample is $5 \times 10^{10} M_{\odot}$ and the median redshift is 0.11. The $22\mu\text{m}$ WISE data is not as deep as SWIRE and FLS surveys, so we only obtain secure $22\mu\text{m}$ measurements for ~ 60 galaxies from the catalogue of Johnson et al. (2007). We predict the fluxes at MIPS- $24\mu\text{m}$ by dividing by 0.84, the value estimated from our single template. The comparison between the pseudo and observed fluxes at Spitzer- $24\mu\text{m}$ is plotted in Figure 3.2. As can be seen, the predicted values (y-axis) match the observed values (x-axis) very well and the the scatter is only ~ 0.11 dex.

Our analysis of the FUV images involves first masking stars and background galaxies using the same procedure applied to the WISE images. We correct for the effects of Galactic extinction using the extinction maps of Schlegel et al. (1998). Finally, we adopt the combined GALEX FUV plus MIPS $24\mu\text{m}$ relation in Leroy et al. (2008) to estimate the total SFR.

In Figure 3.3, we compare the total SFRs derived from FUV plus IR with the SFRs derived via SED-fitting method from the COLD GASS catalogue. There is no significant offset in mean normalization between the two estimates, but there is considerable scatter of around a factor of two. There are 9 galaxies for which the estimates differ by factors of 5 – 10. Some of these are very dusty galaxies with $\text{SFR}_{\text{IR}}/\text{SFR}_{\text{UV}}$ ratios much larger than the average, where SFRs have been underestimated by the SED-fitting method. The galaxies with SFRs overestimated by SED-fitting method have $\text{SFR}_{\text{IR}}/\text{SFR}_{\text{UV}}$ ratios close to the mean value, but NUV-r colours that are very red, indicative of old stellar populations.

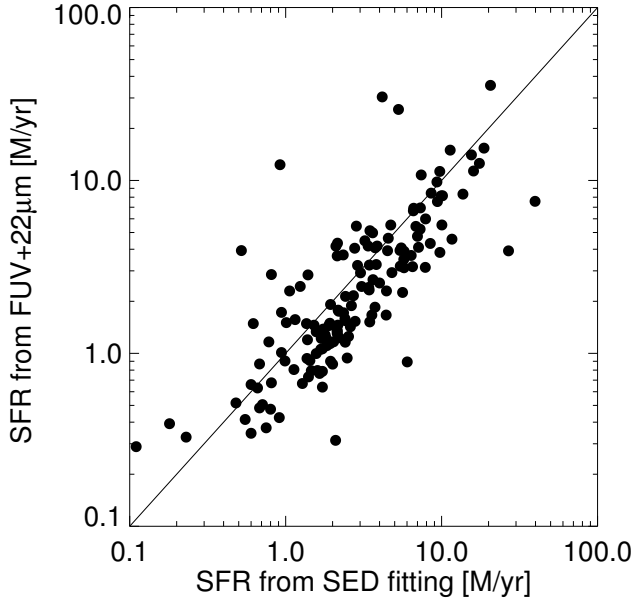


Figure 3.3: Comparison of SFR estimates from the SED-fitting method presented in Singtone et al (2011) and the combination of FUV plus $22\mu\text{m}$.

3.3.2 Properties in the HERACLES sample

Calculation of molecular gas depletion time

We follow the procedures outlined in Leroy et al. (2008) and Bigiel et al. (2008) to calculate the molecular gas depletion time in $1\text{-kpc} \times 1\text{-kpc}$ grid cells. Depletion time in our work is defined as $\Sigma_{\text{H}_2}/\Sigma_{\text{SFR}}$.

We briefly summarize our steps as follows. We first derive Σ_{H_2} in each 1-kpc grid cell from the reduced HERACLES CO maps adopting the Galactic α_{CO} value, $4.35 \text{ M}_{\odot} \text{ pc}^{-2} (\text{K km s}^{-1})^{-1}$. To derive the Σ_{SFR} , we apply the colour-based masks described in Muñoz-Mateos et al. (2009) to remove stars and background galaxies for the FUV and $24\mu\text{m}$ images. We check the images again by visual inspection and mask the stars by hand when necessary. We correct the FUV images for Galactic extinction using the maps of Schlegel et al (1998). All the images are convolved to $\sim 13''$ HERACLES resolution using the kernels provided in Aniano et al. (2011). Leroy et al. (2012) pointed out that cirrus emission from old stellar populations could contribute up to $\sim 20\%$ of the total IR luminosity. To remove the cirrus contribution, we apply the method suggested in sec 8.2 of Leroy et al (2012). With gas, $24\mu\text{m}$, and FUV data in hand, they recommended that

62 3. Variation in molecular gas depletion time: main parameter dependency

a first-order cirrus emission correction could be made using the total gas surface density, i.e. the sum of Σ_{H_2} and Σ_{HI} , where Σ_{HI} is obtained from THINGS data. After we remove this cirrus emission from the $24\mu\text{m}$ emission following equation (15) in Leroy et al. (2012), we then adopt their updated calibration coefficient to calculate the SFRs from the linear combination of the FUV and $24\mu\text{m}$ luminosities.

We exclude bins with $\Sigma_{\text{SFR}} < 10^{-3} \text{ M}_{\odot} \text{ yr}^{-1} \text{ kpc}^{-2}$ since the calibration becomes poor at very low SFR (Leroy et al. 2012). We also discard the bins with $\Sigma_{\text{H}_2} < 3 \text{ M}_{\odot} \text{ pc}^{-2}$, which is the sensitivity limit for the HERACLES CO maps.

Derivation of local parameters

We also derive the local parameters, M_* , stellar mass surface density (μ_*), NUV-r colour, and specific SFR (sSFR) for galaxies in the HERACLES sample. The local parameters are calculated within the 1-kpc scale grids. We measure the SDSS $ugriz$ magnitudes and GALEX FUV, NUV magnitudes after we remove stars and correct for Galactic foreground extinction using the methods described above. We use the SED-fitting method in Wang et al. (2011) to derive the stellar mass. The stellar mass surface density is the stellar mass divided by the physical area of each grid cell , in units of $\text{M}_{\odot} \text{ kpc}^{-2}$. The NUV-r colour is defined as the SDSS r -band minus the GALEX NUV magnitude. The parameter, sSFR, is the SFR divided by the stellar mass within each grid cell. We note that $M_* = \mu_*$ for 1 kpc square grid cells.

Because Leroy et al. (2013) estimated the stellar mass using $3.6\mu\text{m}$ fluxes, different from our SED-fitting method, one might worry that this would play a role in our results. As Leroy et al. (2013) provides the global values of M_* estimated from $3.6\mu\text{m}$ fluxes for the HERACLES sample, we compare our values with theirs. The linear coefficient is 0.9 with scatter 0.11; we do not see a significant systematic difference.

3.4 Results

In this section, we present the results of our new derivation of depletion time and we compare with the results of Saintonge et al. (2011b). We also examine the systematic effects that cause the discrepancy between our results and those of the 2011 study. Finally, we show that we can identify a single global galaxy parameter that drives variations in depletion time among different galaxies.

As in Saintonge et al (20011b), the global galaxy parameters that we investigate are M_* , μ_* , R_{90}/R_{50} , NUV-r, and ssFR. In addition, we consider the ratio of the infrared-to-UV flux, IR/UV. The stellar mass, M_* , is an approximate tracer of the global potential well

Table 3.1: Summary of the best fit linear relations between t_{dep} and galaxy parameters for SFR estimates based on SED fitting (cols 4-7) and based on UV+22 μm measurements (cols 8-11). The relations are parametrized as $\log t_{\text{dep}} = m(x-x_0)+b$

| x parameter | Units | SED fitting | | | | | UV + IR | | | |
|-----------------------------------|--------------------------------|-------------|------------------|-----------------|----------|-------|------------------|-----------------|----------|-------|
| | | x_0 | m | b | σ | r | m | b | σ | r |
| $\log M_*$ | $\log M_\odot$ | 10.7 | 0.40 ± 0.07 | 9.06 ± 1.03 | 0.269 | 0.48 | 0.33 ± 0.06 | 9.44 ± 0.02 | 0.22 | 0.46 |
| $\log \mu_*$ | $\log M_\odot \text{kpc}^{-2}$ | 8.7 | 0.40 ± 0.07 | 8.99 ± 0.88 | 0.275 | 0.44 | 0.17 ± 0.06 | 9.40 ± 0.02 | 0.24 | 0.24 |
| R_{90}/R_{50} | - | 2.5 | 0.37 ± 0.07 | 8.99 ± 0.22 | 0.290 | 0.40 | 0.01 ± 0.06 | 9.40 ± 0.02 | 0.25 | 0.02 |
| NUV-r | mag | 3.5 | 0.18 ± 0.03 | 8.98 ± 0.15 | 0.263 | 0.49 | 0.12 ± 0.03 | 9.41 ± 0.02 | 0.23 | 0.41 |
| $\log \text{SFR}/M_*$ | $\log \text{yr}^{-1}$ | -10.40 | -0.54 ± 0.04 | 9.06 ± 0.62 | 0.221 | -0.70 | -0.37 ± 0.04 | 9.30 ± 0.02 | 0.19 | -0.66 |
| $\text{SFR}_{IR}/\text{SFR}_{UV}$ | - | 1 | - | - | - | - | -0.06 ± 0.05 | 9.38 ± 0.03 | 0.25 | -0.13 |

depth of the galaxy. The stellar surface density, μ_* , and the concentration index, R_{90}/R_{50} , are structural parameters. The concentration index is tightly correlated with the bulge-to-disc ratio. The stellar surface mass density is a convenient way of scaling galaxy size and stellar mass and encodes physical information about angular momentum conservation/loss during the process of galaxy formation. The global NUV-r colour is a measure of the ratio of young stars that are not obscured by dust to older stars. The sSFR parameter is the ratio of the current star formation rate, corrected for dust extinction, to the total stellar mass. For consistency, we derive sSFR within the same 22'' area of the galaxy where we measure the molecular gas mass. The ratio of the total IR to FUV luminosity is a robust estimate of the dust attenuation (e.g., Gordon et al. 2000; Bell 2003; Hao et al. 2011). Although we do not have enough multi-wavelength data to estimate the total IR luminosity, the 24 μm luminosity has been shown to correlate linearly with the total IR luminosity (Wu et al. 2005; Calzetti et al. 2007; Rieke et al. 2009). Thus, we use the ratio of the $\text{SFR}_{22\mu\text{m}}$ to SFR_{FUV} (IR/UV) as our indicator of dust attenuation.

3.4.1 Depletion time based on our new SFR estimates

We plot depletion time results based on our new SFR estimates as a function of global physical properties of galaxies in Figure 3.4. The black circles show galaxies in the representative sample with secure CO, FUV and 22 μm detections. The grey arrows show galaxies with secure CO detections but with SFR upper limits. An extra set of galaxies with high values of SFR/M_* were observed at the end of the COLD GASS program in order to extend the dynamic range in star formation probed by the observations. We will refer to these galaxies as “starburst” systems and we indicate them as red symbols on the figure.

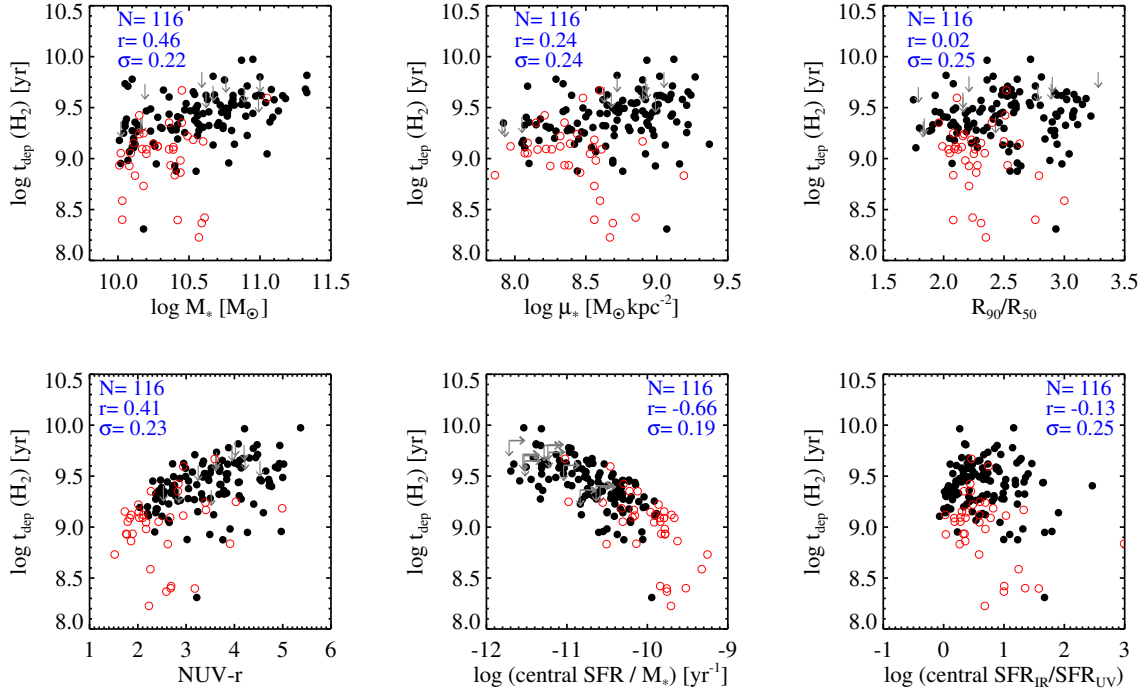


Figure 3.4: Molecular gas depletion time as a function of global galaxy properties. Black circles denote the representative sample of normal galaxies with secure CO, FUV, and IR measurements. Grey arrows denote the normal galaxies with secure CO detections but upper limits on their SFR estimates. Red circles represent the starburst galaxies. The linear relation is fitted to the normal galaxies with secure measurements of both molecular gas and SFR. N , r , and σ indicate the number of galaxies included in the fit, the Pearson correlation coefficient, and the scatter about the best-fit relation.

Some of these galaxies have enhanced infrared luminosity and dust temperature and we thus use the “ULIRG” value of α_{co} ($1 \text{ M}_\odot \text{ pc}^{-2} (\text{K km s}^{-1})^{-1}$) to derive their molecular gas masses. We note that some of these starburst galaxies are interacting/merging systems and it is inevitable to include emission from their companions when we calculate their global properties. To minimize any confusion, we visually identify eight interacting/merging systems and exclude them in the following analyses and discussions. We perform linear fits to galaxies from the representative sample only and the number of galaxies in the sample (N), the Pearson linear correlation coefficient (r), and the scatter (σ) are indicated on the figure.

Our new linear relations are compared with those derived by Saintonge et al. (2011b) in Table 3.1. Three main changes can be seen:

1. The normalization b changes. The resulting depletion times are a factor of two longer than quoted in Saintonge et al. (2011b) and now agree very well with HERACLES results (see later). The change in normalization occurs because the apertures within which we measure the molecular gas and the SFR are now well-matched.
2. The scatter σ in the relations between depletion time and global galaxy parameters is significantly reduced. This occurs for all the relations and is a consequence of our improved star formation rate estimates, which do not have to be corrected for dust in a statistical fashion.
3. The slopes of the relations between depletion time and the structural parameters, μ_* and concentration index R_{90}/R_{50} , are significantly flatter than before. In particular, there is now no correlation at all between depletion time and galaxy bulge-to-disk ratio, whereas Saintonge et al. (2011b) found a very significant correlation.

There are still strong correlations between the depletion time and stellar mass, NUV-r color and sSFR, with only small changes in slope from previously. We note that the depletion time is not dependent on the IR/UV ratio. In the next section, we investigate the systematic effects in the dust extinction properties of the galaxies, which are the main cause of the discrepancy between our work and that of Saintonge et al. (2011b).

3.4.2 Systematic effects caused by dust attenuation

In Figure 3.5, we illustrate how the correlation coefficients r and the scatter σ about the best-fit linear relation between molecular gas depletion time and galaxy properties change when we derive star formation rate purely from the UV flux (SFR_{UV}), purely from the IR flux (SFR_{IR}) and from the sum of the two ($\text{SFR}_{\text{UV+IR}}$). The bar plots show the value of

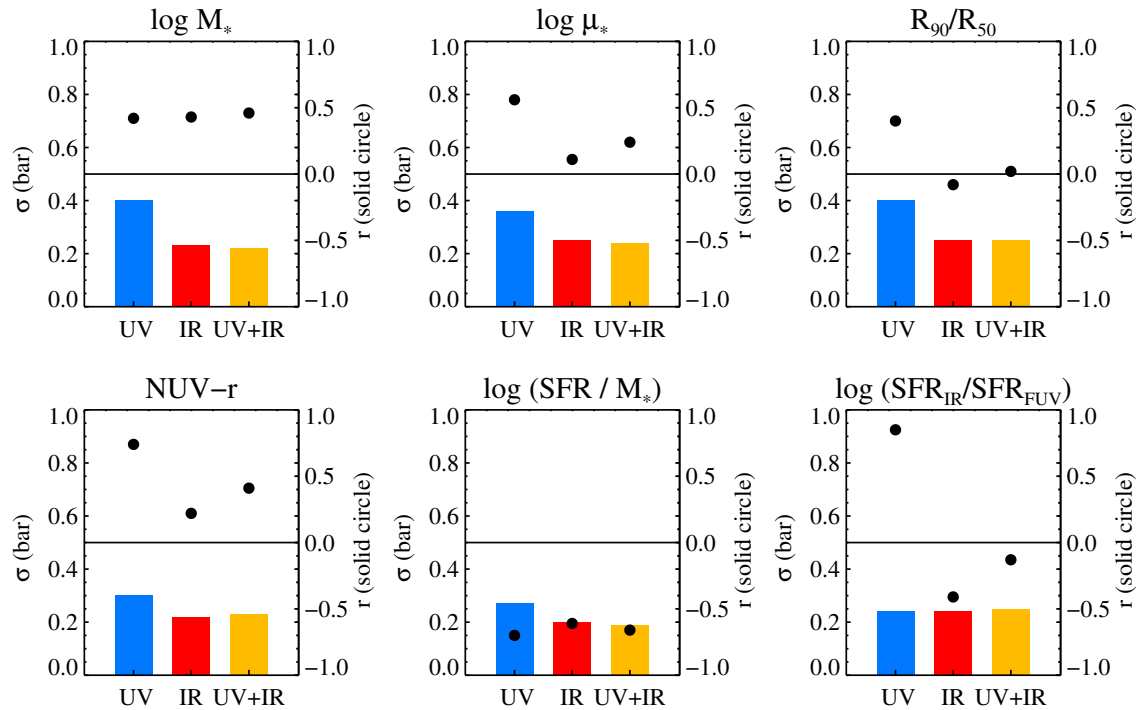


Figure 3.5: The scatter (σ) and the correlation coefficient (r) of the fitted linear relations between depletion time and galaxy parameters based on 3 different SFR tracers: UV+IR, IR, FUV. The bar plots show the value of the scatter as indicated on the left y-axis; the solid circles denote the correlation coefficients as indicated on the right y-axis.

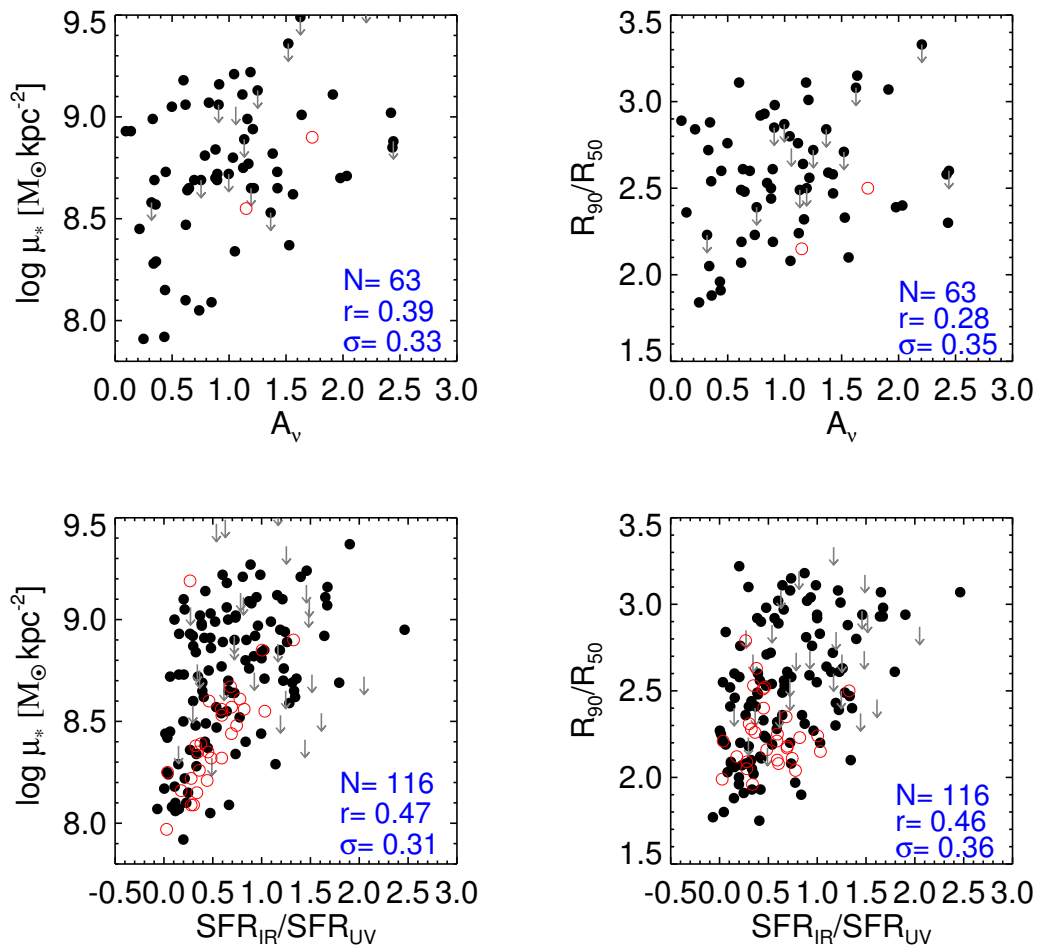


Figure 3.6: Stellar surface density and concentration index as functions of A_v and IR/UV.

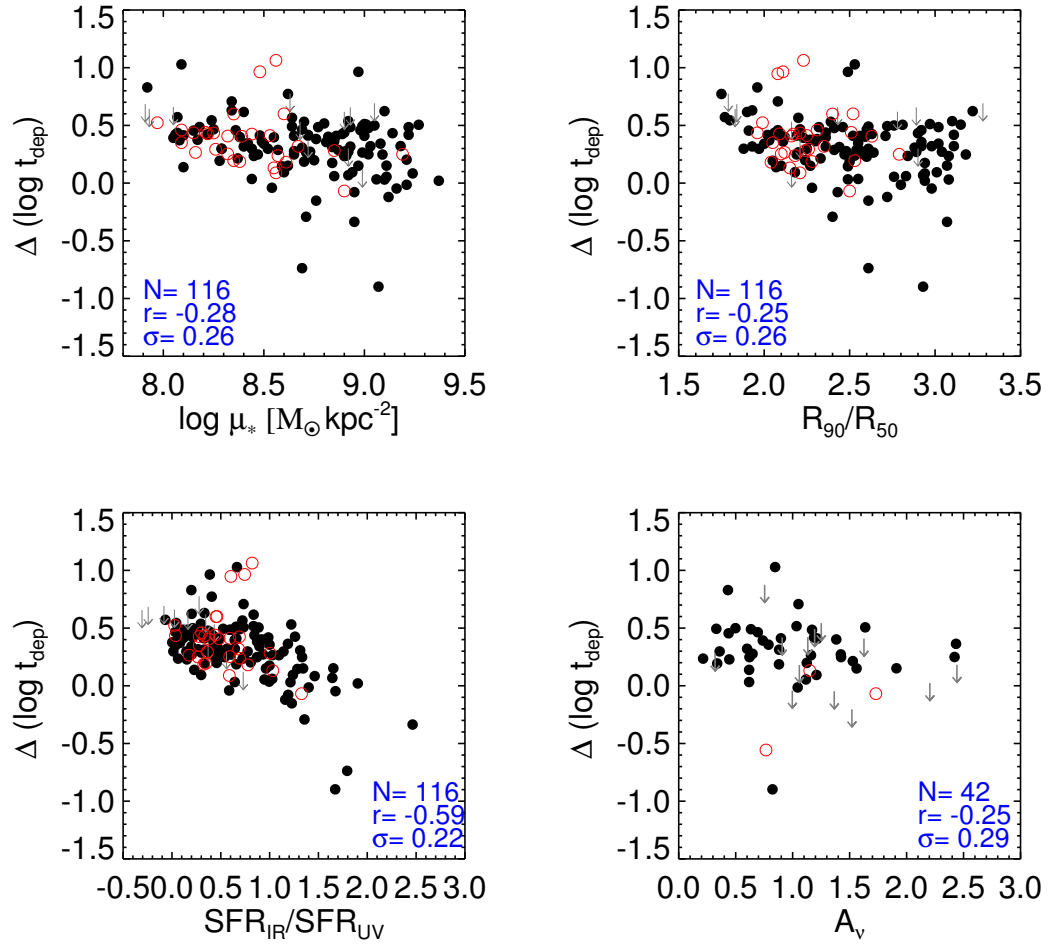


Figure 3.7: Difference in the depletion time, $\Delta (\log t_{\text{dep}})$, measured in Saintonge et al. (2011) and our work as functions of stellar surface density, concentration, IR/UV ratio and dust extinction.

σ , as indicated on the left-hand axis; the solid circles show the correlation coefficients, as indicated on the right-hand axis. We first observe that the scatter tends to be significantly larger for the UV-based relations, and of comparable magnitude for IR and UV+IR-based relations. The strength of the correlations with the structural parameters μ_* and R_{90}/R_{50} is only strong for the UV-based relations, and largely disappears for the SFR_{IR} and $SFR_{\text{UV+IR}}$ relations. In contrast, the strength of the correlations with stellar mass M_* and specific star formation rate SFR/M_* are the same for SFR_{UV} , SFR_{IR} and $SFR_{\text{UV+IR}}$. This supports our conjecture that systematics in IR/UV ratio (or dust extinction) are the main reason for the changes between the results presented in this work and those in Saintonge et al. (2011b).

As both t_{dep} and IR/UV include the UV flux, it is worth using an independent estimate of dust extinction to investigate the effect of dust systematics on our results. A subsample of the COLD GASS galaxies have long-slit spectra along their major axes Moran et al. (2012), from which we can calculate the extinction A_ν from the Balmer decrement, $L(H_\alpha)/L(H_\beta)$. The spectra were spatially binned outward from the galaxy center to ensure an adequate S/N in every bin. We exclude the bins with low S/N for the Balmer lines and weight the bins with reliable measurements by the stellar mass contained within the annulus spanned by the bin boundaries, to get a representative A_ν value for the whole galaxy.

In Figure 3.6, we plot μ_* and R_{90}/R_{50} as a function of A_ν and the IR/UV ratio. These structural parameters correlate strongly with both A_ν and IR/UV. In order to ascertain whether these correlations are responsible for differences in our depletion time results with respect to those of Saintonge et al (2011b), we calculate the difference between the two depletion time estimates $\Delta \log(t_{\text{dep}}) = \log t_{\text{dep}} (\text{our work}) - \log t_{\text{dep}} (\text{Saintonge et al. 2011b})$. In Figure 3.7, $\Delta \log(t_{\text{dep}})$ is plotted against μ_* , R_{90}/R_{50} , IR/UV, and A_ν . As can be seen, our depletion time estimates become shorter with respect to those in Saintonge et al. (2011b) when galaxies have higher stellar surface densities and larger concentration indices. The difference $\Delta \log(t_{\text{dep}})$ is also correlated with IR/UV and A_ν .

3.4.3 Primary or induced correlation?

Our results show that molecular gas depletion time is strongly correlated with M_* , NUV-r and sSFR, and is more weakly correlated with μ_* . One question is whether these correlations are independent of each other. Almost all global galaxy parameters correlate strongly with stellar mass, so one might expect the molecular gas depletion time to correlate with M_* even if the *primary* correlation is with some other parameter. In this section, we attempt to separate primary and induced correlations through analysis of residuals. We

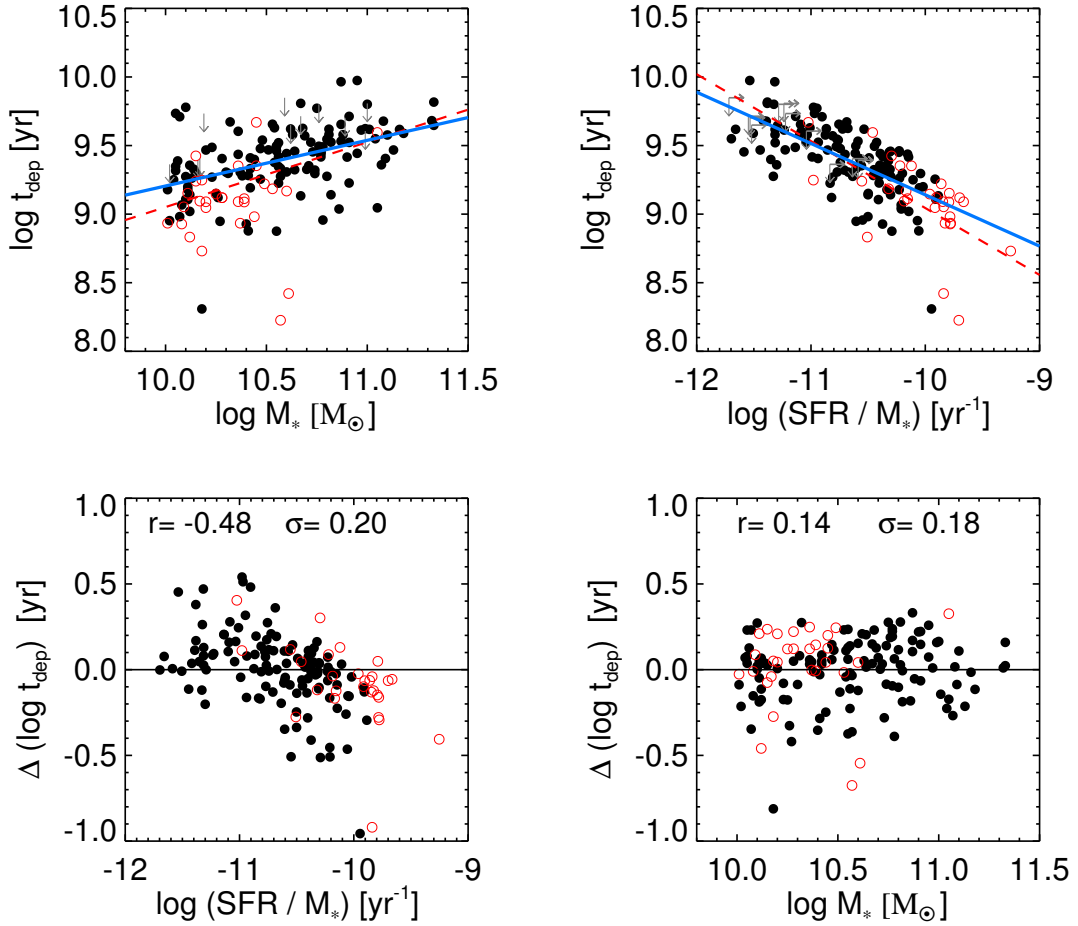


Figure 3.8: Upper panels: molecular gas depletion time is plotted as a function of M_* and SFR/M_* . Blue lines show the best-fit linear relation for galaxies in the representative sample, while the red lines show the best-fit linear relation for the sample that includes the starburst systems. Bottom left : The residuals from the best fit $t_{\text{dep}} - M_*$ relation are plotted as a function of SFR/M_* . Bottom right: The residuals from the best fit $t_{\text{dep}} - \text{SFR}/M_*$ relation are plotted as a function of M_* .

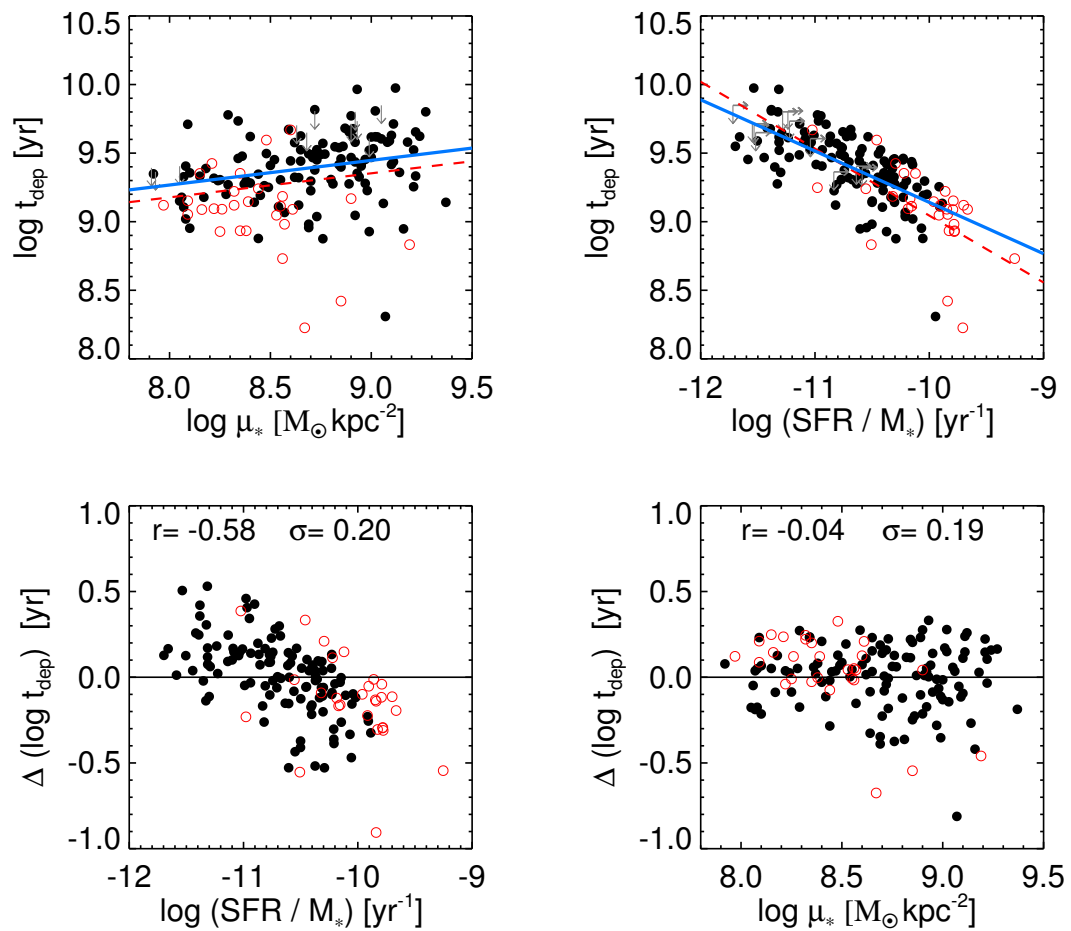


Figure 3.9: As in Figure 3.8, except that M_* has been replaced by μ_*

note that NUV-r and sSFR have similar physical meaning in that they both serve as an indicator of the ratio of young-to-old stars in the galaxy, so for simplicity we only consider sSFR, which does not depend on dust extinction.

We fit a linear relation to the t_{dep} versus M_* relation and ask whether the residuals of t_{dep} from this relation are correlated with sSFR. Similarly, we also fit a linear function to the $t_{\text{dep}}-\text{sSFR}$ relation and examine if the residuals correlate with M_* . The results are shown in Figure 3.8. The blue line shows the fit to the representative sample, while the red line shows the fit to the combination of normal and starburst galaxies. The residuals are measured with respect to the blue line.

As seen in the lower panel of Figure 3.8, the residuals from the $t_{\text{dep}}-M_*$ relation correlate strongly with sSFR, while the residuals from the $t_{\text{dep}}-\text{sSFR}$ relation correlate very weakly with M_* . We note that there is one galaxy with particularly low depletion time (0.1 Gyr) and with a central sSFR $\sim 10^{-9.9} \text{ yr}^{-1}$, which causes most of this weak correlation. In the MPA-JHU catalog, this galaxy has been classified as a galaxy with an AGN in the center. If this galaxy is excluded, there is no longer any significant correlation between the t_{dep} residuals and stellar mass.

We carry out the same exercise for the relation between t_{dep} and μ_* . The results are plotted in Figure 3.9. The residuals of the $t_{\text{dep}}-\mu_*$ relation are strongly correlated with sSFR, with a significance $r = -0.58$. By contrast, there is no relation between μ_* and the residuals of the $t_{\text{dep}}-\text{sSFR}$ relation. We again conclude that the primary relation is the one between t_{dep} and sSFR.

The trend of t_{dep} with sSFR on global scale can be also seen in the results based on a fixed α_{CO} from Leroy et al. (2013). In their Table 6, the rank coefficient (1st column) for $t_{\text{dep}}-\text{sSFR}$ relation is -0.38 for all sample and -0.27 for the sample with $\log M_* > 10$. This indicates there is a dependence of t_{dep} on sSFR though this dependence is weaker than our finding. This might be due to differences in the sample size and the range of the galaxy properties, as discussed in Sec 3.1.

3.4.4 Comparison with results for 1 kpc grids

In order to examine whether the trends we find in the COLD GASS sample are similar to those found on smaller (1 kpc) scales, we utilize data from the HERACLES project. We derive depletion time on grids with 1 kpc^2 area and study the dependence on local physical properties, such as stellar surface density, NUV-r color, sSFR, and IR/UV ratio. As discussed in Section 3.3.2, bins with low SFR surface densities are excluded and we also remove the IR cirrus emission from old stellar populations following the procedures outlined in Leroy et al. (2012).

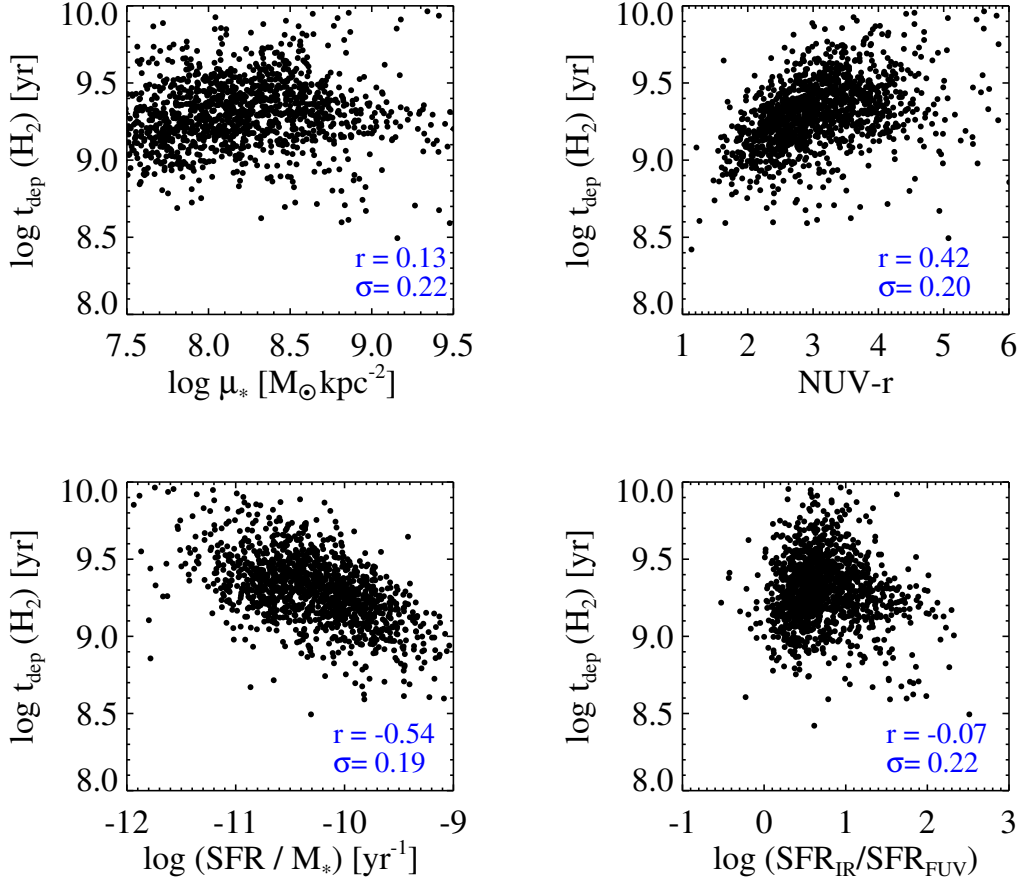


Figure 3.10: Molecular gas depletion times evaluated within 1kpc^2 area grid cells as functions of stellar surface density, NUV-r color, sSFR and IR/UV for galaxies from the HERACLES sample.

Table 3.2: Summary of the best-fit linear relations between t_{dep} and local parameters for grid scale data from the HERACLES sample. The relations are parametrized as $\log t_{\text{dep}} = m(x-x_0)+b$

| x parameter | Units | x_0 | m | b | σ | r |
|---|---------------------------------------|--------|------------------|-----------------|----------|-------|
| $\log \mu_*$ | $\log \text{M}_\odot \text{kpc}^{-2}$ | 8.7 | 0.06 ± 0.01 | 9.33 ± 0.01 | 0.22 | 0.13 |
| NUV-r | mag | 3.5 | 0.12 ± 0.01 | 9.35 ± 0.01 | 0.20 | 0.42 |
| $\log \text{SFR}/\text{M}_*$ | $\log \text{yr}^{-1}$ | -10.40 | -0.24 ± 0.01 | 9.32 ± 0.01 | 0.19 | -0.54 |
| $\text{SFR}_{\text{IR}}/\text{SFR}_{\text{UV}}$ | - | 1 | -0.04 ± 0.01 | 9.29 ± 0.01 | 0.22 | -0.07 |

74 3. Variation in molecular gas depletion time: main parameter dependency

We plot the molecular gas depletion time versus stellar surface mass density, NUV-r color, sSFR, and IR/UV ratio in Figure 3.10. As in the COLD GASS sample, the depletion time on 1 kpc grid scales in the HERACLES sample is strongly correlated with NUV-r and sSFR, but does not show significant dependence on the local stellar mass density or the IR/UV ratio.

To quantify the strength of the correlations on local scales, we also fit linear relations to the HERACLES data and summarize the parameters of the best-fit relations in Table 3.2. Generally, the slopes and the correlation coefficients are somewhat lower for the grid measurements compared to the COLD GASS sample. The slope and the significance of the $t_{\text{dep}} - \text{sSFR}$ correlation on grid scales are -0.24 and -0.54 , compared to -0.37 and -0.66 on global scales.

We plot the $t_{\text{dep}} - \text{sSFR}$ relations for grid and global scales, as well as the best-fit linear relations, in Figure 3.11. We separate the grid cells into those located in the bulge-dominated and disk-dominated regions of galaxies as follows. We apply the GALFIT code (Peng et al. 2010) to the SDSS r-band images to decompose galaxies into bulges and disks. To fit the luminosity profile of the galaxies, the code assumes a two-component model, Sérsic bulge plus Sérsic disk profile, where the Sérsic n values for the bulge and disk are allowed to vary from 1.5 to 4 and from 0.8 to 1.2, respectively.

Two main conclusions emerge from the results shown in Figure 3.11: a) the global $t_{\text{dep}} - \text{sSFR}$ relation for the COLD GAS galaxies overlaps that for the *disk grid cells* quite well. b) The number of grid cells in bulge-dominated regions is quite low. Some of these bulge grid cells do fall below the fitting relation. This is consistent with the results in Leroy et al. (2013), where shorter molecular gas depletion time were found in the nuclear regions of some galaxies. Nevertheless, it is quite clear from Figure 3.11 that the main $t_{\text{dep}} - \text{sSFR}$ correlation is driven by disk-dominated regions of the galaxy.

Because the SFR estimate is included in the calculation of both t_{dep} and sSFR, one might worry that the correlation between t_{dep} and sSFR might be induced rather than a real correlation. This issue was addressed in detail in Saintonge et al. (2011b). It was demonstrated that molecular gas depletion time correlated very well with 4000 Å break strength measured from the SDSS fiber spectrum, which provides an independent estimate of the ratio of young-to-old stars in the galaxy. In addition, these authors carried out Monte Carlo simulations where they showed that the observed relation was too strong to be “induced” by scatter arising from measurement errors.

In Figure 3.12, we investigate whether the depletion time has dependence on the molecular gas surface density, Σ_{H_2} and the molecular gas surface density scaled by the stellar mass within the grid cell, Σ_{H_2}/M_* . As can be seen, there is no dependence of t_{dep} on

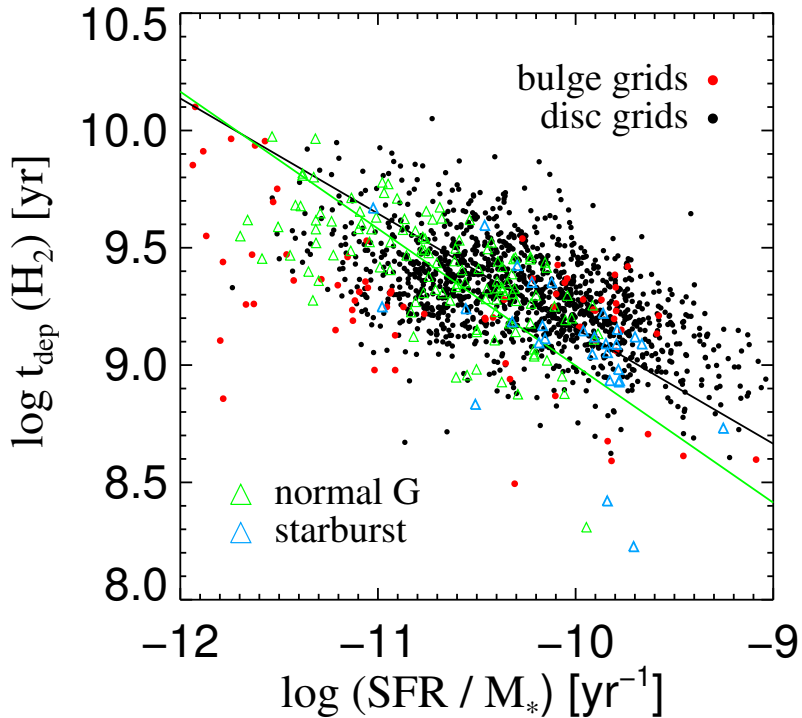


Figure 3.11: Comparison of the global t_{dep} -sSFR relation for COLD GASS galaxies and for measurements on 1 kpc grid scales for galaxies in the HERACLES sample. Green and blue triangles denote the representative and starburst samples from the COLD GASS survey. Black and red points denote the grid measurements in *disc* and *bulge* regions of galaxies from the HERACLES sample. Linear relations are fit to both the COLD GASS representative sample (green line) and the HERACLES data (black line).

Σ_{H_2} . However, when Σ_{H_2} is scaled by the stellar mass measured in the grid cell, a mild dependence on Σ_{H_2}/M_* , with the linear coefficient $r = -0.11$, is found. This result might indicate that the *local density of evolved stars has an effect on the molecular gas depletion time*.

3.5 Summary and discussion

In this chapter, we re-analyze the relations between global molecular gas depletion time and a variety of galaxy parameters for nearby galaxies from the COLD GASS survey with stellar masses in the range $10^{10} - 10^{11.5} M_\odot$ and redshifts in the range 0.02– 0.05. The molecular gas mass is estimated from the CO(J=1-0) line measurements and our updated estimates of star formations use the combination of GALEX FUV and WISE 22 μm data. In agreement with Saintonge et al. (2011), we find that the molecular gas depletion time depends strongly on galaxy stellar mass, NUV-r colour and sSFR. Our results differ from those in Saintonge et al. (2011) in that we find that the dependences of the depletion time on galaxy structural parameters such as stellar surface density and concentration index, are weak or absent. We demonstrate that the differences with the Saintonge et al. (2011) analysis arise from the fact that dust extinction as measured by the ratio of 22 micron to far-UV flux in the galaxy, correlates strongly with μ_* and concentration. We further demonstrate that the dependence of t_{dep} on M_* is actually driven by the primary correlation between t_{dep} and sSFR.

We compare our results with molecular gas depletion time estimates on 1-kpc scales using publicly available data from the HERACLES survey. We find remarkably good agreement with our global t_{dep} versus sSFR relation. On sub-galactic scales, we are able to ascertain that t_{dep} is not correlated with Σ_{H_2} , but is weakly correlated with Σ_{H_2}/M_* , indicating that the presence of old stars has an effect on the ability of molecular clouds to form new stars.

We note that the parameter, sSFR, is the ratio of current SFR to the stellar mass built up by the past star formation. The strong correlation between t_{dep} and sSFR, extending over a factor of 10 in t_{dep} in our sample, leads to the inference that the molecular gas depletion time is dependent on the star formation history of the galaxies. Those galaxies with high current-to-past averaged star formation activity, will drain their molecular gas reservoir sooner.

The influence of metallicity on α_{CO} value is always a concern whenever the star-formation law is studied. One might question whether our assumption of a fixed α_{CO} value is appropriate. Sandstrom et al. (2013) studied variations in α_{CO} using a subset of

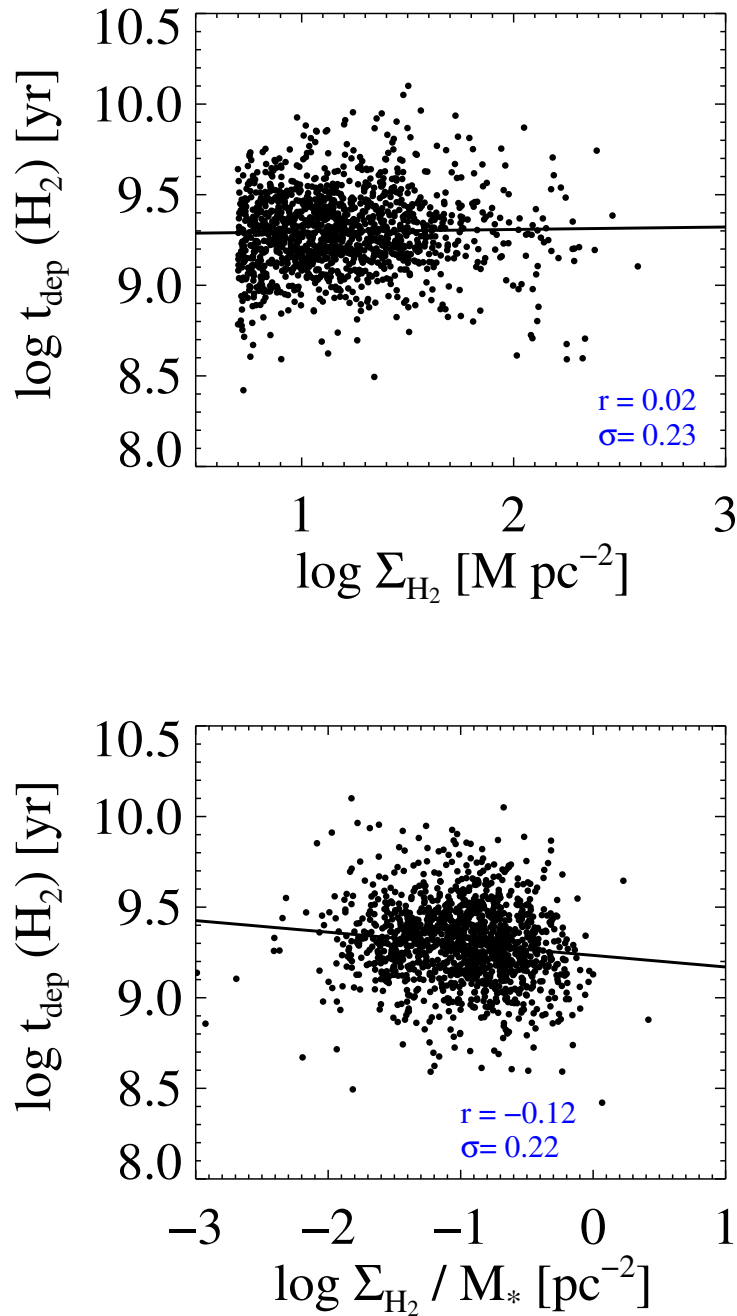


Figure 3.12: Depletion time as a function of molecular gas surface density and molecular gas surface density per unit stellar mass for the HERACLES grid measurements.

78 3. Variation in molecular gas depletion time: main parameter dependency

26 galaxies from the HERACLES sample. They showed that metallicity effects on α_{CO} are very weak over the metallicity range spanned by the HERACLES disc galaxies. α_{CO} has been shown to depart significantly from the typical Galactic value only below a metallicity $\sim 1/3 - 1/2$ solar (e.g., Glover & Mac Low 2011; Leroy et al. 2011; Bolatto et al. 2013). We would also expect to see a dependence of gas depletion time on the dust content of the galaxy, if our results were simply a consequence of variations in α_{CO} . From Figures 3.4 and 3.10, we know that the depletion time on both global and local scales does not show any correlation with IR/UV ratio.

Sandstrom et al. (2013) did find that α_{CO} is dependent on other galaxy parameters, such as average radiation field intensity, PAH fraction, stellar mass surface density, SFR surface density and dust mass surface density. The α_{CO} value appears to decrease as the stellar mass and SFR surface densities increase. We note that these two effects cancel when we derive sSFR. We conclude that it is unlikely that the small variations in α_{CO} found by Sandstrom et al. (2013) explain our observed relation between t_{dep} and sSFR.

Next step, we investigate whether the strong $t_{\text{dep}}-\text{sSFR}$ is connected to the structure of the interstellar medium, such as the presence of spiral arms. Gas clouds are compressed in spiral arm regions and one might hypothesize that galaxies with high SFR/M_* might have more arm structures than those with low SFR/M_* , leading to the observed variation in molecular depletion time scales in disks.

Chapter 4

The variation in molecular gas depletion time: the impact of galaxy internal structures

Based on

Mei-Ling Huang et al.

MNRAS, 450, 1375 (2015)

4.1 Introduction

As demonstrated in Chapter 3, we improve on the COLD GASS project by estimating SFR with the combination of GALEX FUV and WISE $22\mu\text{m}$ data within fixed apertures matched to the $22''$ beam size of the gas observations. Dependences of the depletion time on galaxy structural parameters such as stellar surface density and concentration index are then found to be much weaker, or even absent. We go on to demonstrate that the *primary dependence* of t_{dep} is on sSFR. All other remaining correlations, such as the $t_{\text{dep}} -$ stellar mass relation, are demonstrated to be secondary, i.e., induced by the fact that sSFR in turn correlates with a variety of other global galaxy parameters. We note that a comprehensive study based on 500 star forming galaxies at redshifts from $z = 0$ to 3 also supports our findings (Genzel et al. 2015).

We also compared the results obtained from the COLD GASS galaxies to estimates of t_{dep} on 1 kpc scales using high-resolution CO and SFR maps from the HERACLES survey. The global $t_{\text{dep}} - \text{sSFR}$ relation derived from the COLD GASS sample and that derived from

1 kpc grids placed on HERACLES galaxies agree remarkably well. This suggests that the local molecular gas depletion time is dependent on the local fraction of young-to-old stars and that galaxies with high current-to-past-averaged star formation activity, will consume their molecular gas reservoir sooner.

Another aspect that has not been fully understood is the role of galaxy internal structures such as bulges, arms, bars, and rings in determining the molecular gas depletion time. We note that simply using all available grids from the whole galaxy or integrated values of gas mass and SFR to study molecular gas depletion times might smooth out variations caused by different structures.

Many studies have investigated whether the star formation efficiency (SFE) varies in different galactic environments. For instance, Meidt et al. (2013) studied the inner region of the spiral galaxy M51 with a high resolution CO (1-0) map (~ 40 pc) and proposed that streaming motions, induced by gravitational instabilities due to bars and arms, cause variations in gas depletion time. Momose et al. (2010) observed a barred spiral galaxy, NGC 4303, with CO (1-0) observations and found that its arms have twice higher SFEs than its bar, although strong CO emission is both seen in the bar and the disc region along the arms. Fujimoto et al. (2014) proposed that these results could be understood in a model where star formation is regulated by collisions between molecular clouds. However, other studies have come to the opposite conclusion about the viability of the cloud collision model (Foyle et al. 2010; Eden et al. 2012). Other observational studies using CO(1-0) line luminosities as the gas tracer and H α or 24 luminosities as the SFR tracer have demonstrated that the SFE in spiral arms is enhanced compared to regions outside the arms (e.g., Lord & Young 1990; Knapen et al. 1996; Rebolledo et al. 2012; Hirota et al. 2014).

We note that most of these studies explored the influence of structures on SFE based on samples of one or only a few galaxies, and they did not consider variations in SFE with respect to the t_{dep} –sSFR relation. In this chapter, we try to understand whether galaxy structures induce significant variation in molecular gas depletion time by systematically separating the grids into those in bulge, arm, bar, and ring regions, and by studying how the local depletion time from these different regions varies with respect to the established t_{dep} –sSFR relation.

This chapter is organized as follows. We describe the multiwavelength data sets used in this work in Section 4.2, and our methods for identifying galaxy structures and deriving t_{dep} and sSFR on local scales in Section 4.3. Our results are presented in Section 4.4, where we look at the t_{dep} –sSFR relations for the grids in the bulge, arm, bar, and ring regions respectively. Finally, we compare our results with previous studies and discuss our findings

in Section 4.5.

4.2 Data

In this section we introduce the data sets we use in this work. The HERACLES sample provides spatially-resolved CO maps with resolution $\leq 1\text{kpc}$, appropriate for pixel-by-pixel studies. Because of this good resolution, we are able to identify the pixels lying in galaxy structures such as bulges or spiral arms. ATLAS^{3D} galaxies are mostly early-type galaxies and are included because this data supplements the number of data points we are able to extract from the bulge-dominated regions of galaxies. The COLD GASS project targets more distant sources and therefore provides only integrated values of the molecular gas mass. Nevertheless, the large sample size gives us the opportunity to carry out a statistical analysis of global relations between gas depletion time and other galaxy properties.

4.2.1 HERACLES

To study molecular gas depletion time on sub-kpc scales, we use public data from the HERACLES. HERACLES has released CO ($J = 2 - 1$) maps for 48 nearby galaxies, achieving a spatial resolution ~ 13 arcsec and an average H₂ surface density detection limit of $\sim 3 \text{ M}_\odot \text{ pc}^{-2}$. We analyze 21 massive galaxies with $\log(M_*/M_\odot) \geq 10$ from the catalog in Leroy et al. (2013) so that we avoid those low-mass galaxies with less reliable H₂ mass measurements. All our selected galaxies are located within a distance of ~ 20 Mpc.

A variety of ancillary data is available for the HERACLES sample, which allow us to derive the SFR and stellar mass surface densities. The relevant data includes FUV images from GALEX All-sky Imaging survey (AIS) and Nearby Galaxy Survey (NGS) data, 24 μm data from the Spitzer Infrared Nearby Galaxies Survey (SINGS), HI maps from The HI Nearby Galaxies Survey (THINGS), and optical images from Sloan Digital Sky Survey (SDSS). FUV images from GALEX satellite have effective wavelength 1528 Å and angular resolution ~ 4.3 arcsec FWHM. SINGS provides MIPS 24 μm images with an angular resolution ~ 6 arcsec and 3σ sensitivity $\sim 0.21 \text{ MJy sr}^{-1}$. The maps (natural-weighting) from THINGS have an angular resolution of ~ 11 arcsec and are sensitive to $\Sigma_{\text{HI}} \geq 0.5 \text{ M}_\odot \text{ pc}^{-2}$.

Combining these public data sets, we estimate gas, SFR, and stellar mass surface densities as a function of position in the galaxy by dividing the galaxy into a set of square cells with 1 kpc^2 size. In this way, we are able to separate the grids within bulges, arms, bars, rings from those in the rest of the galaxy. Galaxy parameters such as distance, inclination angle, position angle are taken directly from Leroy et al. (2013).

4.2.2 ATLAS^{3D}

To increase the amount of data in bulge regions, we make use of a subset of the galaxies observed as part of the ATLAS^{3D} project (Cappellari et al. 2011), with publicly-available resolved interferometric CO(1-0) maps (Alatalo et al. 2013). The full ATLAS^{3D} sample consists of a volume-limited sample of 260 nearby early-type (elliptical E and lenticular S) galaxies (ETGs) with a cut-off absolute magnitude of $M_K = -21.5$. The ATLAS^{3D} galaxies were observed in CO(1-0) and CO(2-1) by the IRAM 30m telescope (Young et al. 2011), and those with detected CO integrated fluxes larger than 19 Jy km s^{-1} were imaged using the Combined Array for Research in Millimeter Astronomy (CARMA; Alatalo et al. 2013). This data set includes 30 ETGs. Together with 10 CO-detected galaxies that have interferometric CO(1-0) data from the literature, there are a total 40 ETGs with resolved CO maps in the ATLAS^{3D} sample. The reader is referred to Alatalo et al. (2013) for further details about the sample, the observations and the analyses.

We derive SFR using the combination of FUV emission from GALEX data and mid-infrared emission at $22\mu\text{m}$ from WISE data. The FUV maps are retrieved from GALEX Data Release 7 products. When several atlas images from different observing programs are available, we always use the one with the longest exposure time. The exposure time for $\sim 2/3$ of the sample is longer than 1500 seconds; the rest of galaxies have data from the AIS program with typical exposure time $\sim 100 - 200$ seconds and limiting magnitude ~ 20.5 AB magnitude. There are 3 galaxies without FUV observations from GALEX. WISE provides $22\mu\text{m}$ images of the whole sky, with angular resolution 12 arcsec and 5σ point-source sensitivity $\sim 6\text{mJy}$. All galaxies have WISE observations. The stellar mass is derived from SDSS 5-band images using a SED-fitting method; the SDSS images are downloaded from SDSS Data Release 9.

In Figure 4.1 we compare the basic properties of the galaxies in the HERACLES and ATLAS^{3D} samples. Generally, their stellar masses are comparable. The HERACLES galaxies are much closer than the ATLAS^{3D} galaxies, so the angular disc sizes (R_{25}) of the former sample are larger than the latter sample. The distributions of the concentration index, R_{90}/R_{50} , which is tightly related to the bulge-to-disc ratio of the galaxy, reflect the fact that the ATLAS^{3D} galaxies are mostly ETGs and the HERACLES sample consists of mostly disc galaxies.

4.2.3 COLD GASS

The sample is drawn from the COLD GASS survey catalogue, which contains CO ($J = 1 - 0$) line measurements from the IRAM 30m telescope for ~ 360 nearby galaxies with

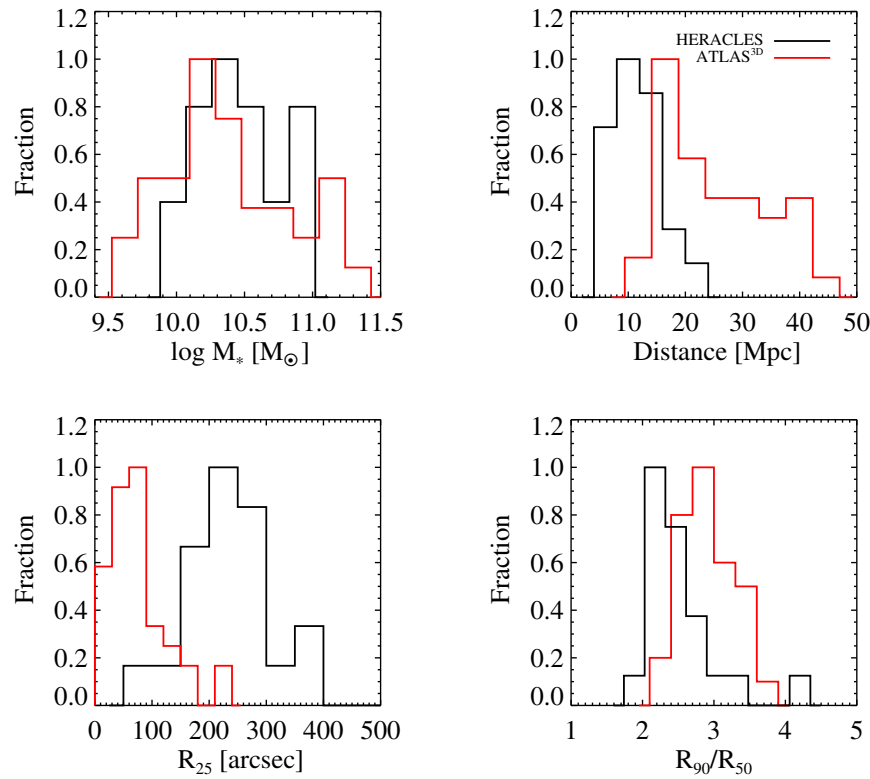


Figure 4.1: Comparison of stellar mass, distance, B-band isophotal radius at 25 mag arcsec⁻² (R_{25}), concentration index (R_{90}/R_{50}) for HERACLES galaxies (black line) and ATLAS^{3D} galaxies (red line).

stellar masses in the range $10^{10} - 10^{11.5} M_{\odot}$ and redshifts in the range $0.025 < z < 0.05$. We only select the galaxies with detected CO fluxes in our studies.

In the same fashion as was done for the ATLAS^{3D} sample, we derive SFR by summing GALEX FUV and WISE 22 μ m luminosities and we estimate stellar mass by fitting stellar population synthesis models to SDSS 5-band images. We retrieve the FUV maps from GALEX Data Release 7 products; the maps with the longest exposure time are always preferred. Most of our FUV images are from the Medium Imaging survey (MIS) with typical exposure time \sim 1500 seconds; 81 out of 366 galaxies only have data from the AIS program with typical exposure time \sim 100 – 200 seconds. The limiting magnitude for MIS is 23.5 AB magnitude and for AIS, it is 20.5 AB magnitude. All galaxies have both WISE and SDSS imaging data.

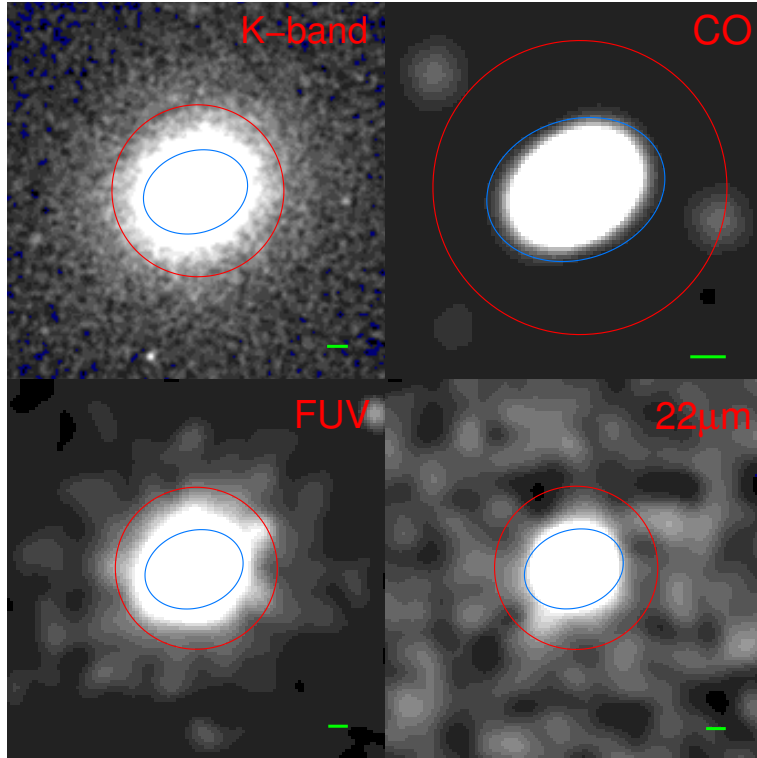


Figure 4.2: 2MASS K-band (upper left), CARMA CO (upper right), GALEX FUV (lower left) and WISE 22 μ m (lower right) maps for NGC3607 in the ATLAS^{3D} sample. All maps are convolved to 13 arcsec resolution. The blue ellipses and red circles indicate the aperture derived from CO(1-0) map and the half-light radius R_e in K-band taken from Cappellari et al. (2011). The green bar shows the physical scale of 1kpc in each map.

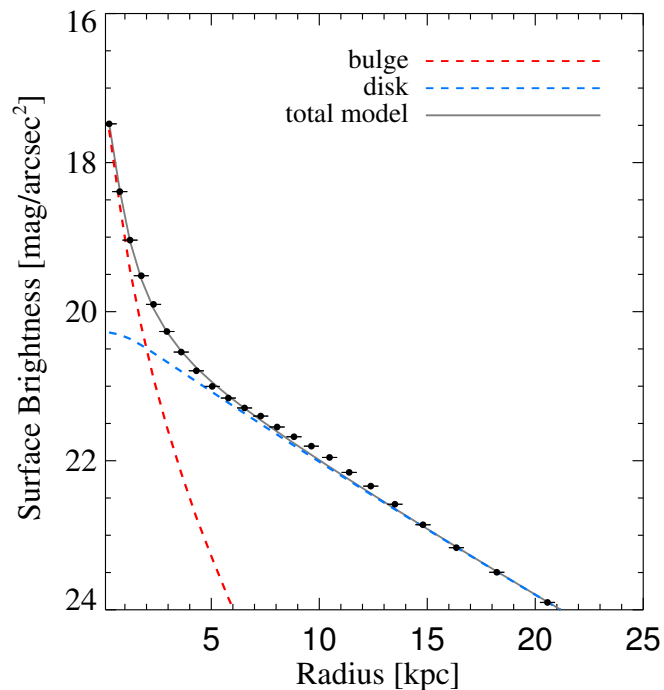


Figure 4.3: An example of a one-dimensional decomposition profile for a galaxy in the HERACLES sample. Black points show the mean surface brightness of the g-band image in elliptical annuli with the axial ratio and position angle drawn from the disc model. The grey line denotes the total model flux. The red and blue dashed lines denote the model fluxes for the bulge and the disc.

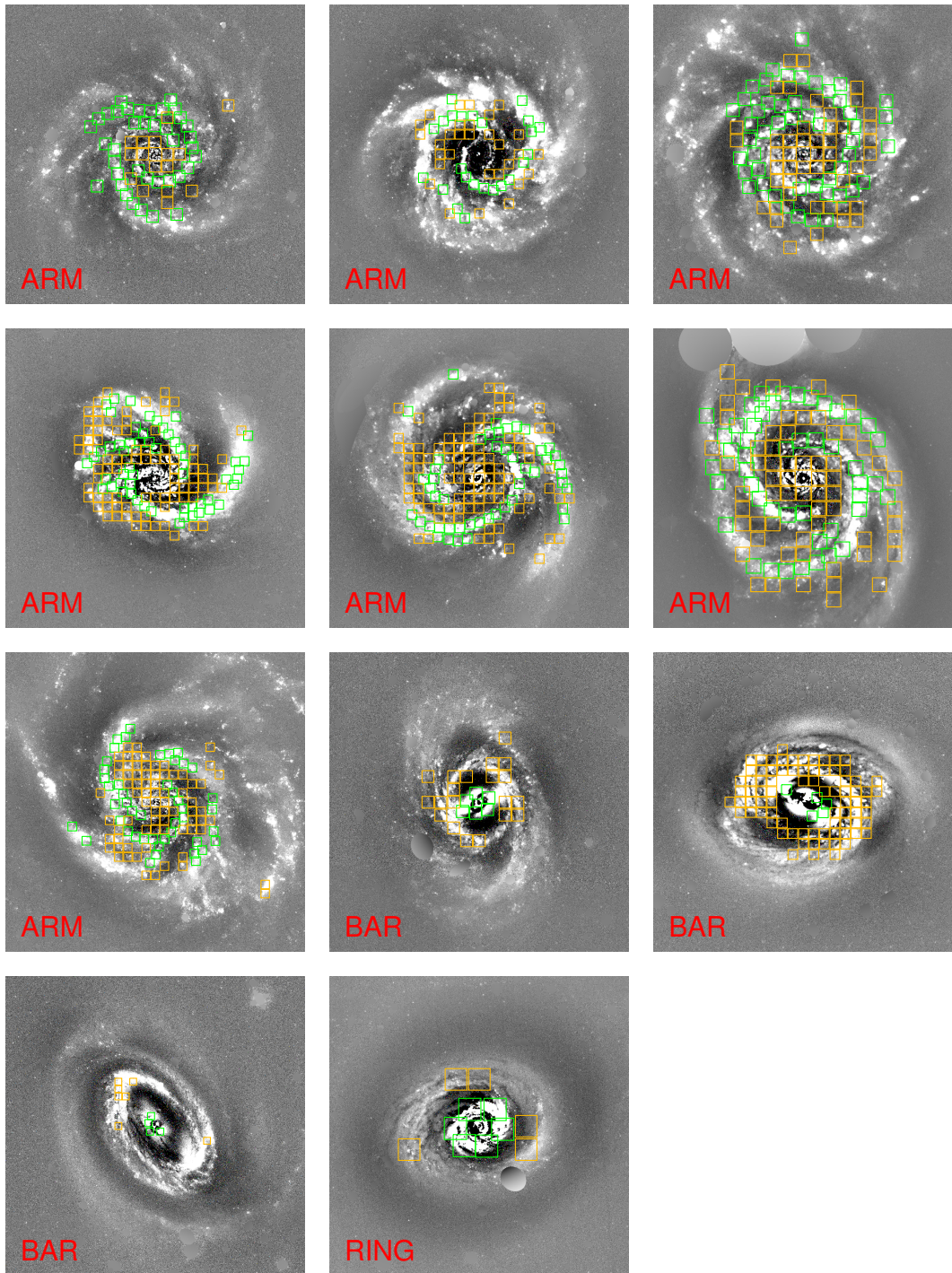


Figure 4.4: SDSS g-band residual maps for HERACLES galaxies with grand-design spiral arms, bars and rings. Coloured squares show grids of 1-kpc^2 size in the area of the targeted structure (green) and in the rest of the galaxy (yellow) . Note that we only show the grids that lie above the gas and SFR sensitivity limits.

4.3 Methods

Molecular gas depletion time is defined as $\Sigma_{\text{H}_2}/\Sigma_{\text{SFR}}$ or $M_{\text{H}_2}/\text{SFR}$, where Σ_{H_2} and Σ_{SFR} are molecular gas and SFR surface densities, and M_{H_2} is molecular gas mass. Specific SFR (sSFR) is defined as SFR/M_* or $\Sigma_{\text{SFR}}/\Sigma_*$, where Σ_* is stellar mass surface density. We use the first definition for the spatially-resolved HERACLES sample; the second definition is used for the ATLAS^{3D} and COLD GASS samples to derive an integrated depletion time and sSFR.

4.3.1 Overview of the spatial scales probed by the observations

For the HERACLES sample, the spatial resolution of the CO maps is $\sim 13''$, which is $\leq 1\text{kpc}$. The GALEX FUV and Spitzer $24\mu\text{m}$ maps have better resolution, so we degrade them to the same resolution as the CO maps. The sizes of structures we want to study, such as bulges, arms, bars and rings, are well-resolved with 1kpc smoothing. We therefore use $1\text{kpc} \times 1\text{kpc}$ grid cells as our sampling elements.

ATLAS^{3D} includes a subset of ~ 40 ETGs with resolved CO maps and supplements data for bulge regions. Given that the size of the CO-emitting regions is only a few kpc or even smaller and that the gas surface density sensitivity limit varies from one galaxy to another for the ATLAS^{3D} project, we do not derive the depletion time within 1kpc^2 grids, but within the CO-emitting region. We first smooth CO maps to the same $13''$ resolution as the WISE image. We run SExtractor on the CO moment0 maps and use the Kron aperture as the size of CO-emitting region. The CO flux within the Kron aperture is converted to the molecular gas mass by applying a Galactic CO-to-H₂ conversion factor. We note that we measure the SFR and the stellar mass using the same aperture as the CO emission. An example of our multi-band images with the aperture derived from the CO map is shown in Figure 4.2.

The CO emission for the COLD GASS galaxies is observed within the IRAM $22''$ Gaussian beam. Once again, SFR must be measured within the same region where molecular gas is observed; thus, we derive SFR for the COLD GASS galaxies by placing a $22''$ Gaussian beam on the FUV and $24\mu\text{m}$ maps. As pointed out in the previous chapter, the depletion timescales that we derive for the COLD GASS galaxies agree better with the HERACLES results than those in Saintonge et al (2011b).

4.3.2 Identification of bulges/arms/bars/rings

In this section, we fit Sérsic models to SDSS g-band images and identify bars/rings/spiral arms from the residual images. After the main features of galaxies, i.e. the bulge and the disc, are removed, the residual maps can reveal fine structures such as rings or arms more clearly.

We first mask stars and background galaxies in the SDSS images using the colour-based masks as before. We inspect the images again and mask stars by hand when necessary. The masked regions are marked as bad pixels which will not be used for fitting. The maps of Schlegel et al. (1998) are used to correct for Galactic extinction. We next apply a two-dimensional image decomposition program called GALFIT (Peng et al. 2002) to the SDSS g-band images to decompose galaxies into bulges and disks. To fit the luminosity profile of the galaxies, the code assumes a two-component model, Sérsic bulge plus Sérsic disk profile, where the Sérsic n values for the bulge and disk are allowed to vary from 1.5 to 4 and from 0.8 to 1.2, respectively. The grids within the effective radius of the bulge model are designated as the bulge grids. One example of the fitting result is shown in Figure 4.3. The surface brightness profile of the galaxy is clearly separated into two components. The effective radii of the bulge and disc are 0.8 and 8.0 kpc.

We identify seven galaxies with large arms, three barred galaxies, and one galaxy with a ring from the residual maps. We visually select grids within the arm, bar and ring regions. Examples are shown in Figure 4.4. Note that we exclude those grids with Σ_{H_2} below the CO detection sensitivity limit or $\Sigma_{\text{SFR}} < 10^{-3} \text{ M}_{\odot} \text{ yr}^{-1} \text{ kpc}^{-2}$, because the SFR calibration does not work for these low values (see Section 4.3.4). As can be seen, we are able to sample between 50 – 100 grid cells for each galaxy, with the exception of some of the barred galaxies and the ring galaxy. The reason why there are only a few grids on these galaxies is that their Σ_{H_2} values are generally low and thus many grids are discarded.

4.3.3 Derivation of M_{H_2} or Σ_{H_2}

For the resolved HERACLES maps, molecular gas depletion time is defined as $\Sigma_{\text{H}_2}/\Sigma_{\text{SFR}}$. We calculate the molecular gas depletion time in 1-kpc \times 1-kpc grid cells. The fluxes from the reduced HERACLES CO maps are converted to Σ_{H_2} in each 1-kpc grid cell adopting the Galactic CO-to-H₂ conversion factor, $4.35 \text{ M}_{\odot} \text{ pc}^{-2} (\text{K km s}^{-1})^{-1}$. Note that we discard the bins with $\Sigma_{\text{H}_2} < 3 \text{ M}_{\odot} \text{ pc}^{-2}$, which is the sensitivity limit for the HERACLES CO maps.

For the COLD GASS galaxies, the observed CO fluxes in the catalog of Saintonge et al. (2011b) are converted to the molecular gas mass. For ATLAS^{3D}, the CO flux within

the Kron aperture is converted to the molecular gas mass. In both cases, the Galactic CO-to-H₂ conversion factor is used.

4.3.4 Derivation of SFRs or Σ_{SFR}

We estimate SFR by combining the FUV and IR data. FUV traces the emission from unobscured massive stars formed over the past $\sim 100 \text{ Myr}$. UV photons absorbed by the surrounding dust cause emission at IR wavelengths. The linear combination of the FUV and IR emission can recover both the unobscured stellar emission and the dust-reprocessed emission.

HERACLES

We use the FUV and $24 \mu\text{m}$ images to estimate Σ_{SFR} . The same method applied to the optical images is used to mask stars and background galaxies. We re-fill the masked region with the local background. We correct the FUV images for Galactic extinction using the maps of Schlegel et al. (1998). All the images are convolved to a resolution of Gaussian $13''$ using the kernels released in Aniano et al. (2011).

Next we apply the method suggested in section 8.2 of Leroy et al. (2012) to remove the cirrus contribution originating from evolved stellar populations. A first-order correction is done using the total gas surface density, i.e. the sum of Σ_{H_2} and Σ_{HI} , where Σ_{HI} is obtained from THINGS data. After we remove this cirrus emission from the $24 \mu\text{m}$ emission, we then adopt the updated calibration coefficient in Leroy et al. (2012) to calculate the SFRs from the linear combination of the FUV and $24 \mu\text{m}$ luminosities. Those bins with $\Sigma_{\text{SFR}} < 10^{-3} M_{\odot} \text{ yr}^{-1} \text{ kpc}^{-2}$ are excluded in the following analysis, because the SFR calibration becomes poor in the very low SFR regime.

ATLAS^{3D}

Figure 4.5: Relation between K-band absolute magnitude and WISE $22 \mu\text{m}$ luminosity. Black and magenta solid points are the galaxies without and with CO detections from the ATLAS^{3D} sample. Only galaxies with $22 \mu\text{m}$ flux S/N > 3 are shown. The black solid line is the best-fit linear regression to the CO non-detected galaxies. The blue plus symbols represent galaxies excluded during the fitting process (see text).

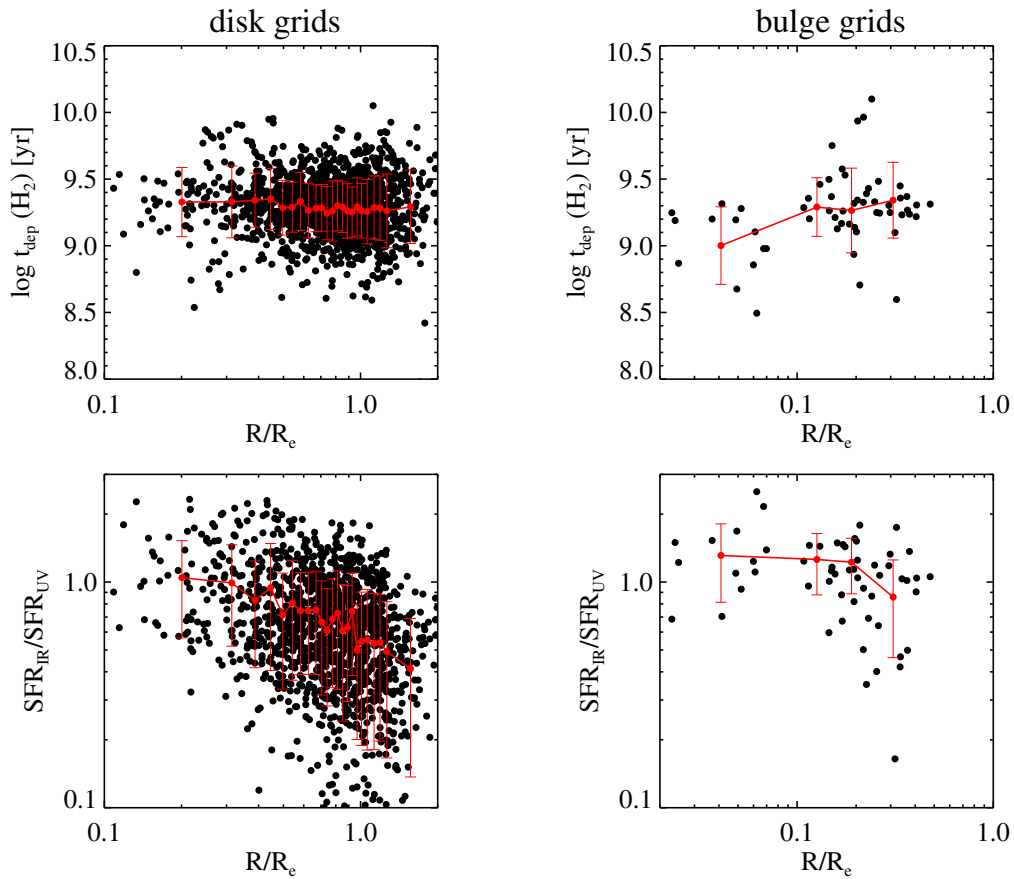


Figure 4.6: Molecular gas depletion time (upper panel) and the IR/UV ratio (lower panel) as a function of radius for disc and bulge grids of HERACLES sample. The radius is normalized to the effective radius of the disc, R_e .

We use the FUV and $22\mu\text{m}$ images to estimate SFRs within the aperture derived from the CO maps. Both the GALEX FUV and WISE $22\mu\text{m}$ images are convolved to $13''$ resolution. The steps to process FUV and WISE $22\mu\text{m}$ images including star/background galaxy masking, sky removal, Galactic foreground extinction correction and WISE color correction, are the same as described in the previous chapter.

As the ATLAS^{3D} galaxies are ETGs, the contribution from old stellar populations to the IR emission is significant (e.g., Kennicutt 1998). Davis et al. (2014) estimate that the average fractional contribution from evolved stars to the $22\mu\text{m}$ luminosities of ETGs is $\sim 25\%$. These authors found a tight correlation between K-band and $22\mu\text{m}$ luminosities for a subset of galaxies without CO detections and used this relation to correct the total $22\mu\text{m}$ emission for the contribution from old stars.

We retrieve 2MASS K-band Atlas images from the NASA/IPAC Infrared Science Archive for both CO-rich and CO non-detected galaxies from the ATLAS^{3D} survey. To remove stars or background galaxies, we run SExtractor and mask detected sources, with the exception of the central galaxies. We estimate the sky background as the median value of the pixels with values $< 3\sigma$ above the median value of the whole image. The K-band images are then convolved to the same $13''$ resolution as the WISE $22\mu\text{m}$ images. We derive K-band and $22\mu\text{m}$ luminosities for the whole galaxy using the Kron aperture in SExtractor.

The K-band absolute magnitude is plotted against $22\mu\text{m}$ luminosity for CO-rich and CO non-detected ETGs in Figure 4.5. As can be seen, the K-band absolute magnitude correlates well with the $22\mu\text{m}$ luminosity for CO non-detected galaxies (black points), while there is no clear relation for the CO-rich galaxies (magenta points). We perform a linear fit to the CO non-detected galaxies and plot the result with a black solid line in Figure 4.5. The best-fit is given by

$$\log\left(\frac{L_{22\mu\text{m}, \text{old stars}}}{\text{ergs}^{-1}}\right) = (-0.38 \pm 0.01) \times M_k + (32.38 \pm 0.34). \quad (4.1)$$

Note that there are 5 outliers (blue plus signs in Figure 4.5) with scatter larger than 0.5 dex. They include one galaxy with apparent spiral arms, one with a star-forming ring, one with a high HI mass fraction, and two with either a star or small galaxy nearby. We exclude these galaxies from our fits.

We measure the K-band magnitudes of CO-rich ETGs within the aperture derived from CO maps, estimate the $22\mu\text{m}$ luminosity from old stars using Equation (4.1), and subtract this from the total $22\mu\text{m}$ emission. We then scale the WISE $22\mu\text{m}$ fluxes so that they have the same normalization as the MIPS $24\mu\text{m}$ fluxes (see the previous chapter). We convert the FUV and $22\mu\text{m}$ luminosities to SFRs using the same calibration given in Leroy et al.

(2012). ¹

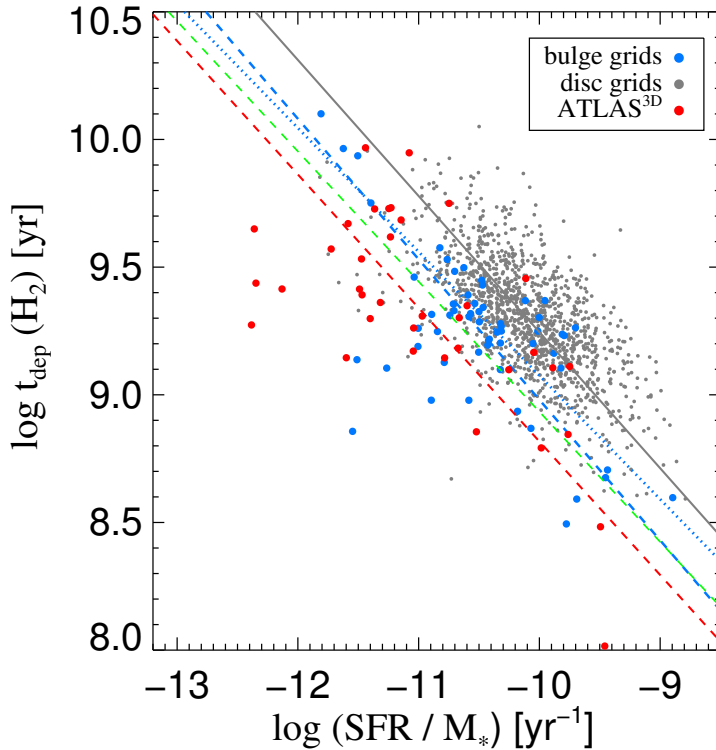


Figure 4.7: t_{dep} — sSFR relation for the bulge and disc grids of the HERACLES sample, as well as the ATLAS^{3D} galaxies. Grey and blue solid points show grids in the disc and bulge regions of the HERACLES galaxies. Red solid points show the ATLAS^{3D} sample. OLS bisector fits to the disc, bulge and ATLAS^{3D} data points are shown as grey, blue, and red dashed lines. The blue dotted line shows the OLS bisector fit to the bulge grids, excluding those with $R < 0.1R_e$. The green dashed line is the OLS bisector fit to the HERACLES bulge data points plus the results from the ATLAS^{3D} sample.

COLD GASS

As in the previous section, we use GALEX FUV and WISE 22 μm images to estimate SFR for COLD GASS galaxies within the central 22'' region. The procedure is the same as

¹We note that the local calibrations may not be applicable to global conditions (Calzetti et al. 2013), so we also try the calibration formula given in Hao et al. (2011) which is derived for the whole galaxy. We find that this makes little difference to our results.

mentioned above. For consistency, we use the same calibration as we apply to HERACLES and ATLAS^{3D} sample to convert FUV plus 22 μm into SFR.

4.3.5 Derivation of stellar mass

Stellar mass is derived using the SED-fitting method in Wang et al. (2011) by which the stellar population synthesis models of Bruzual & Charlot (2003) are fit to SDSS 5-band magnitudes. The parameter, sSFR, is the SFR divided by the stellar mass.

4.4 Results

4.4.1 The effect of internal structures on molecular gas depletion time

Bulges and discs

We plot the depletion time and the ratio of $\text{SFR}_{22\mu\text{m}}$ to SFR_{FUV} (IR/UV) as a function of radius for bulge and disc grids in Figure 4.6. Whereas the depletion time of the bulge grids drops towards the center of the galaxy, the depletion time of the disc grids remains almost constant as a function of radius. In contrast, the IR/UV ratios of the disc and bulge grids decline from the center towards the outskirts – this is not surprising because the IR/UV ratio is a robust indicator of dust attenuation, and the outer parts of galaxies are expected to have lower metallicities and dust content. We note that the fact that different radial trends are found for depletion time and for IR/UV ratio make it seem unlikely that variations in CO-to-H₂ conversion factor are responsible for the drop in the depletion time in the central bulge. We note that this result is consistent with results presented in Leroy et al. (2013). (see Section 4.5 for further discussion).

In Figure 4.7, we investigate the $t_{\text{dep}} - \text{sSFR}$ relation for bulges (blue solid points) and discs (grey solid points) regions. We also plot the ATLAS^{3D} bulge-dominated sample for comparison (red solid points). We perform OLS-bisector fits to the data and plot the fitting results in Figure 4.7 as well. There are two obvious results: First, the scatter in depletion time is larger in bulges than in discs (0.33 dex in $\log t_{\text{dep}}$, compared to 0.22 for discs). Excluding bulge grids with $R < 0.1 R_e$, which may be influenced by AGN , makes no difference to this conclusion. Second, in the bulge, t_{dep} is systematically shifted to smaller values at a given sSFR compared to the disc grids. We note that there are some bulge grids whose depletion times lie above the grey line derived for disc grids in Figure 4.7. We check the location of these grids and find that they are generally in the outer region of the

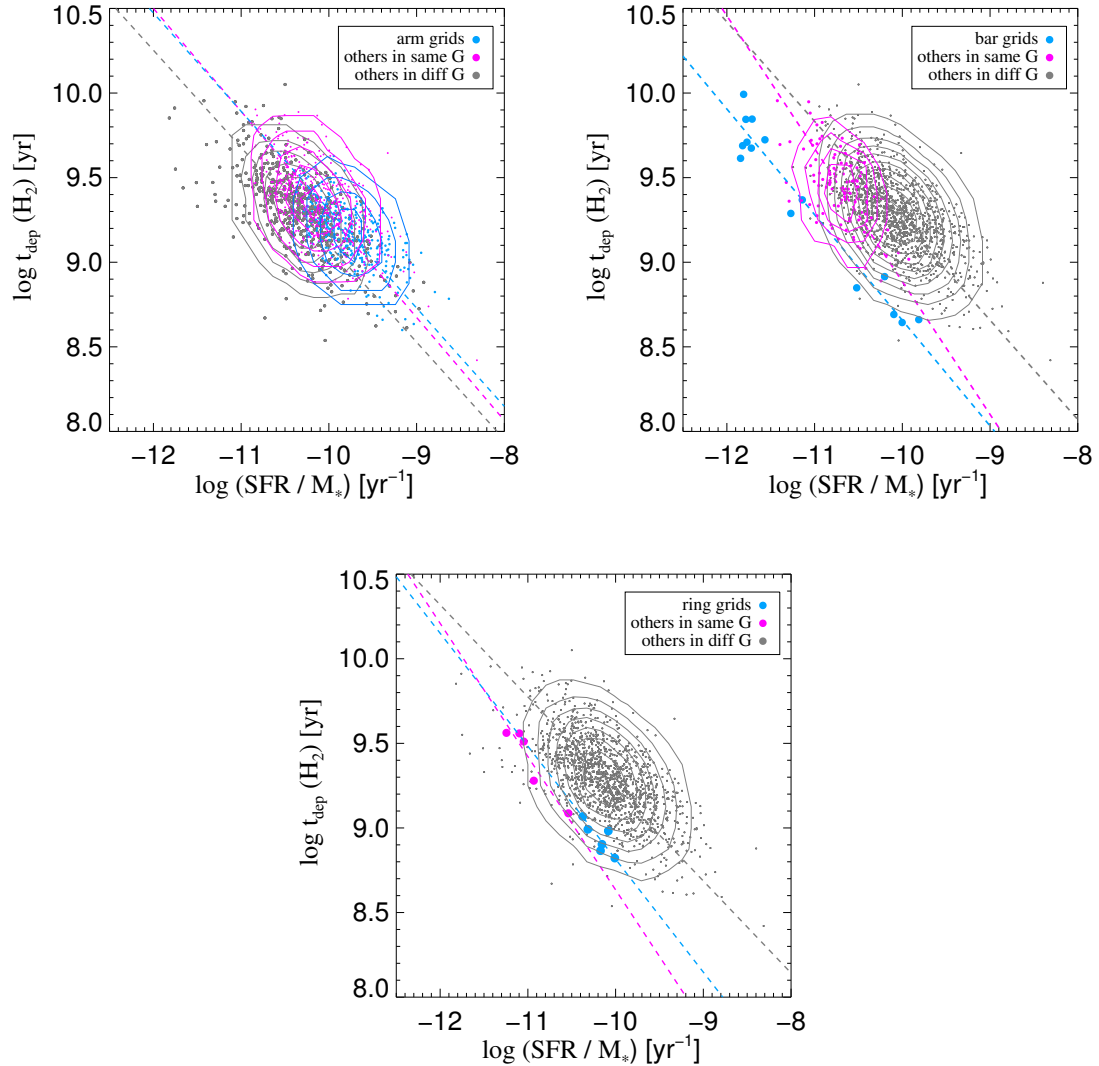


Figure 4.8: Distribution in the t_{dep} – sSFR plane of grids in galaxies with spiral arms (upper left), in galaxies with bars (upper right) and in galaxies with rings (bottom). Results for grids within the arm, bar or ring regions are coloured in blue. Results for grids in these galaxies outside the arms, bars or rings are coloured in magenta. Results for grids in galaxies without arms, bars or rings are coloured in grey. OLS-bisector fits to the data points in these different groups are shown with the same color.

bulge.

Spiral arms, bars and rings

In Figure 4.8, we plot the $t_{\text{dep}} - \text{sSFR}$ relation for galaxies with grand-design arms, bars and rings. Magenta points denote the grids located within the region of the targeted structure, such as the grand-design arm, bar or ring; blue points denote other grids in the same galaxies. Grids from other galaxies, i.e. those galaxies that do not contain the designated structure, are shown in grey.

The sSFRs in the ISM of galaxies with grand-design arms are higher than in galaxies without arms, and the sSFRs within the arms themselves are the highest. This is expected, because gas is compressed by spiral density waves and star formation rate scales with gas surface density. Interestingly, t_{dep} is shifted to higher values at a given sSFR in galaxies with spiral arms. We apply OLS-bisector fits to the spiral arm data and the results are shown as dashed lines in Figure 4.8. Indeed, the grids in the regions with (blue dashed line) or without (magenta dashed line) arms are systematically shifted to longer t_{dep} at fixed sSFR compared to the grey dashed line, which is for galaxies without spiral structure.

In barred galaxies, we find the opposite trend. The sSFRs in the interstellar medium of galaxies with bars (magenta points in the middle panel) are much lower than in galaxies without bars. Bars are long-lived structures. Although they can act to channel gas towards the center of a galaxy and fuel starbursts, this is a transient phenomenon and the majority of present-day barred galaxies are relatively quiescent. The OLS-bisector fit to the grids in barred galaxies indicates that t_{dep} is shortened at fixed sSFR compared to grids from galaxies without bars. This is exactly the opposite to what was found for galaxies with spiral arms. There is only one galaxy with a ring in HERACLES sample, so we only have a few grids available for analysis. Based on the limited data, we conclude that ringed galaxies follow the same trends as barred galaxies.

4.4.2 Linking the results together

So far, we have analyzed molecular gas depletion time variations in terms of location within or outside specific structures of the galaxy, such as bulges, bars, arms or rings. We now ask whether all of these variations can be linked to a physical parameter that varies continuously within galaxies. For example, Daddi et al. (2010) and Genzel et al. (2010) proposed that the combination of high gas density and short dynamical timescale could explain the short global molecular gas consumption timescales in strongly starbursting galaxies. The parameters that we examine in this section are, 1) IR/UV ratio as a proxy

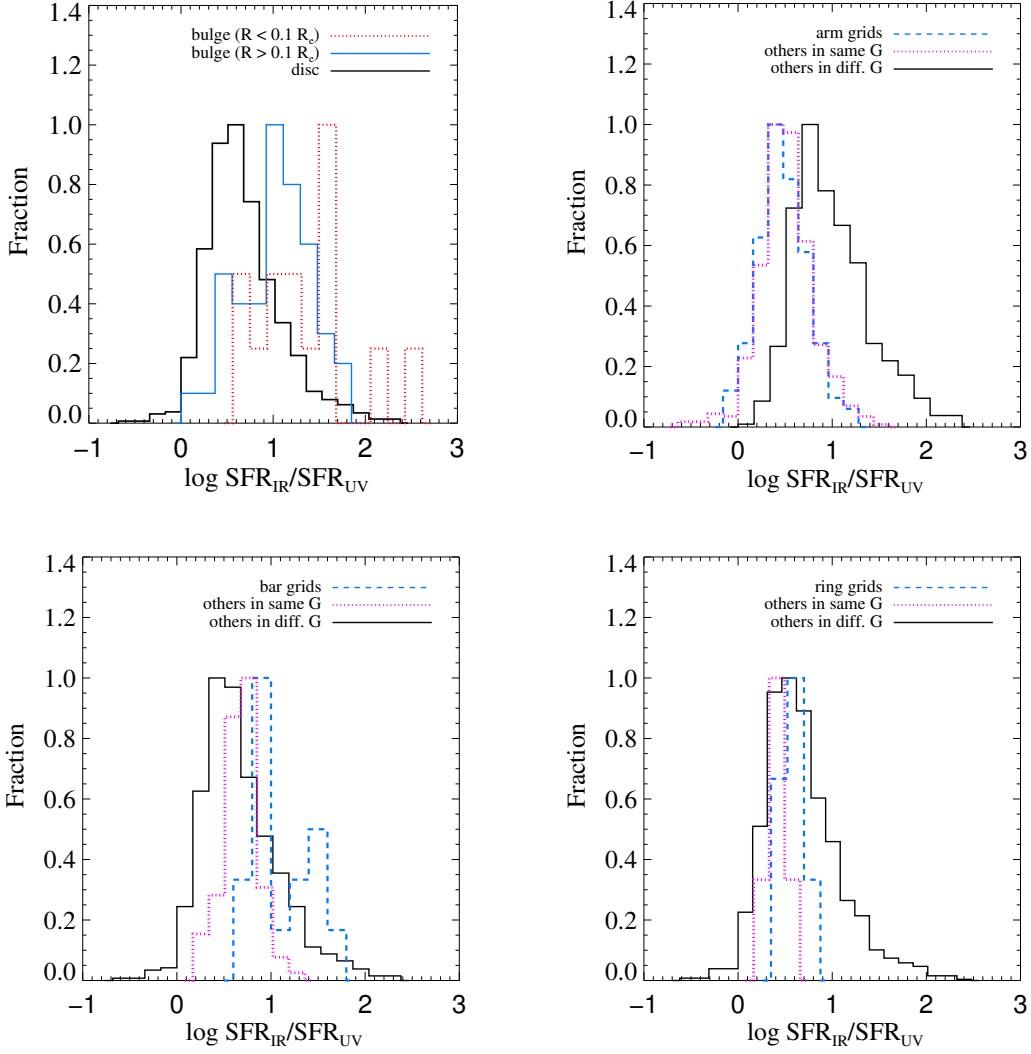


Figure 4.9: Distribution of the ratio of $SFR_{22\mu m}$ to SFR_{FUV} . In the upper left panel, red dashed and blue histograms show results for grids in the bulge regions with $R < 0.1R_e$ and $R > 0.1R_e$ respectively. The black histogram is for the grids in the disc regions. In the other panels, blue histograms are for grids within the structure (arm or bar or ring); magenta histograms are for the grids outside the structure; black histograms are for the grids from the other galaxies in the HERACLES sample. Upper right panel: the spiral-arm galaxies. Lower left and right panels: the barred and ring galaxies.

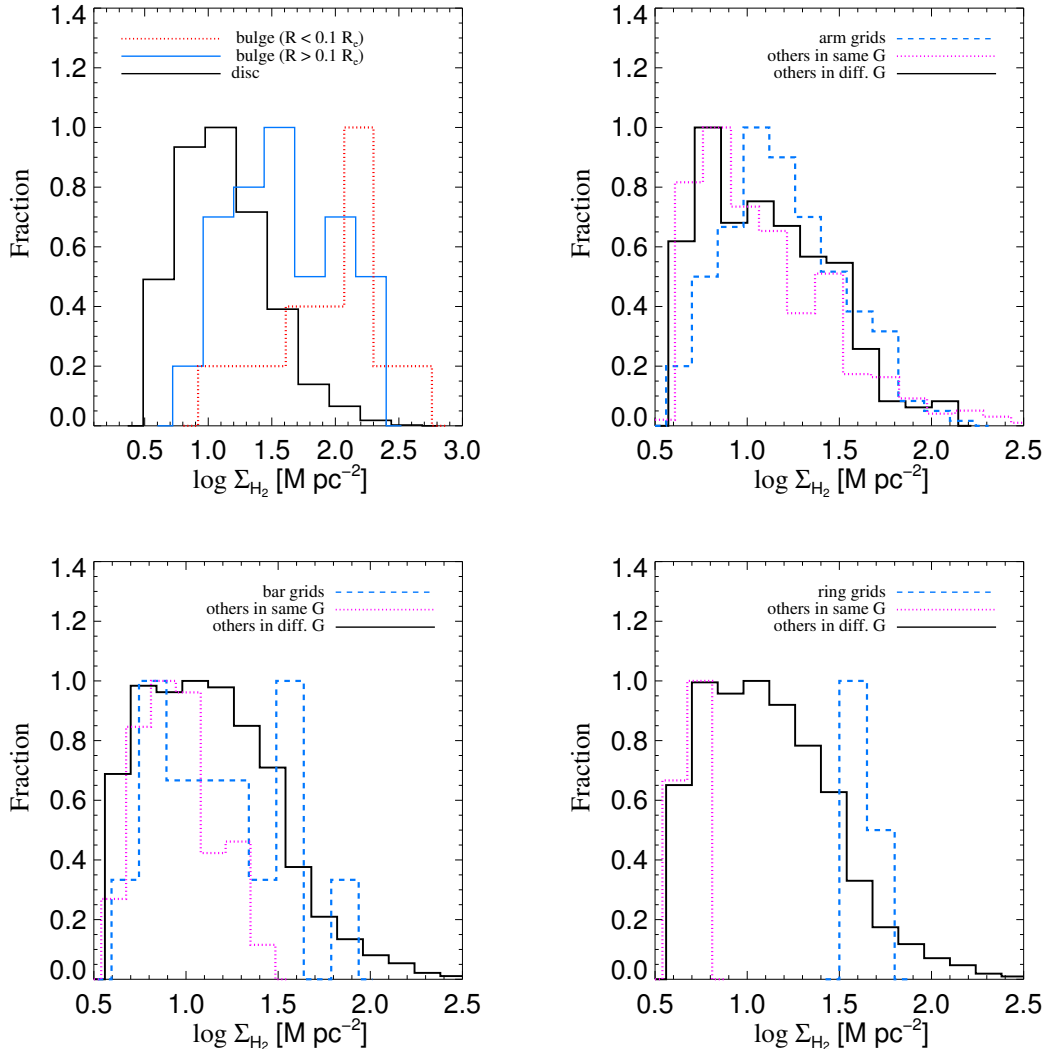


Figure 4.10: Distribution of the molecular gas surface densities. Conventions and lines are as in Figure 4.9.

for dust content, 2) H₂ surface density, 3) stellar surface density.

IR/UV ratio In Figure 4.9, we plot the distributions of IR/UV ratios for inner bulge, outer bulge and disk grids in the top left panel. In the top right panel, we plot distributions for spiral arm, inter-arm and control grids. The bottom two panels are the same as the top right panel, except that results are shown for bars and rings.

As we have seen previously, IR/UV ratios are highest in the inner regions of bulges, from which we infer that these are the dustiest regions of nearby galaxies. The high dust content in the centers of bulges means that it is unlikely that we have under-estimated the H₂ content on the galaxy by using the Galactic CO-to-H₂ conversion factor. The short depletion times observed in central bulges are thus not likely to be an artifact of wrongly estimated molecular gas masses. The least dusty regions of the ISM are found within galaxies with grand-design spiral arms. By a similar argument, we infer that that higher molecular gas depletion times observed in these regions are not likely to be an artifact of conversion factor variations either.

Grids within bars in barred galaxies have similar IR/UV ratio as the outer parts of galactic bulges, while those outside bars have IR/UV ratios similar to the general disc population. Grid within rings appear less dusty than grids within bars, but we caution that our sample consistent of only one ringed system.

In summary, we deem it unlikely that variations in CO-to-H₂ conversion factor are responsible for the different $t_{\text{dep}} - \text{ssSFR}$ relations among grid cells lying within different structures.

H₂ surface density Figure 4.10 is the same as Figure 4.9, except that distributions of H₂ surface density are shown. If we exclude the single ringed galaxy, the only significant shift in H₂ surface density occurs within bulges, which have molecular gas densities up to a factor of 30 higher than discs, particularly in their inner regions. The enhancement in gas density in the grids with spiral arms is only about 50%, and grids that lie outside spiral arms have H₂ densities that are identical to grids with galaxies without arms. Gas density is enhanced more strongly within bars, but still not as strongly as in bulges.

In conclusion, although high gas densities may be a promising avenue for explaining the short depletion time in bulges and starburst systems, it does not appear to vary in a systematic way in other environments such as spiral arms and bars, so as to explain other observed trends. We will demonstrate this in more detail later in this section.

Stellar surface density In Figure 4.11, we plot the distributions of stellar surface density for the grids within different structures. In this case, there is a very clear separation between grid cells in bulges, bars and rings, which peak at $\log \Sigma_* \sim 3 \text{ M}_\odot \text{ pc}^{-2}$ while grids in the spiral-arm galaxies peak at $\log \Sigma_* \sim 1.5 - 2 \text{ M}_\odot \text{ pc}^{-2}$. Grids in the inner regions of

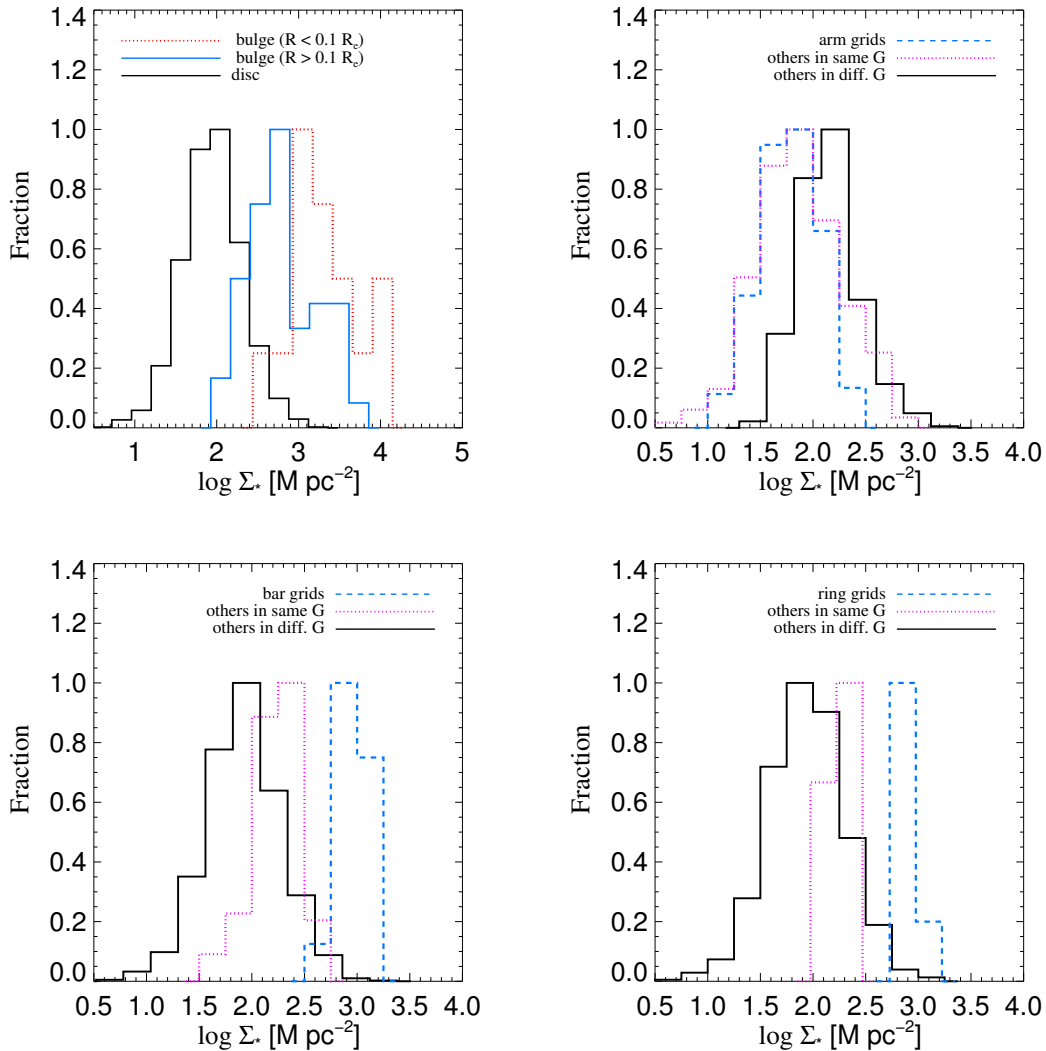


Figure 4.11: Distribution of the stellar surface densities. Conventions and lines are as in Figure 4.9.

bulges, where t_{dep} is shortest, are shifted to even higher Σ_* than the outer bulges. Spiral arm and inter-arm grids also peak at lower Σ_* values than grids from galaxies without spiral arms. In summary, variations in the Σ_* distributions between different galaxy structures mirror the variations in the $t_{\text{dep}}-\text{sSFR}$ relations described in the previous section extremely well.

We now fit a linear relation to the $t_{\text{dep}}-\text{sSFR}$ relation for all grid data points and plot the residuals against Σ_* , Σ_{H_2} and a third quantity, the interstellar pressure, in Figure 4.12. Following Leroy et al. (2008), the pressure, P_h , is expressed as

$$P_h \approx \frac{\pi}{2} G \Sigma_{\text{gas}} (\Sigma_{\text{gas}} + \frac{\sigma_g}{\sigma_{*,z}} \Sigma_*), \quad (4.2)$$

where σ_g and $\sigma_{*,z}$ are velocity dispersions of gas and stars, and Σ_{gas} and Σ_* are the gas and stellar surface densities.

Figure 4.12 shows that Σ_* is the only quantity that clearly correlates with Δt_{dep} . Grids in bulges, bars, and rings and the ATLAS^{3D} sample clearly separate from the spiral arm, inter-arm and disc grids in this plot. We can also understand the reason why we did not observe a correlation between Δt_{dep} and Σ_* for the COLD GASS sample previously : the dynamic range in Σ_* of the COLD GASS sample is too small. The integrated stellar surface densities of the COLD GASS sample span only 1 dex on the x-axis.

Motivated by these results, we fit a plane to the two-dimensional relation between the depletion time, specific star formation rate and the stellar surface density. Following the method in Bernardi et al. (2003), we find the best-fit linear correlation of the form

$$\log t_{\text{dep}} = a \log(\text{sSFR}) + b \log(\Sigma_*) + c \quad (4.3)$$

We plot all the data, including the grids from HERACLES, the ATLAS^{3D} sample and the COLD GASS sample in Figure 4.13, and we show the $t_{\text{dep}}-\text{sSFR}$ relation in the next panel for comparison. The 1:1 relation is shown by a black solid line. The values of the coefficients, a , b , and c from the best-fit result are -0.36 , -0.14 , and 5.87 respectively. The Pearson linear correlation coefficient r between the x and y axes is 0.68 , and the scatter in t_{dep} about the plane is 0.18 dex. The reduction in scatter, compared to the one-dimensional relation for t_{dep} versus sSFR, which has a scatter of 0.19 , is only 5% . This is because our sample is heavily dominated by the number of grids from the disc-dominated regions of galaxies. The main effect of the two-parameter fit is to bring the outlying points, which are mainly from bulge and bar grid cells, into better agreement with the rest of the sample.

Finally, we note that for 1 kpc^2 grid cells, we can rewrite equation (4.3) above as

$$\log t_{\text{dep}} = a \log(\Sigma_{\text{SFR}}) + (b - a) \log(\Sigma_*) + c \quad (4.4)$$

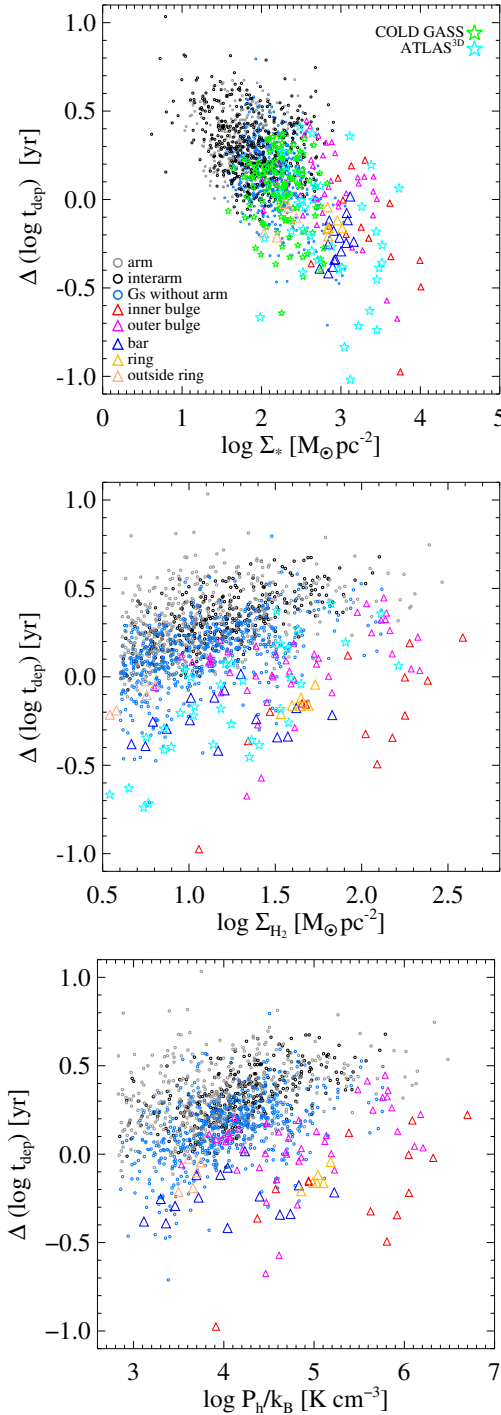


Figure 4.12: Residuals from the $t_{\text{dep}} - \text{sSFR}$ relation as a function of Σ_* (top panel), Σ_{H_2} (middle panel), and midplane gas pressure (bottom panel). Grey and black circles are the grids in and outside the arm regions of the spiral galaxies from HERACLES. Light blue circles denote grids from galaxies without spiral-arms. Blue and yellow triangles denote the grids in the bars and the ring. Beige triangles denote the grids from the ring galaxy but outside the ring region. Cyan and green stars represent the ATLAS^{3D} and COLD GASS sample respectively.

This shows that the surface density of young stars in a grid cell contributes ~ 1.6 times more weight to our prediction of depletion time than the surface density of evolved stars.

4.5 Summary and discussion

Using the resolved maps of the nearby HERACLES galaxies, we have calculated the molecular gas depletion time in $1\text{-kpc} \times 1\text{-kpc}$ grid cells and studied the $t_{\text{dep}} - \text{sSFR}$ relation for grids lying within different galaxy structures such as bulges, arms, bars, and rings.

Our main results can be summarized as follows:

- (i) Bulge regions have shorter gas depletion times than the disk regions at a given value of the sSFR. This effect is strongest in the central regions of the bulge.
- (ii) The $t_{\text{dep}} - \text{sSFR}$ relation for the grid cells in spiral-arm galaxies shifts to longer t_{dep} at fixed sSFR compared to grid cells from galaxies without spiral arms. Note that this shift applies to *all grid cells* from spiral arm galaxies. Within a spiral arm, the sSFR values are higher than in the inter-arm region, so the average depletion times will be shorter.
- (iii) Grid cells located within bars have reduced depletion time at fixed sSFR. Grids located in barred galaxies outside of the barred region occupy a narrow range of low sSFR values.
- (iv) We identify the stellar surface density Σ_* as the parameter that can best predict the shifts between the relations found for bulges, bars and spiral arms.

Our results on star formation efficiencies in spiral arms are largely consistent with those presented in Figure 7 of Foyle et al. (2010) and Figure 13 of Rebolledo et al. (2013) even though our methodology for identifying spiral arms differs from these papers. Several previous papers have claimed that star formation efficiencies in bars are low (e.g., Reynaud & Downes 1998; Momose et al. 2010; Sorai et al. 2012). We note that in our sample, the molecular gas depletion time in barred regions spans a range of more than a factor of 10. Only in bars with high gas densities do we find grid cells with short depletion times and high SFEs. This is consistent with the work of Sheth et al. (2005), who find that barred spiral galaxies generally have higher molecular gas concentrations in their central regions. However, barred galaxies exist that have no molecular gas detected in the nuclear region and very little within the bar corotation radius. Bars are long-lives, and we likely observe them at different evolutionary stages, which explains why the SFE has such a large spread.

Our result that bulge grids have reduced depletion time compared to disc grids is consistent with results presented in Leroy et al. (2013). These authors studied radial trends in molecular gas depletion time as a function of radius and observed that the average t_{dep} was smaller in the central $\sim 1\text{kpc}$ regions. The reduced depletion time was even more

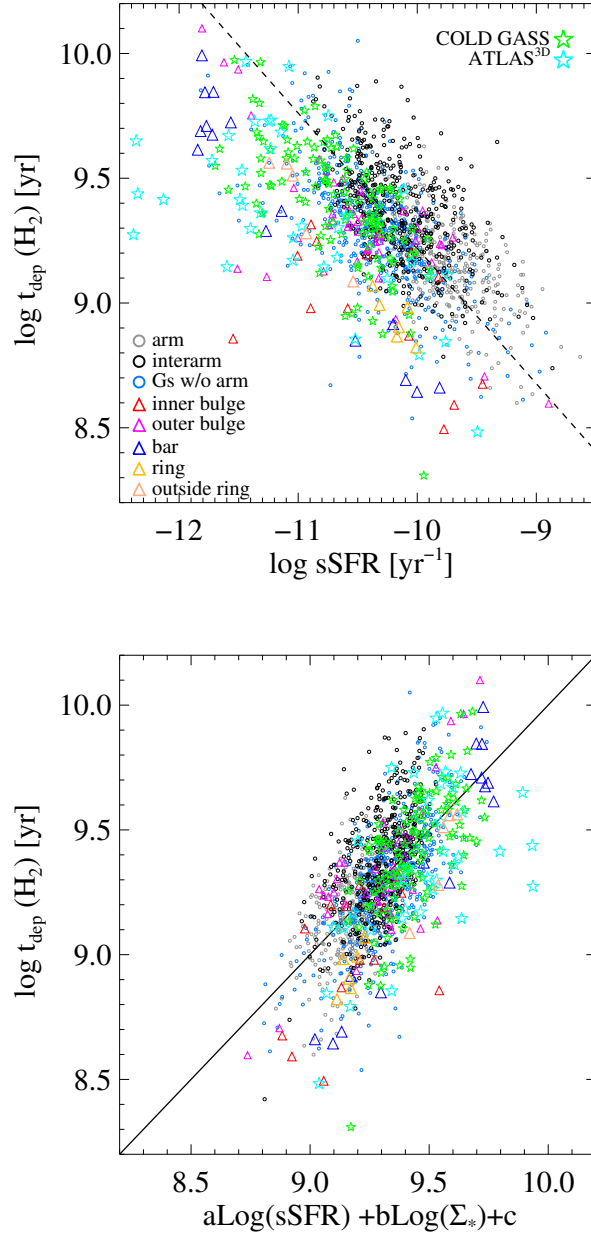


Figure 4.13: Top panel: t_{dep} – sSFR relation for all grids of the HERACLES sample, ATLAS^{3D} galaxies, and the COLD GASS galaxies. Grey and black circles are the grids in and outside the arm regions of the spiral galaxies from HERACLES. Light blue circle denote grids from galaxies without spiral-arms. Blue and yellow triangles denote the grids in bars and rings. Beige triangles denote the grids from the ring galaxy but outside the ring region. Cyan and green stars represent the ATLAS^{3D} and COLD GASS sample separately. We show the OLS bisector fit to all grid data from the HERACLES sample with a black dashed line. Bottom panel: The best-fit plane linking t_{dep} , ssfr, and Σ_* . Symbols are as in the left plot. The best-fit coefficients, a , b , c , are -0.36 , $+0.22$, 5.87 respectively.

pronounced after they applied a CO-to-H₂ conversion factor that depended on dust-to-gas ratio. Once again, these authors did not study trends of depletion time at fixed specific star formation rate.

We note that Davis et al. (2014) found that star formation efficiencies (SFEs) of the ETGs in ATLAS^{3D} survey were *reduced* compared to spiral galaxies. The main reason for this apparently discrepant result is the definition of star formation efficient adopted by these authors: SFE was computed as the ratio of the total (atomic+molecular) gas mass divided by the total star formation rate of the galaxy. The analysis in this study only considers the star formation efficient of the molecular gas component of the galaxy.

Why should the star formation efficiency of the molecular gas be sensitive to the local surface density of evolved stars? Helfer & Blitz (1993) studied the properties of the dense molecular gas in the bulges of a sample of 19 normal spiral galaxies. They observed the 3mm emission from the molecules HCN and CS, which traces much denser gas than CO. They found that the CS to CO ratio in the external bulges was consistent with that measured for the bulge of the Milky Way and a factor of 2 or more larger than in the Galactic disc. In subsequent work, Helfer & Blitz (1997) carried out interferometric observations of emission from the HCN molecule in NGC 6946, NGC 1068, and the Milky Way and found that the ratio of HCN to CO at the galactic centres was 5-10 times higher than in the discs of these galaxies.

Helfer & Blitz (1993) put forward two possible explanations for their findings: 1) Because the stellar potential is larger in the bulge than in the disc, the gas is subject to much higher pressures, 2) The giant molecular clouds (GMCs) have different mass and/or structure in the bulge than in the disc. Launhardt, Zylka & Mezger (2002) emphasized that most of the ISM in the central bulge of the Milky Way is likely in the form of very dense, compact clouds. These conclusions arise from the lack of a significant diffuse component in high resolution submm maps of the Galactic centre. They speculate that the physical reason for the observed clumpiness of the ISM is the tidal stability limit – clouds have to be dense enough to be stabilized against tidal forces by their own gravitation.

The results in our work suggest that there may be a *continuum* of molecular cloud properties set by the local stellar surface density. If so, this would have very interesting consequences for our understanding of galaxy evolution. Gas-to-evolved star ratios are much higher in the early Universe than they are today (Tacconi et al 2010) and star formation may likewise be proceeding in a quite different manner inside GMCs.

Chapter 5

Conclusion and outlook

In this thesis we first combine multi-wavelength data of nearby galaxies from the ultraviolet, optical, infrared to the radio and derive a variety of galaxy properties. We then study the star formation histories of nearby galaxies to quantify the recent star formation fueled by the newly-accreted gas. We also explore the relation between molecular gas and star formation of galaxies, and constrain the molecular gas depletion time with galaxy physical parameters. We summarize our main results below.

Resolved star formation histories of galaxies – *Chapter 2*

We first work on the development of principal component analysis techniques, by which we achieve much better signal-to-noise ratio for galaxy spectra. Next we create a library of model spectra by using the population synthesis code of Bruzuel & Charlot 2003, and superimposing additional bursts of star formation on to continuous star formation histories. With these novel techniques, we constrain the radial dependence of the recent SFHs of ~ 200 local galaxies with the long-slit spectroscopy data by fitting stellar population models to the combination of specific star formation rate (ssSFR), 4000 angstrom break strength and Balmer absorption lines. These three quantities jointly place strong constraints on whether the galaxy has been forming stars smoothly or episodically over the past 1-2 Gyr. Our sample also has data of global atomic and molecular gas masses, allowing to study the connection between the recent SFHs and the gas properties.

We show that the star formation histories of many disk galaxies cannot be accurately represented if their star formation rates declined exponentially with time. Many galaxies have Balmer absorption line equivalent widths that require recent short-lived episodes or bursts of star formation. Our results clearly demonstrate that the enhanced star formation at later times is not uncommon.

The fraction of galaxies that have experienced episodic rather than continuous star

formation is highest for “late-type” galaxies with low stellar masses, low surface densities, and low concentrations. In these systems, bursts occur both in the inner and in the outer regions of the galaxy. The fraction of stars formed in a single burst episode is typically around 15% of the total stellar mass in the inner regions of the galaxy and around 5% of the mass in the outer regions. When we average over the population, we find that such bursts contribute around a half of the total mass in stars formed in the last 2 Gyr.

In massive galaxies, bursts occur predominantly in the outer disk. Around a third of all massive, bulge-dominated galaxies have experienced recent star formation episodes that are fully confined to their outer ($R > 0.7R_{90}$) regions. The fraction of stars formed in bursts is only $\sim 2 - 3\%$ of the underlying stellar mass, but when we average over the population, we find that such bursts contribute nearly all the stellar mass formed in the last 2 Gyr.

Recent star formation in outer disks is strongly correlated with the global atomic gas fraction of the galaxy, but not its global molecular gas fraction. We suggest that outer episodic star formation is triggered by gas accretion “events”. Episodic star formation in the inner regions is suppressed in galaxies with large bulge-to-disk ratio. This supports the idea that inner bursts are linked to instability-driven gas inflows.

Variation in molecular gas depletion time – *Chapter 3, 4*

We re-analyze correlations between global molecular gas depletion time (t_{dep}) and galaxy parameters for nearby galaxies from the COLD GASS survey. We improve on previous work by estimating SFRs using the combination of GALEX FUV and WISE $22\mu\text{m}$ data and by deriving t_{dep} within a fixed aperture set by the beam size of gas observation. In our new study we find correlations with much smaller scatter. Dependences of the depletion time on galaxy structural parameters such as stellar surface density and concentration index are now weak or absent. We demonstrate that the *primary* global parameter correlation is between t_{dep} and sSFR; all other remaining correlations can be shown to be induced by this primary dependence. This implies that galaxies with high current-to-past-averaged star formation activity, will drain their molecular gas reservoir sooner.

We then analyze t_{dep} on 1-kpc scales in galactic disks using data from the HERACLES survey. There is remarkably good agreement between the global $t_{\text{dep}}-\text{sSFR}$ relation for the COLD GASS galaxies and that derived for 1 kpc scale grids *in disks*. This leads to the conclusion that the local molecular gas depletion time in galactic disks is dependent on the local fraction of young-to-old stars.

Our work has now eliminated the discrepancy between the global and local results from COLD GASS and HERACLES, as seen in the previous works. We show that there is no

different star formation “law” between massive, bulge-dominated early-type and less massive, disk-dominated late-type galaxies. Rather, the molecular gas depletion time mainly depends on the sSFR on both local and global scale.

Furthermore, we now find that at a given sSFR, the bulge has shorter t_{dep} than the disc. The shift to shorter depletion times is most pronounced in the inner bulge ($R < 0.1R_e$). Grids from galaxies with bars and rings are similar to those from galactic bulges in that they have reduced t_{dep} at a given sSFR. In contrast, the t_{dep} versus sSFR relation in the discs of galaxies with spiral arms is displaced to longer t_{dep} at fixed sSFR. We then show that the differences in the t_{dep} –sSFR relation for bulges, discs, arms, bars and rings can be linked to variations in *stellar*, rather than gas surface density between different structures. We have best constrained the gas depletion time of nearby galaxies with the combination of sSFR and Σ_* . Our best current predictor for t_{dep} , both globally and for 1 kpc grids, is given by $\log t_{dep} = -0.36 \log(\Sigma_{\text{SFR}}) + 0.22 \log(\Sigma_*) + 5.87$. This might be worth implementing into simulation and modelling to improve the prescription for star formation and gas.

Our works have revealed several interesting aspects of galaxy evolution. However, there are still more topics needed to further study based on our works. For example, we still have no idea how gas is exactly accreted into galaxies and how the accreted gas influences the metallicities and star formation histories on a local scale.

In the coming years, we might rely on integral field spectroscopic (IFS) surveys to make important breakthroughs in galaxy formation and evolution. The IFS technique has the potential to revolutionize our understanding of galaxies by progressing from a 1D or 2D description to a 3D perspective, allowing a more detailed physical understanding of galaxies than offered by long-slit spectroscopy or integrated-light surveys. A large IFS survey, SDSSIII-MaNGA¹, has officially started in August 2014 and aims to observe a large sample of $\sim 10,000$ galaxies with a speed of 1600 target per year. It would be great to obtain resolved gas maps for the sample drawn from large IFS surveys such as MaNGA and to study the connections between the local atomic gas content, metallicities and star formation histories.

Also, to better understand why there is a strong correlation between depletion time and sSFR, we need the IFS data to explore the star formation histories of the galaxies with the gas data. sSFR is the ratio of current SFR to stellar mass built up by the past star formation, which is a very rough proxy of star formation history. With IFS data, we can derive much more precise star formation histories for the galaxy and further investigate how the gas depletion timescale varies with the SFHs of galaxies.

¹<https://www.sdss3.org>

In the near future, new radio facilities are going to fulfill our wishes, together with the IFS surveys, such as the MaNGA project. For the atomic gas observation, the VLA telescope is being upgraded to the new Expanded VLA², which is particularly useful to spatially resolve the atomic gas distribution in galaxies and to higher redshifts. Besides, the Westerbork Synthesis Radio Telescope is going to be equipped with APERTIF (Verheijen et al. 2008), which will provide several beams on the sky and thus increase the survey speed of the telescope by a factor of 20. One of the major proposal is to observe $\sim 2 \times 10^5$ galaxies in the northern sky that overlaps with SDSS out to $z \sim 0.15$, which would be a perfect counterpart of MaNGA in the radio band. For the molecular gas, the Atacama Large Millimeter/Submillimeter Array (ALMA³) has started full-scale operation, with 66 12m antennas since 2013. Its powerful collecting ability will promise a substantial sample from the IFS surveys. In conclusion, the combination of the IFS survey and new radio facilities will greatly help to expand the scope and depth of the studies in this thesis.

²<http://www.aoc.nrao.edu/evla>

³<http://www.almaobservatory.org/>

Bibliography

- [1] Alatalo K. et al., 2013, MNRAS, 432, 1796
- [2] Allende Prieto C., Lambert D. L., & Asplund M., 2001, ApJ, 556, L63
- [3] Aniano G., Draine B. T., Gordon K. D., Sandstrom K., 2011, PASP, 123, 1218
- [4] Baldry I. K., Glazebrook K., Brinkmann J., IvezićŽ., Lupton R. H., Nichol R. C., Szalay A. S., 2004, ApJ, 600, 681
- [5] Baldry I. K. et al., 2006, MNRAS, 373, 469
- [6] Bell E. F., de Jong R. S., 2000, MNRAS, 312, 497
- [7] Bell E. F., Bower R. G., 2000, MNRAS, 319, 235
- [8] Bell E. F., 2003, ApJ, 586, 794
- [9] Bernardi M. et al., 2003, AJ, 125, 1866
- [10] Bertin E., Arnouts S., 1996, A&AS, 117, 393
- [11] Bigiel F., Leroy A. K., Walter F., Brinks E., De Blok W. J. G., Madore B., Thornley M. D., 2008, ApJ, 136, 2846
- [12] Bigiel F. et al., 2011, ApJL, 730, L13
- [13] Bolatto A. D., Wolfire M., Leroy A. K. 2013, ARA&A, 51, 207
- [14] Brown M. J. I., Dey A., Jannuzi B.T., Brand K., Benson A. J., Brodwin M., Croton D. J., Eisenhardt P. R., 2007, ApJ, 654, 858
- [15] Bruzual G., Charlot S., 1993, ApJ, 405, 538
- [16] Bruzual G., Charlot S., 2003, MNRAS, 539, 718

- [17] Buat V., Deharveng J. M., & Donas J. 1989, A&A, 223, 42
- [18] Calzetti D., 1997, AJ, 113, 162
- [19] Calzetti D. et al., 2007, ApJ, 666, 870
- [20] Calzetti D., 2013, Star Formation Rate Indicators. Cambridge Univ. Press, Cambridge, p. 419
- [21] Cappellari M. et al., 2011, MNRAS, 413, 813
- [22] Casoli M. et al., 1998, A&A, 331, 451
- [23] Catinella B. et al., 2010, MNRAS, 403, 683
- [24] Catinella B., et al., 2012, A&A, 544, A65
- [25] Chen Y. M. et al., 2012, MNRAS, 421, 314
- [26] Charlot S., Fall S. M., 2000, MNRAS, 539, 718
- [27] Combes F., Encrénaz P. J., Lucas R., Weliachew L., 1977, A&A, 55, 311
- [28] Conroy C., 2003, ARA&A, 51, 393
- [29] Daddi E. et al., 2010, ApJL, 714, 118
- [30] Davis T. A. et al., 2014, MNRAS, 444, 3427
- [31] Chary R., Elbaz D., 2001, ApJ, 556, 562
- [32] Dekel A., Birnboim Y., 2006, MNRAS, 368, 2
- [33] Dekel A., Sari R., Geverino D. 2009, ApJ, 703, 785
- [34] Draine B. T. & Li A. 2007, ApJ, 657, 810
- [35] Dressler A., Gunn J. E., 1983, ApJ, 270, 7
- [36] Eden D. J., Moore T. J. T., Morgan L. K., Thompson M. A., Urquhart J. S., 2013, MNRAS, 431, 1587
- [37] Elmegreen B. G., 1994, ApJ, 425, L73
- [38] Elmegreen B. G., 2011, preprint (arXiv:1101.3108)

- [39] Faber S. M., 2007, ApJ, 665, 265
- [40] Fang J. J., Faber S. M., Salim S., Graves G. J., Rich R. M., 2012, ApJ, 761, 23
- [41] Foyle K., Rix H.-W., Walter F., Leroy A. K., 2010, ApJ, 725, 534
- [42] Fukugita M., Hogan C. J., Peebles P. J. E., 1998, ApJ, 503, 518
- [43] Gadotti D. A. et al., 2009, MNRAS, 393, 1531
- [44] Gao Y. & Solomon P. M. 2004, ApJ, 606, 271
- [45] Garnett D. R., 1999, in IAU symp. 190, New Views of the Magellanic Clouds, ed. Y.-H. Chu, N. B. Suntzeff, J. E. Hesser, & D. A. Bohlender, 266
- [46] Garnett D. R., 2002, ApJ, 581, 1019
- [47] Genzel R. et al., 2010, MNRAS, 407, 2091
- [48] Genzel R. et al., 2015, ApJ, 800, 20
- [49] Glover S. C. O., Mac Low M.-M., 2011, MNRAS, 412, 337
- [50] Gil de Paz A., Boissier S., Madore B. F., Seibert M., Joe Y. H., 2007, ApJS, 173, 185
- [51] Gordon K. D., Clayton G. C., Witt A. N., Misselt K. A. ,2000, ApJ, 533, 236
- [52] Hao C.-N., Kenicutt R. C. Jr., Johnson B. D., Calzetti D., Dale D. A., Moustakas J. ,2011, ApJ, 741, 124
- [53] Hamajima K. & Tosa M. 1975, PASJ, 27, 561
- [54] Hartwick F. D. A., 1971, ApJ, 163, 431
- [55] Helfer T. T., Blitz L., 1993, ApJ, 419, 86
- [56] Helfer T. T., Blitz L., 1997, ApJ, 478, 162
- [57] Helfer T. T. et al., 2003, ApJS, 145, 259
- [58] Ilbert O. et al., 2010, ApJ, 709, 644
- [59] Jarrett T. H. et al., 2011, ApJ, 735, 112
- [60] Johnson B. D. et al., 2007, ApJS, 173, 377

- [61] Kauffmann G. et al., 2003a, MNRAS, 341, 33
- [62] Kauffmann G. et al., 2003b, MNRAS, 341, 54
- [63] Kauffmann G. et al., 2006, MNRAS, 367, 1394
- [64] Kauffmann G. et al., 2007, ApJS, 173, 357
- [65] Kennicutt R. C. Jr., 1989, ApJ, 344, 685
- [66] Kennicutt R. C. Jr., 1998, ARA&A, 36, 189
- [67] Kennicutt R. C. Jr. et al., 2003, PASP, 115, 928
- [68] Kennicutt R. C. Jr. & Evans N. J., 2012, ARA&A, 50, 531
- [69] Kereš D., Katz N., Weinberg D. H., Davié R., 2005, MNRAS, 363, 2
- [70] Knapen J. H., Beckman J. E., Cepa J., Nakai N., 1996, A&A, 308, 27
- [71] Kewley L. J. & Dopita M. A., 2002, ApJS, 142, 25
- [72] Kong X., Charlot S., Brinchmann J., Fall S. M., 2004, MNRAS, 349, 769
- [73] Launhardt R., Zylka R., Mezger P. G., 2002, A&A, 384, 112
- [74] Leroy A. K. et al., 2008, AJ, 136, 2782
- [75] Leroy A. K. et al., 2011, ApJ, 737,12
- [76] Leroy A. K. et al., 2012, AJ, 144,3
- [77] Leroy A. K. et al., 2013, AJ, 146,19
- [78] Lord S. D., Young J. S., 1990, ApJ, 356, 135
- [79] Madore B. F., 1977, MNRAS, 178,1
- [80] Madore B. F., van den Bergh S., Rogstad D. H. 1974, ApJ, 191, 317
- [81] Martig M., Bournaud F., Teyssier R., Dekel A., 2009, ApJ, 707, 250
- [82] Maraston C., 1998, MNRAS, 300, 872
- [83] Martin D. C., 2005, ApJ, 619, L1

- [84] McGaugh S. S., 1991, ApJ, 380, 140
- [85] Meier D. S. & Turner J. L., 2005, ApJ, 618, 259
- [86] Momose R. et al., 2013, ApJL, 772, L13
- [87] Moran S. M. et al., 2010, ApJ, 720, 1126
- [88] Moran S. M. et al., 2012, ApJ, 745, 66
- [89] Muñoz-Mateos J. C., Gil de Paz A., Boissier S., Zamorano J., Jarrett T., Gallego J., Madore B. F., 2007, ApJ, 658, 1006
- [90] Pagel B. E. J., Edmunds M. G., Blackwell D. E., Chun M. S., Smith G., 1979, MNRAS, 189, 95
- [91] Pan H.-A., Kuno N., Hirota A., 2014, PASJ, 66, 27
- [92] Peng C. Y., Ho L. C., Impey C. D., Rix H.-W. et al., 2002, AJ, 124, 266
- [93] Peng C. Y., Ho L. C., Impey C. D., Rix H.-W. et al., 2010, MNRAS, AJ, 139, 2097
- [94] Pettini M., Pagel B. E. J., 2004, MNRAS, 348, L59
- [95] Pérez E. et al., 2013, ApJ, 764, L1
- [96] Poggianti B. M., Smail I., Dressler A., Couch W. J., Barger A. J., Butcher H., Ellis R. S., Oemler A., Jr., 1999, ApJ, 518, 576
- [97] Rebolledo D., Wong T., Leroy A., Koda J., Meyer D. J., 2012, ApJ, 757, 155
- [98] Rees M. J. & Ostriker J. P., 1977, MNRAS, 179, 541
- [99] Rickard L. J., Palmer P., Morris M., Zuckerman B., Turner B. E., 1975, ApJ, 199, L75
- [100] Rieke G. H. et al., 2009, ApJ, 692, 556
- [101] Sage L. J., 1993, A&A, 272, 123
- [102] Saintonge A. et al., 2011a, MNRAS, 415, 32
- [103] Saintonge A. et al., 2011b, MNRAS, 415, 61
- [104] Saintonge A. et al., 2012, ApJ, 758, 73

- [105] Salim S. et al., 2012, ApJ, 755, 105
- [106] Sandstrom K. M. et al., 2013, ApJ, 777, 5
- [107] Sanduleak N., 1969, AJ, 74, 47
- [108] Sánchez S. F., et al., 2012, A & A, 538, A8
- [109] Schlegel D. J., Finkbeiner D. P., Davis M., 1998, ApJ, 500, 525
- [110] Schmidt M., 1959, ApJ, 129, 243
- [111] Scoville N. Z., Yun M. S. Sanders D. B., Clemens D. P., Waller W. H., 1987, ApJS, 63, 821
- [112] Shetty R., Kelly B. C., Bigiel F., 2013, MNRAS, 430, 288
- [113] Silk J. et al., 1977, ApJ, 211, 638
- [114] Skrutskie M. F. et al., 2006, AJ, 131, 1163
- [115] Solomon P. M., de Zafra R., 1975, ApJ, 199, L79
- [116] Solomon P. M., Rivolo A. R., Barrett J., Yahil A. et al., 1987, ApJ, 319, 730
- [117] Strateva I., et al., 2001, AJ, 122, 1861
- [118] Strong A. W. & Mattox J. R., 1996, A&A, 308, L21
- [119] Tacconi L. J. et al., 2010, Nature, 463, 781
- [120] Tinsley B. M. & Gunn J. E., 1976, ApJ, 203, 52
- [121] Tosa M. & Hamajima K., 1975, PASJ, 27, 501
- [122] Tremonti C. A. et al., 2004, ApJ, 613, 898
- [123] Vazdekis A., 1999, ApJ, 513, 108
- [124] Verheijen M., van Gorkom J. H., Szomoru A. et al., 2007, ApJ, 668, L9
- [125] Walter F., Brinks E., de Blok W. J. G., Bigiel F., Kennicutt R. C. Jr., Thornley M. D., Leroy A. K., 2008, AJ, 136, 2563
- [126] Wang J. et al., 2011, MNRAS, 412, 1081

- [127] Weinmann S. M., Kauffmann G., van den Bosch F. C., Pasquali A., McIntosh D. H., Mo H., Yang X., Guo Y., 2009, MNRAS, 394, 1213
- [128] White S. D., Frenk C. S., 1991, ApJ, 379, 52
- [129] Wild V., Kauffmann G., Heckman T., Charlot S., Lemson G., Brinchmann J., Reichard T., Pasquali A., 2007, MNRAS, 381, 543
- [130] Williams R. J., Quadri R. F., Franx M., van Dokkum P., Toft S. Kriek M. Labbe I., 2010, ApJ, 713, 738
- [131] Wong T., Blitz L., 2002, ApJ, 569, 157
- [132] Wright E. L. et al., 2010, AJ, 140, 1868
- [133] Wu J. et al., 2005, ApJ, 635L, 173
- [134] Wuyts S. et al., 2011, ApJ, 742, 96
- [135] Wyder T. K. et al., 2007, ApJS, 173, 293
- [136] Yi S. K., et al., 2005, ApJ, 619, L111
- [137] York D. G. et al., 2000, AJ, 120, 1579
- [138] Young L. M. et al., 2011, MNRAS, 414, 910
- [139] Young J. S. & Knezeck P. M., 1989, ApJ, 347, L55
- [140] Young J. S. & Scoville N. Z., 1991, ARA&A, 29, 581
- [141] Young J. S. et al., 1995, ApJS, 98, 219

Acknowledgements

My deepest gratitude is to my supervisor, Guinevere Kauffmann. This thesis would never have been possible without her. She constantly inspires me, motivates me, and supports me. When I have doubts or encounter obstacles, she is always there with me, and leads me out of troubles and towards the right path. Her knowledge, advice and insight are inexhaustible source for my scientific development. I deeply appreciate her invaluable guidance and enormous patience to me.

I am indebted to my co-workers, Richard D'Souza, Jonas Johansson, Sean Moran, Yan-Mei Chen, and Jing Wang for kindly helping me and answering my all sorts of questions. It has been very pleasant to discuss and interact with them. Their constructive inputs and useful advice have largely improved my work. I am also grateful to Simon White, Linda Tacconi, Stephane Charlot for their insights into my work. The discussions with them are very helpful and inspiring.

I owe special thanks to Else, Nitya, and Wenting. I am privileged to ever meet them and have them as lifelong friends. They always encourage me, support me and comfort me when I am weak, upset, and depressed. They keep me positive throughout the difficult time. I deeply value the friendship they have given me without any reservation.

I would like to thank MPA and IMPRS for providing such a wonderful environment to conduct research. I also want to acknowledge helpful conversations and discussions with many colleagues from MPA and IMPRS. Besides, I wish to express my gratitude to the secretaries in MPA, Cornelia, Gabi, Maria and Sonja for providing me prompt helps with warm smiles all the time. They have made my stay in MPA and Germany much more easy and smooth.

Finally I dedicate this dissertation to my family in Taiwan.

List of Publications

- [1] **M.-L. Huang** & G. Kauffmann *The variation in molecular gas depletion time among nearby galaxies: II the impact of galaxy internal structures*, MNRAS, 450, 1375 (2015)
- [2] S. Roychowdhury, **M.-L. Huang**, G. Kauffmann, J. Wang, J. N. Chengalur *The spatially resolved Kennicutt-Schmidt relation in HI dominated regions of spiral and dwarf irregular galaxies*, MNRAS, 449, 3700 (2015)
- [3] **M.-L. Huang** & G. Kauffmann *The variation in molecular gas depletion time among nearby galaxies: what are the main parameter dependences?*, MNRAS, 443, 1329 (2014)
- [4] J. Wang, F. Jian, A. Michael, G. Kauffmann, G. Jozsa, P. Serra, **M.-L. Huang**, J. Brinchmann, T. van der Hulst, F. Bigiel *An observational and theoretical view of the radial distribution of HI gas in galaxies*, MNRAS, 441, 2159 (2014)
- [5] F. Jian, G. Kauffmann, **M.-L. Huang**, R. M. Yates, S. Moran, T. M. Heckman, R. Davé, Q. Guo, B. M. B. Henriques *Star Formation and metallicity gradients in semi-analytic models of disc galaxy formation*, MNRAS, 434, 1531 (2013)
- [6] **M.-L. Huang**, G. Kauffmann, Y. Chen, S. M. Moran, T. M. Heckman, R. Davé, J. Johansson *Spatially-resolved star formation histories of nearby galaxies: evidence for episodic star formation in disks*, MNRAS, 43, 2622 (2013)
- [7] **M.-L. Huang** & C.-Y. Hwang *Morphologically-Identified Merging Galaxies in the SWIRE Fields*, ApJ, 734, 11 (2011)